L-Università ta' Malta

A novel approach to groundwater monitoring in the Maltese Islands: Analysis of auto- and cross-correlation functions of ambient seismic noise

Luca Laudi

Supervisor: Prof. Pauline Galea
Co-supervisors: Prof. Sebastiano D'Amico
Dr Matthew R. Agius

Department of Geosciences
Faculty of Science
University of Malta

February 5, 2023

A dissertation submitted in partial fulfilment of the requirements for the degree of M.Sc. in Geosciences (by Research)

Water is the driving force of all nature

Leonardo da Vinci

Dedication

I would like to dedicate this dissertation to my late grandfather Giovanni. You have always instilled inspiration in me to be strong-willed and face challenges with a smile and infinite courage.

Acknowledgement

My deepest gratitude goes to my supervisors Prof. Pauline Galea, Prof. Sebastiano D'Amico, and Dr Matthew R. Agius. Despite their professional and personal commitments, they always made it a priority to guide and support me throughout the course of this study. I would also like to thank them for the academic and life lessons that they taught me, and for giving me opportunities to present my study at conferences abroad. Special thanks to Dr Thomas Lecocq from the Royal Observatory of Belgium and Dr Martin Schimmel from Geosciences Barcelona, for their constant and helpful advice on the software and techniques that were used.

I would like to thank the Energy and Water Agency for awarding the SIGMA project all the necessary funds for me to conduct my research throughout the past year and a half. Special thanks go to Mr. Manuel Sapiano, Dr Michael Schembri, Dr Julian Mamo, and Ms. Christa Pisani - all were very helpful in providing me with the necessary hydrological data to complete this study. I would also like to thank my friend Rami Kalfouni, for always being a helping hand in the writing of this thesis.

I cannot fail to mention my close friends, who have always understood and supported me in my goals. Finally, the people I want to thank the most of all are my parents, Horace and Esther, my sister Lara, and the rest of my family. The patience you have had with me, but also the never-ending belief that I would succeed have always pushed me to work hard and to believe in myself.

Abstract

The Maltese islands, approximately 315 km^2 in area with a high population density, face high levels of water stress due to low amounts of rainfall and a dependence on groundwater abstraction. Up till now, *in-situ* borehole readings are the only utilised method to monitor the quantitative status of groundwater in Malta. This study investigates an innovative, cost-effective approach to groundwater monitoring in an island environment; by computing cross-correlations and autocorrelations of ambient seismic noise recorded by two types of seismic stations in the Maltese islands: six broadband from the Malta Seismic Network (MSN) and six short-period from the FASTMIT network. Six years of seismic noise data was utilised from the broadband stations, and a year-long dataset was available from the short-period stations. Interstation distances in this study ranged from 3-35 km. The MSNoise program was used for the data management and processing. Seismic velocity changes ($\delta v/v$), which are possibly induced by changes in groundwater level, were detected using the Moving-Window Cross-Spectral (MWCS) technique. Both types of stations can provide similar sensitivity to the $\delta v/v$ when taking into consideration appropriate filters (0.1-1 Hz and 0.3-3 Hz for the broadband and short-period stations respectively).

The results demonstrate that seasonal and annual changes in the groundwater levels can be detected by changes in seismic velocity. The method works for both cross-correlation (maximum $\delta v/v$ variation of $\sim$0.3%) and autocorrelation functions (maximum $\delta v/v$ variation of $\sim$2%) of ambient seismic noise, the latter being an order of magnitude more sensitive. Seasonal and annual variations of the $\delta v/v$ from autocorrelations of some stations were found to be more pronounced than from cross-correlations. Clear seasonal variations in $\delta v/v$ were observed as a result of cross-correlations between short-period stations as well as short-period and broadband stations. The quality of the $\delta v/v$ deteriorates at longer interstation distances when seasonal variations in the $\delta v/v$ are less obvious. Presumably, this is because longer interstation paths tend to traverse more complex geology, different types of aquifers, or even the sea.

Generally, the comparison of the $\delta v/v$ with groundwater level readings from nearby boreholes show highly encouraging similarities in the seasonal variations, indicating that $\delta v/v$ may be used as a proxy for monitoring groundwater levels in the Maltese islands in regions where borehole measurements are sparse.

Contents

List of Figures

List of Tables

List of Abbreviations

BC	Blue Clay
CCF	cross-correlation function
$cmH2O$	centimetres of water column
EWA	Energy and Water Agency
FAO	Food and Agricultural Organisation
FASTMIT	FAglie Sismogeniche e Tsunamigeniche nei Mari ITaliani
GL	Globigerina Limestone
GPS	Global Positioning System
GRACE	Gravity Recovery and Climate Experiment
GUI	graphical user interface
GWD	Groundwater Directive
HNM	high noise-model
InSAR	Interferometric Synthetic-Aperture Radar
LCL	Lower Coralline Limestone
LNM	low noise-model
MAR	Managed Aquifer Recharge
MSEED	miniSEED
MSL	mean sea-level
MSLA	mean sea-level aquifer
MSN	Malta Seismic Network
MWCS	moving-window cross-spectral technique
NSO	National Statistics Office
ObsPY	Python toolbox for seismologists, seismological observatories, and data centres
PSD	power spectral density
PWS	phase-weighted stack
QC	Quality Control
RMS	root-mean-square
SAC	Seismic Analysis Code
SEED	Standard for the Exchange of Earthquake Data
SEWCU	Sustainable Energy and Water Conservation Unit
SMRG	Seismic Monitoring and Research Group
SQL	Structured Query Language
UCL	Upper Coralline Limestone
WCMP	Water Catchment Management Plan

WFD	Water Framework Directive
WLS	weighted linear regression
WSC	Water Services Corporation
UN	United Nations
Z	vertical component
$\delta v/v$	change in seismic velocity

1. Introduction

1.1. The global groundwater crisis

Groundwater accounts for 97% of global liquid freshwater, making it the largest non-frozen freshwater resource in the world (Elshall et al., 2022). Subsurface water is classified as groundwater when it fully saturates the pores, cracks and fissures of underground rocks found below the water table (Giordano et al., 2009). Under ordinary hydraulic gradients, these permeable and saturated geological formations, or aquifers, can transmit significant quantities of water vertically downwards, and horizontally (Freeze and Cherry, 1979). Groundwater is a crucial natural resource that approximately half of the global population depends on for drinking water (Velis et al., 2017). However, studies have documented an unsustainable decrease in groundwater resources on the regional scale, such as in the Euro-Mediterranean region (Xanke and Liesch, 2022), as well as on the global scale (Famiglietti, 2014; Konikow, 2011; Wada et al., 2010).

The ongoing global population increases and climate change impacts on the hydrological cycle have led to groundwater depletion to become a more significant global issue (Gude and Maganti, 2021). Furthermore, global water demand is set for a 20-30% increase by 2050 (Boretti and Rosa, 2019). This increase in water demand has led to land subsidence and reduced groundwater storage in aquifers globally (e.g., Galloway and Burbey, 2011). Figure 1.1 shows the extent of the groundwater table decline in centimetres/year according to a study conducted from 1990–2014 (United Nations (UN), 2021). The most significant decline has occurred in arid regions such as in Mexico, parts of USA, North Africa, Saudi Arabia, India, China, and Australia. This corresponds with the sudden intensification of groundwater abstraction in arid and semi-arid regions during the 20th century (Margat and Van der Gun, 2013). Unsustainable groundwater abstraction for irrigation purposes accounts for approximately 70% of the total global freshwater withdrawal (Food and Agricultural Organisation (FAO), 2020), which makes it a major player in global groundwater table decline.

1.2. Groundwater monitoring

One of the main goals of sustainable groundwater resource management is to locate and access groundwater while ensuring permanent availability of groundwater resources for

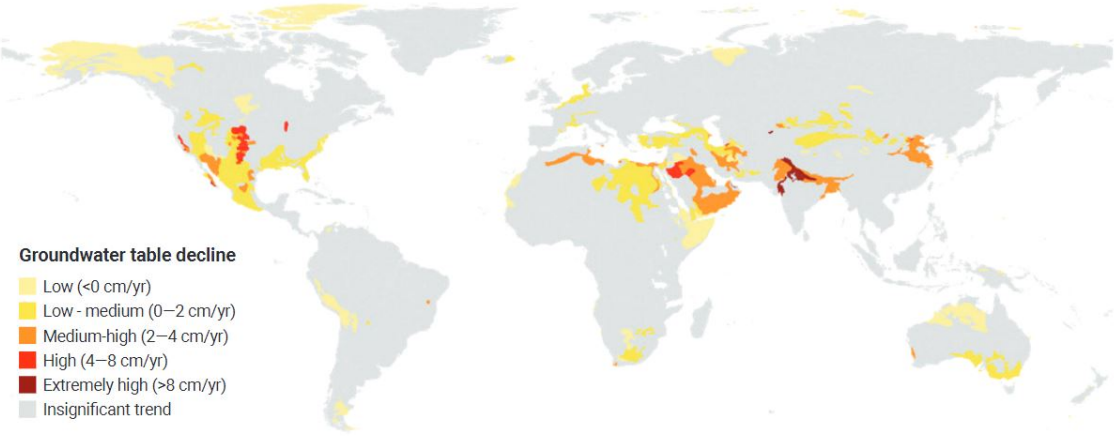

Figure 1.1.: Global groundwater table decline. The map shows the average from 1990-2014 in cm/yr (UN, 2021). The highest groundwater table decline, in brown and red, is mainly indicative of unsustainable groundwater abstraction in the said regions.

an indefinite period (Margat and Van der Gun, 2013; van der Gun, 2021). Therefore, this relates to the day-to-day operations that aim at locating, quantifying, and controlling groundwater abstraction (UN, 2022). To do so, groundwater must be monitored for variations in its hydrogeological characteristics, such as changes in groundwater level at a detailed spatial and temporal resolution (Asefa et al., 2004).

Groundwater is typically monitored using a piezometer, which is a device that can measure groundwater level as a function of varying water pressure in underground rock pores. Piezometric networks, which consist of a number of wells tapping into a groundwater body, act as essential tools to the monitoring of both the quantitative and qualitative status of groundwater (Kavusi et al., 2020). Measuring the variations in groundwater level from wells provides the most direct and accurate measurement of the quantitative status of the groundwater body (Zhou et al., 2013). These groundwater level variations are specific to the location of the piezometric wells in the network (Healy and Cook, 2002). However, a large number of sampling points (piezometric wells) would be required to adequately monitor the water level changes of a groundwater body (Zhou et al., 2013). This could incur significant costs to set up and maintain, and require extensive planning to design the optimal monitoring network (Gemitzi and Lakshmi, 2018; Kavusi et al., 2020).

To conduct effective groundwater monitoring, making use of more than one groundwater data in tandem can be beneficial. Alternative groundwater monitoring techniques use the Global Positioning System (GPS, e.g., Bawden et al., 2001; Ji and Herring, 2012; King et al., 2007), Interferometric Synthetic-Aperture Radar (InSAR, e.g., Chaussard et al., 2017; Galloway and Hoffmann, 2007; King et al., 2007), and gravity measurements from satellites such as the Gravity Recovery and Climate Experiment satellite (GRACE, e.g., Ramillien et al., 2008; Rodell et al., 2009; Xanke and Liesch, 2022; Xiao et al., 2017). Using GPS for monitoring surface displacements can measure groundwater changes at

good temporal resolution, but at a limited spatial resolution (Bawden et al., 2001; Ji and Herring, 2012; King et al., 2007). On the other hand, surface displacements measured by InSAR indicate groundwater changes at a high spatial resolution, but weak temporal resolution (Chaussard et al., 2017; Galloway and Hoffmann, 2007; King et al., 2007). Utilising the GRACE satellite for obtaining gravity measurements has proven its sensitivity to changes in water masses at large wavelengths only, but not at the more important shorter wavelengths that are related to local changes (e.g., Rodell et al., 2009; Xiao et al., 2017). Another disadvantage of this technique is that the gravity measurements suffer non-uniqueness between aquifer depths and water mass (e.g., Rodell et al., 2009; Xiao et al., 2017).

Despite the significant costs involved, groundwater monitoring is important because it allows for early identification of negative trends, and the introduction of remediation strategies before the state of the groundwater body deteriorates any further (United Nations, 2022). The use of on-the-ground geophysical techniques to obtain spatio-temporal groundwater data can be a complementary option to monitoring groundwater via borehole readings, if the latter are absent in the region in question (Kirsch, 2006).

1.2.1. Quantitative groundwater monitoring in the Maltese islands

Figure 1.2.: A map of the Mediterranean region. The red box indicates the location of the Maltese islands.

As a result of more frequent drought periods and higher temperatures due to the changing climate, southern European islands such as Rhodes and Crete are projected to face more pronounced water supply issues (Sauter et al., 2013). The Maltese islands, an island nation in the centre of the Mediterranean (Figure 1.2), is deemed as the European country facing

the highest stress on its water resources (Hallett et al., 2017). Malta has a semi-arid climate with ≈550 mm of annual rainfall (Hartfiel et al., 2020). The Maltese islands consist of three main islands; Malta, Gozo, and Comino (see Figure 2.5), and cover a total area of ≈315 km^2. In 2018, Malta had a very high population density of 1867 persons/km^2 (National Statistics Office (NSO), 2019a). In the same year, a record 2.6 million tourists visited the islands before the COVID-19 outbreak (NSO, 2019b). The main population, industrial and tourism activity take place in Malta. These reasons have led to Malta's strong dependence on groundwater abstraction and desalinisation plants (Sapiano, 2020). In 2021, 59% of the public water supply was produced by desalinisation (WSC, 2021). Moreover, 80% of the water used in the Maltese agricultural sector is directly abstracted from groundwater resources (Fenech et al., 2019), via boreholes or underground galleries (Hallett et al., 2017). The re-use of treated greywater for irrigation purposes has been recently introduced to alleviate pressures on the groundwater resources (Sapiano, 2022; Sustainable Energy and Water Conservation Unit (SEWCU), 2015). Sapiano (2020) provides an overview of the integrated water management approach employed up till now in the Maltese islands to safeguard water resources in a sustainable manner.

The groundwater monitoring network of the Maltese islands is managed by the Water Services Corporation (WSC) and the Energy and Water Agency (EWA). The latter records the groundwater levels from a network of boreholes according to the obligations of the Water Framework Directive (WFD) and the Groundwater Directive (GWD). These directives identify this parameter as the primary metric of quantitative groundwater status (SEWCU, 2015). The first Water Catchment Management Plan (WCMP) (SEWCU, 2011) in Malta utilised a monitoring network of gauging boreholes and their respective groundwater level measurements to assess the quantitative status of the mean sea-level aquifer (MSLA) system (see Section 2.3.2). Manual readings of water level were conducted in some of these stations since the 1940's, using dip tape measurements. Since the late 1990s, water level data was collected every 30 minutes utilising water level shaft encoders fitted with data loggers (Thalimedes, OTT (2011)), which serve as automated water level monitoring equipment (SEWCU, 2011). The recorded data was downloaded regularly to eventually produce water level plots in the temporal scale (SEWCU, 2015). In 2021, the EWA employed pressure transducers called divers, that can monitor the groundwater's real-time quantitative status. These divers measure water level, depth, temperature and electrical conductivity (vanEssen, 2022). The divers measure total water depth by calculating the hydrostatic pressure of the water above a pressure sensor diaphragm (vanEssen, 2022). These instruments can store a maximum of 144000 readings with backup (vanEssen, 2022). Once these divers are retrieved, data is downloaded and converted from centimetres of water column ($cmH2O$) to metres using appropriate equations.

1.2.2. Motivation for the study

In recent years, EWA started to look for innovative, cost-effective ideas to enhance its groundwater monitoring and management. One approach derives from the cross-correlation of ambient seismic noise (Campillo, 2006; Shapiro and Campillo, 2004). Such alternative methods can assess the groundwater over a greater extent and may provide a broader picture of the subsurface groundwater level and dynamics. This technique detects changes in the seismic wave speeds that may vary through seasonal water content in rocks. Water-saturated rocks experience an increase in pore pressure, which in turn leads to the opening of cracks in the rock (Christensen and Wang, 1985). The cracks reduce the contact area between different grains of rock leading to a decrease in seismic velocity (Christensen and Wang, 1985). Thus, variations in the seismic wave speeds reflect changes in the medium through which the waves are passing such as from changes in groundwater content (e.g., Meier et al., 2010; Sens-Schönfelder and Wegler, 2006).

This phenomenon has been observed at different locations such as in the mountain region of the Himalayas (Illien et al., 2021), San Gabriel Valley Basin, California (Clements and Denolle, 2018), and the Reykjanes geothermal reservoir in Iceland (Sánchez-Pastor et al., 2019). Further studies which have been conducted in other regions will be discussed in the following sections. Malta is different from these locations because it is a small island with no lakes, rivers, mountain regions, geothermal reservoirs, or watersheds. Moreover, rainfall is relatively low, and the islands are surrounded by saline water, which to a certain extent, interacts with the groundwater. Studies are yet to determine whether variations in groundwater on small islands, particularly in the Mediterranean region, can be detected through seismic data.

In this study, ambient seismic noise data recorded by the seismic networks on the Maltese Islands are analysed to determine temporal changes in seismic velocity. These changes were compared to time series of groundwater level measurements from nearby boreholes to investigate the correlation between them. Effectively, this would mean that the signal processing technique used in this study can be utilised in groundwater management together with conventional borehole readings. While the *in-situ* borehole readings provide accurate site-specific data on water levels, the proposed technique would provide a more regional approach to quantitative groundwater monitoring. Finally, this study may help the relevant authorities to monitor illegal abstraction of groundwater in the Maltese islands, since sudden groundwater level changes may be detected in a specific location over a particular time.

This dissertation is structured in the following manner; a literature review highlighting similar studies that have been conducted, a description of the data, methodology, and the different tests that have been carried out, and the analysis of the results followed by a discussion about the main outcomes of the study.

2. Literature review

In this chapter, the different types of seismic waves and ambient seismic noise, the cross- and autocorrelation techniques and how such methods relate to changes in groundwater levels will be discussed. Additionally, Malta's geology and hydrogeology will be described.

2.1. Seismic waves

Seismic waves are vibrations that propagate through the ground. These waves typically originate from earthquakes, volcanic eruptions, or man-made explosions that release elastic energy throughout the Earth. Earthquake seismology has been one of the most effective tools in mapping out the Earth's internal structure and understanding plate tectonics (Fowler, 2005). Earthquake distribution dictates where the most seismic energy is observed in the Earth (Khilyuk et al., 2000), whilst seismic wave paths provide an understanding of the Earth's interior (Fowler, 2005). Seismic waves travel at different speeds, depending on the elastic moduli and the density of the rocks through which the elastic waves are passing. (Fowler, 2005; Stein and Wysession, 2003). The two types of elastic waves are body waves, which travel through the Earth, and surface waves, which contain the remaining seismic energy that travels through the surface layers (e.g., Fowler, 2005).

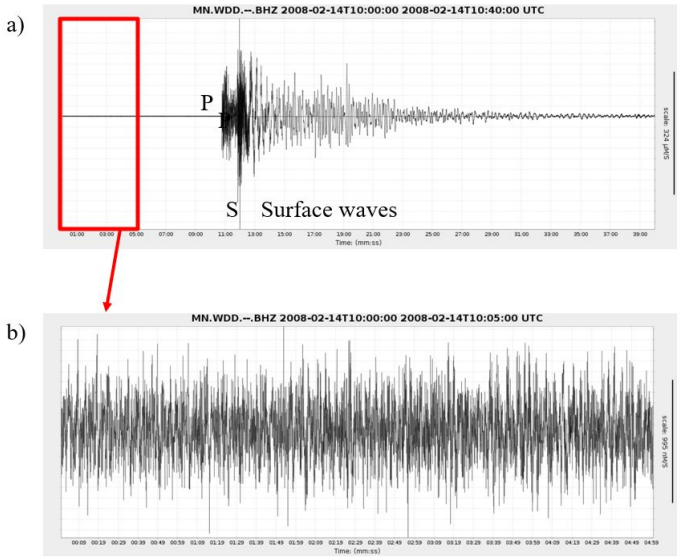

Figure 2.1.: The seismogram of an earthquake that was recorded on one of the seismic stations of the Maltese islands. (a) The seismogram of a M 6.9 earthquake that occurred 35 km south of Methóni, Greece. The arrivals of the body waves (*P*- and *S*-waves) and the surface waves are labelled. (b) A zoom-in on the ambient seismic noise recorded by the station before the earthquake, highlighted by the red box in (a).

The two types of body waves are primary waves (*P*-waves) and secondary waves (*S*-waves) (e.g., Shearer, 2009). *P*-waves are longitudinal waves, where the particles propagating along the ray path vibrate in parallel to the direction that the wave is travelling (Lowrie, 2007; Milsom and Eriksen, 2011). This translates to the compression and rarefaction of the medium through which the wave is passing (Fowler, 2005; Shearer, 2009). Contrastingly, *S*-waves are transverse waves, where the particle motion is perpendicular to the direction of propagation (Fowler, 2005). This leads to the shearing or rotation of the medium through which the wave is passing, but not a change in volume of the medium (Fowler, 2005). *P*-waves are the fastest seismic waves, and the first to be recorded by a seismometer when an earthquake occurs. *S*-waves travel slower than *P*-waves, and hence are picked up by a seismometer at a later arrival time (Lowrie, 2007), as shown in Figure 2.1a.

Surface waves are also split into two types, called Rayleigh waves and Love waves depending on the particle motion in the wavefront (e.g., Lowrie, 2007). The main difference between these surface waves is that for laterally homogenous media Rayleigh waves are radially (vertically) polarised, while Love waves are transversely (horizontally) polarised (e.g., Shearer, 2009). Due to their polarization, Rayleigh and Love waves are recorded on the vertical and horizontal components of a seismograph, respectively (Fowler, 2005). Rayleigh waves can occur at any free surface while Love waves are guided by a low seismic velocity layer overlying a high-velocity medium (e.g., Shearer, 2009). Figure 2.2 shows how Rayleigh waves propagate as a retrograde ellipse in the vertical plane, meaning that the elliptical motion of the particle is opposite to the direction of propagation (Fowler, 2005; Telford et al., 1990). Love wave motion is transverse to the propagation.

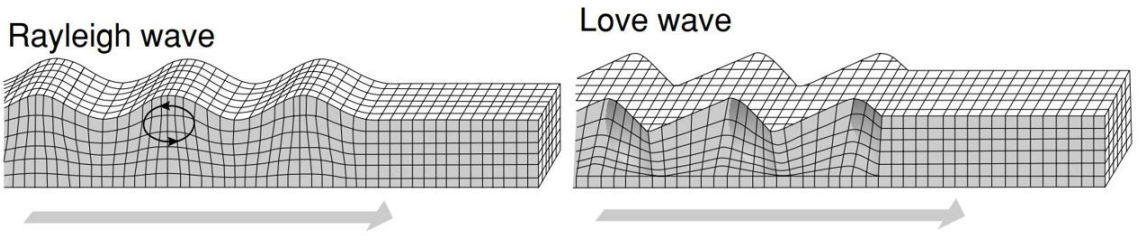

Figure 2.2.: Seismic surface waves propagation. Rayleigh and Love waves and their respective particle motions during their propagation (Fowler, 2005).

When compared to body waves, surface waves exhibit larger amplitudes and longer durations (Fowler, 2005; Shearer, 2009). Surface waves travel at lower velocities, and so they arrive after *P*- and *S*-waves on the seismograph (Fowler, 2005; Shearer, 2009), as shown in Figure 2.1a.

2.1.1. Ambient seismic noise

Ambient seismic noise is constituted by a series of random, continuous signals (e.g., Bonnefoy-Claudet et al., 2006; Groos, 2010; Yang and Ritzwoller, 2008) in the Earth's surface and shallow rock layers. These waves could be caused by both natural and anthropogenic sources (Asten, 1978; Asten and Henstridge, 1984; Bonnefoy-Claudet et al., 2006; Groos, 2010; Gutenberg, 1958). Ambient noise is ever-present and independent of earthquake sources (Yang and Ritzwoller, 2008). Figure 2.1b shows an example of ambient seismic noise recorded on the seismometer before an earthquake occurred. Natural sources of ambient seismic noise are ocean wave action striking the coast, tides, local and large-scale meteorological conditions (e.g., cyclones over the oceans), air pressure changes, and turbulent winds that may cause the vibrations of trees and buildings. Anthropogenic sources include road traffic, industrial machinery, explosions, and underground reservoir exploitation (Asten, 1978; Asten and Henstridge, 1984; Bonnefoy-Claudet et al., 2006; Groos, 2010; Gutenberg, 1958).

Urban seismic noise, which varies in the spatial and temporal domain, consists of anthropogenic time-dependent signals being superimposed with naturally sourced signals (Groos and Ritter, 2009). Naturally sourced noise (microseisms) exhibits variations depending on natural phenomena, while anthropogenic or cultural noise (microtremors) varies according to the hourly, daily, and weekly variations in human activity (Bonnefoy-Claudet et al., 2006). Seismic stations on islands tend to record significant levels of ambient seismic noise, particularly noise of marine origin (Hedlin and Orcutt, 1989), such as in case of the Maltese islands (e.g., Bozionelos et al., 2019; Galea et al., 2021).

Natural sources of ambient noise generally contain seismic waves with a frequency of less than 1 Hz (Asten, 1978; Gutenberg, 1958). Microseismic noise from ocean gravity waves (Hasselmann, 1963; Longuet-Higgins, 1950), have been recorded on broadband stations worldwide in the frequency band of 0.05-0.3 Hz (Davy et al., 2015). Ocean microseisms are observed at 0.5-1.2 Hz (Asten, 1978; Asten and Henstridge, 1984) and are split into primary and secondary microseisms. Primary microseisms are represented by a smaller amplitude hump in the spectrum at 10-20 s period, which peak at around 14 s and have the same period as ocean swells (Davy et al., 2015; Gualtieri et al., 2013). Primary microseisms are generated by the interaction of swell waves with the sloping seafloor along the coast (Davy et al., 2015; Hasselmann, 1963). On the other hand, secondary microseisms exhibit approximately half the period of ocean waves at around 3-10 s (Davy et al., 2015; Gerstoft and Tanimoto, 2007). At 7 s, secondary microseisms have the strongest noise peak when compared to primary microseisms (Gualtieri et al., 2013). Swell waves of similar periods that are travelling in directions opposite to each other may interfere and cause second-order pressure fluctuations which induce secondary microseisms (Longuet-Higgins, 1950). At frequencies between 1 – 5 Hz, noise can be both natural and cultural,

while at frequencies higher than 5 Hz, noise is of cultural origin (Asten, 1978; Gutenberg, 1958). Generally, 1 Hz is considered as the spectral boundary between natural and cultural noise (Bonnefoy-Claudet et al., 2006). An exact border frequency that separates the noise wave field is not possible because this is site specific, depending on the local geological conditions and the predominant noise sources (Groos, 2010). For example, the ambient noise field can be dominated by cultural sources at 0.5-1 Hz in a soft subsoil setting (e.g., Groos and Ritter, 2009). However, on hard rock settings, anthropogenic signals can only be observed at frequencies of around 1 Hz or higher (Bonnefoy-Claudet et al., 2006).

2.1.2. Correlation of ambient seismic noise

It has been shown that the cross-correlation function (CCF) between two time series of random ambient noise recorded from two seismic stations at the same time corresponds to the Green's function of the medium between the sensors (Campillo and Paul, 2003; Clarke et al., 2011; Lobkis and Weaver, 2001; Sabra et al., 2005a; Shapiro et al., 2005; Wapenaar and Fokkema, 2006; Weaver and Lobkis, 2004). If one of the sensors is considered to be an impulsive source, the retrieval of the Green's function between two sensors yields the impulse response of the Earth recorded at the other sensor (Grobbe et al., 2021). Cross-correlation of ambient seismic noise is a powerful tool for imaging the Earth's interior on a local, regional or global scale (e.g., Agius et al., 2022; Bensen et al., 2007; Lin et al., 2007, 2008; Moschetti et al., 2007; Sabra et al., 2005b; Shapiro et al., 2005; Yang and Ritzwoller, 2008; Yang et al., 2007; Yao et al., 2006). The delay times of the Green's function may vary because of either a sudden change in the position of the noise source or scatterers, or changes in the medium velocity (Lecocq et al., 2014). With this method, real-time data from seismic stations can be utilised for the continuous monitoring and investigation of the medium between the sensors (Lecocq et al., 2014). As an example, the noise recorded by two stations in Gozo, XLND and FM04 (Figure 2.3a), is represented by the 30-minute time segments shown in blue and red in Figure 2.3b. Performing cross-correlation of these time series yields the Green's function or the impulse response. This is represented by the zoomed CCF in Figure 2.3c. The noise travelling from stations FM04 to XLND produces a negative time lag, or arrival time, while noise travelling from stations XLND to FM04 produces a positive time lag. Figure 2.3d shows the CCF processing for a whole day. The grey shading consists of 96 individual grey lines or CCFs on top of eachother. This is because the daily CCF stack consists of 96 CCFs from 30-minute time windows at a time step of 15 minutes (see Section 4.6). The black line in Figure 2.3d is the 1-day stack of all the grey lines.

Another approach is autocorrelation, which is the same as cross-correlation, but the noise recorded by a single station is correlated with itself (Gubbins, 2004). Thus, the CCF from an autocorrelation represents the ground below the station.

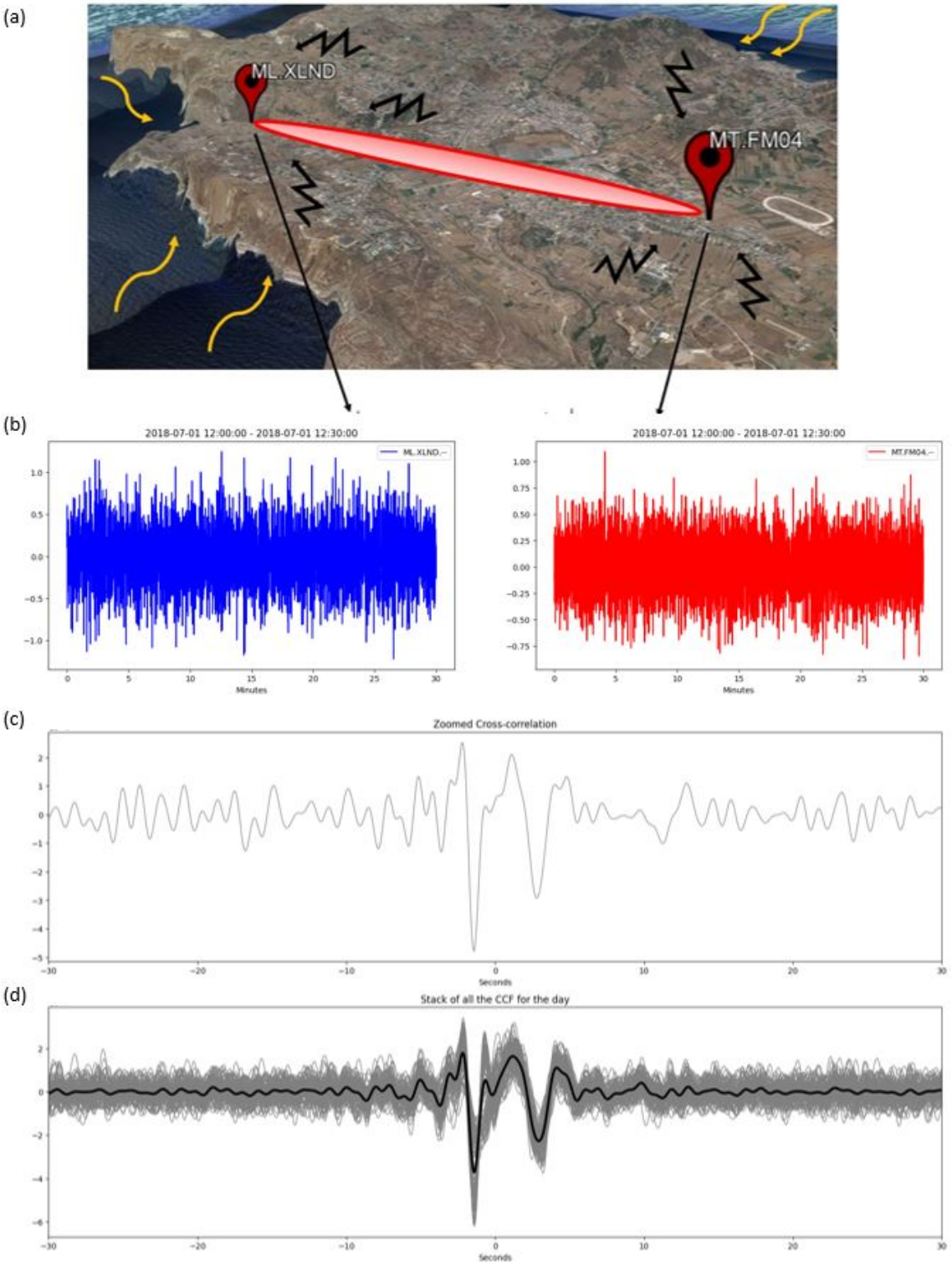

Figure 2.3.: Cross-correlation of ambient seismic noise recorded by two stations in Gozo, to yield a Green's function. The black and yellow arrows on the map in (a) represent the cultural and natural noise, respectively. The red oval shape describes the medium being sampled when cross-correlating noise recorded from stations XLND and FM04. The noise recorded by both stations is represented by the 30-minute time segments shown in blue and red in (b). Performing cross-correlation of these time series yields the Green's function or the impulse response. This is represented by the zoomed CCF in (c). Figure (d) shows the CCF processing for a whole day. The grey shading consists of 96 individual grey lines or CCFs on top of eachother. The black line is the 1-day stack of all the grey lines.

2.1.3. Analysing changes in seismic velocity over time

The analysis to determine changes in seismic velocity over time entails comparing the "current" CCF to a reference CCF, where the former represents the situation at a certain time period and the latter describes an averaged background representation of the medium being studied (Clarke et al., 2011). Two methods that obtain variations in seismic velocity from CCFs are Passive Image Interferometry (Sens-Schönfelder and Wegler, 2006; Wegler et al., 2009) and Moving-Window Cross-Spectral (MWCS) technique (Clarke et al., 2011; Ratdomopurbo and Poupinet, 1995), which operate in the time and frequency domain respectively (Clarke et al., 2011). While Wegler et al. (2009) discussed that both domains have developed popular applications with similar sensitivities, the fact that the MWCS method operates in the frequency domain acts as an advantage (Clarke et al., 2011). This is because the coherent signal bandwidth in the CCF can be distinctly interpreted in the frequency domain (Clarke et al., 2011).

Recently, techniques using ambient seismic noise have demonstrated its applicability in varying contexts, such as imaging and monitoring of the subsurface. Studies investigating changes in seismic velocity to analyse the crustal dynamics of the Earth have been conducted, such as in the context of volcanoes (Duputel et al., 2009; Sens-Schönfelder and Wegler, 2006), and in response to volcanic eruptions (Brenguier et al., 2014, 2016, 2008b; Rivet et al., 2015), earthquakes (Brenguier et al., 2008a; Taira et al., 2015; Wang et al., 2017; Wegler et al., 2009; Wegler and Sens-Schönfelder, 2007), ice sheet melts (Mordret et al., 2016), landslides (Larose et al., 2015; Mainsant et al., 2012), and wastewater injection (Yang et al., 2022). Several factors are known to alter seismic wave speeds at shallow depths, such as seasonal variations from air temperature changes (Hillers et al., 2015; Mao et al., 2019; Meier et al., 2010; Tsai, 2011), precipitation (Meier et al., 2010; Obermann et al., 2014; Sens-Schönfelder and Wegler, 2006; Tsai, 2011; Wang et al., 2017), and long-term seasonal variations of climatic origin (Lecocq et al., 2017). Essentially, variations in the speed at which these waves travel are determined by the medium through which the wave is passing, whose properties may depend on changes in groundwater content (Sens-Schönfelder and Wegler, 2006; Meier et al., 2010). In fact, changes in seismic velocity can act as a complementary tool to groundwater level monitoring in medium-sized aquifers (e.g., Clements and Denolle, 2018).

2.2. Ambient seismic noise for groundwater monitoring

Groundwater is formed by the infiltration of water into aquifers, from either surface water bodies, precipitation or surface runoff (Giordano et al., 2009). The groundwater table (labelled as GWT in Figure 2.4), which refers to the depth at which subsurface rocks are completely saturated with water, acts as a border between the upper vadose (unsaturated)

zone and lower phreatic (saturated) zone (Hiscock and Bense, 2021). The vadose zone extends from the soil surface to the water table below (Holden and Fierer, 2005). Although pores in the vadose zone are filled with both air and water, the water found between soil particles in the vadose zone is not regarded as groundwater (Giordano et al., 2009).

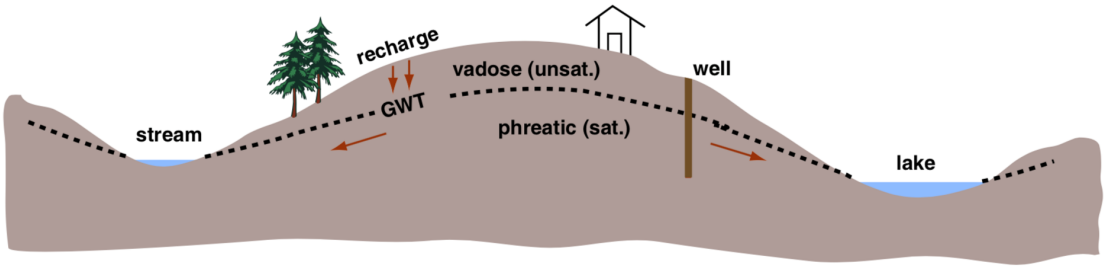

Figure 2.4.: The vadose and phreatic zones (MIT OpenCourseware, 2021). The groundwater table (GWT) refers to the depth at which subsurface rocks are completely saturated with water, and acts as a border between the upper vadose (unsaturated) zone and lower phreatic (saturated) zone (Hiscock and Bense, 2021). The water found between soil particles in the vadose zone is not regarded as groundwater since the particles are filled with both water and air (Giordano et al., 2009).

Seasonal evaporation and precipitation vary the soil moisture in the vadose zone, while simultaneous groundwater table fluctuations occur because of drainage, abstraction, and inundation (Fokker et al., 2021). Varying pore pressures at deeper rock layers are a consequence of these groundwater table fluctuations, where such pressures can be measured using conventional piezometric wells at a local scale (Fokker et al., 2021). However, adopting a regional approach on investigating subsurface pore pressure variability can be achieved with the use of seismic methods (Fokker et al., 2021), which can complement conventional borehole reading methods.

Computing the cross-correlation of ambient seismic noise recorded by two sensors may utilise real-time data from seismic stations, which allows for the continuous sampling and investigation of the medium between the sensors (Lecocq et al., 2014). Changes in the seismic velocity are indicative of changes in groundwater in underground rocks due to changes in pore pressure (Grêt et al., 2006). Water saturation in rocks will lead to an increase in pore pressure (Christensen and Wang, 1985). In turn, this leads to the opening of cracks in the rock which reduces the contact area between different grains of rock, leading to a decrease in seismic velocity (Christensen and Wang, 1985).

Analysing the changes in seismic velocity may therefore be plausibly used to monitor changes in groundwater content. This methodology does not depend on the occurrence of active seismic sources or earthquake activity to produce results because ambient seismic noise is continuous and naturally abundant (Clarke et al., 2011; Lecocq et al., 2014). While wells provide *in-situ* (or local) groundwater monitoring (Healy and Cook, 2002), seismic noise presents a volumetric and averaged sampling of the medium through which

it naturally scatters and is sensitive to hydrogeological changes within the volume. This allows for a broader representation of the aquifer under investigation when compared to the localised measurements from wells especially when the aquifer consists of a heterogeneous permeability structure (Clements and Denolle, 2018).

Numerous studies have tested this technique at different locations such as in the mountain region of the Himalayas (Illien et al., 2021), the Gräfenberg Array, Germany (Lecocq et al., 2017), the Pont Bourquin landslide in the Swiss Alps (Mainsant et al., 2012), San Gabriel Valley Basin, California (Clements and Denolle, 2018), the groundwater basins in California (Mao et al., 2022; Meier et al., 2010), the Gulf Coast Aquifer System of southern Texas (Kim and Lekic, 2019), the Crépieux-Charmy water exploitation field in the alluvial plain of the Rhone River, France (Garambois et al., 2019; Voisin et al., 2017), the Reykjanes Geothermal Reservoir, Iceland (Sánchez-Pastor et al., 2019), Merapi volcano, Indonesia (Sens-Schönfelder and Wegler, 2006, 2011), the volcanic island of O'ahu, Hawai'i (Grobbe et al., 2021), and across Japan (Wang et al., 2017). Malta is different from these locations because it is a small island (smaller than Japan and O'ahu, Hawaii) with no lakes, rivers, mountain regions, geothermal reservoirs, or watersheds. Additionally, rainfall is relatively low, and the islands are surrounded by saline water, which to a certain extent, interacts with groundwater. To our knowledge, no similar studies have yet been conducted on small islands, in particular in the Mediterranean area. In addition, ambient seismic noise provides a constant and cost-effective source of data that can be continuously used to monitor groundwater levels in the Maltese islands, and worldwide.

2.3. Geology and Hydrogeology

The geology of the Maltese islands follows a five-layer cake-like sequence, consisting of the Lower Coralline Limestone (LCL), the oldest formation, followed by Globigerina Limestone (GL), Blue Clay (BC), Greensand, and the youngest formation Upper Coralline Limestone (UCL) (Figure 2.5). The LCL is a hard, dense, and semi-crystalline limestone reaching thicknesses of 140 m in vertical cliffs in south-west Gozo, and 100 m in western and southern Malta. This is overlain by GL, which outcrops in large areas of southern and central Malta and Gozo. GL is composed of soft and fine-grained sediment, and reaches thicknesses of 207 m in southern Malta, and 23 m in southern Gozo.

The next formation in the sequence is BC, consisting of deep-water formations of marls, clays, and silty sands, in alternating pale grey and dark grey colours. The BC has been significantly eroded in the south and east of Malta, and thicknesses of approximately 75 m have been recorded in Northern Gozo and the western coast of Malta. Greensand, underlying the following UCL formation, is coarse, thickly bedded, bioclastic limestone rich in glauconite. Although it is generally observed as a layer that is a few centimetres thick, a noticeable thickness of approximately 11 m is found in Gozo. The youngest formation, the

UCL, is like the LCL in terms of the content of coralline algae and colour. The UCL can be observed as either highly competent, but also at times more fractured. Outcrops of the UCL occur in all the islands, where they are the most developed in east-central Gozo, at Comino, and in the west and north of Malta. Comprehensive descriptions on the lithostratigraphical sequence of the Maltese islands can be found in House (1961), Felix (1973), Pedley et al. (1978a), Pedley et al. (1978b), Pedley (1987), Alexander (1988), Pedley (1990), Rehfeld and Janssen (1995), Magri (2006), Baldassini and Di Stefano (2017), and Prampolini et al. (2018). As can be observed from Figure 2.5, a N-S divide in geological outcrops exists, distinguished by GL in the south of Malta and the UCL/BC in the west and north of Malta.

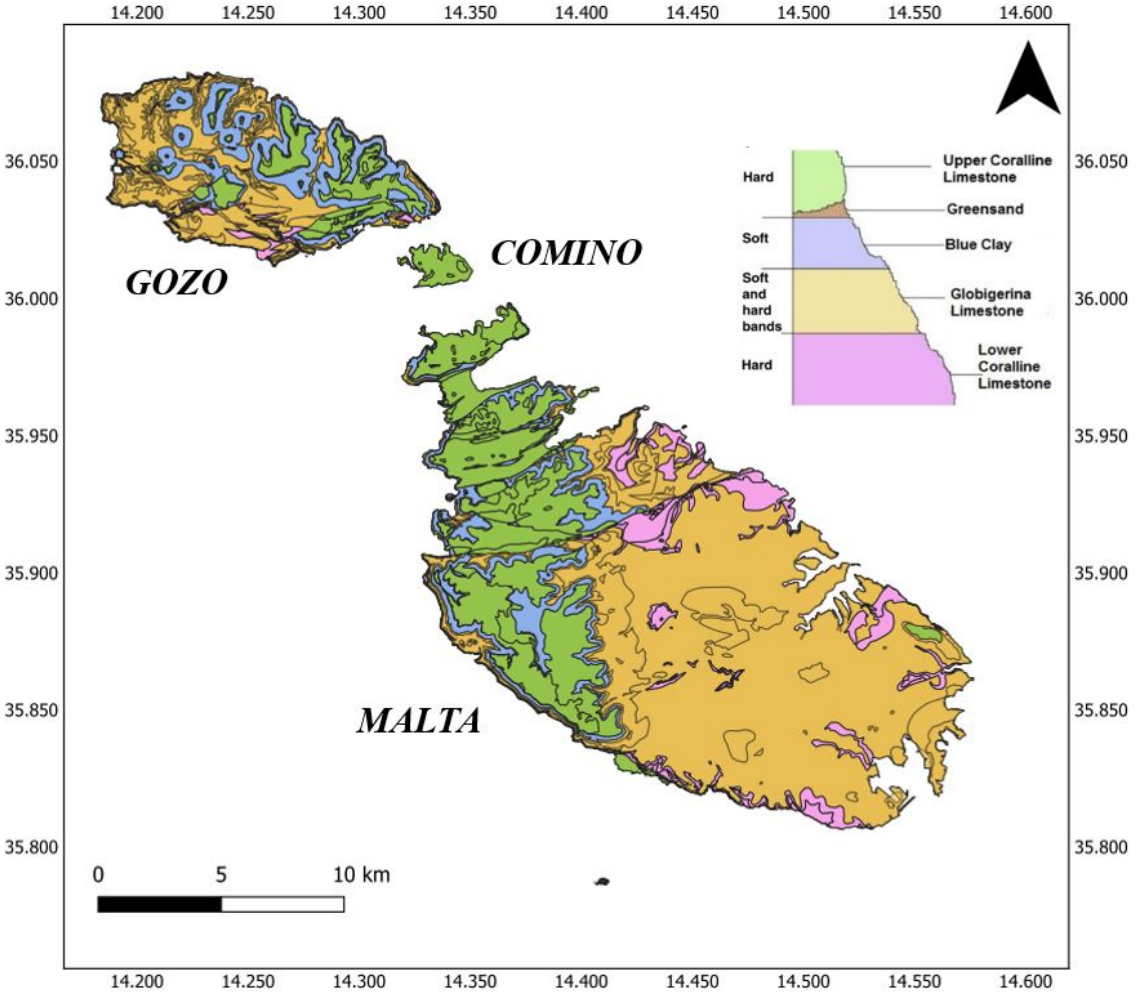

Figure 2.5.: Geological outcrop map of the Maltese islands. The top right diagram shows the colour-coded sequence of geological layers found in the Maltese islands, ranging from the oldest formation of Lower Coralline Limestone (LCL) to the youngest formation of Upper Coralline Limestone (UCL) (Continental Shelf Department, 2022).

Groundwater resources in the Maltese islands are of two typologies: the perched aquifer and the mean sea-level aquifer (MSLA) (Newbery, 1968; Alexander, 1988; Food and Agricultural Organisation, 2006; Buhagiar, 2007; Sapiano et al., 2008; National Audit Office, 2012; Sapiano, 2020). The map in Figure 2.6 shows the extent of the two aquifer

types in the Maltese islands (provided by EWA). The perched aquifer (in orange) occurs where the BC formation is present in the rock strata, which coincides with where UCL can be observed in the geological outcrop map in Figure 2.5. The MSLA (in green) is evident almost throughout the whole extent of the islands.

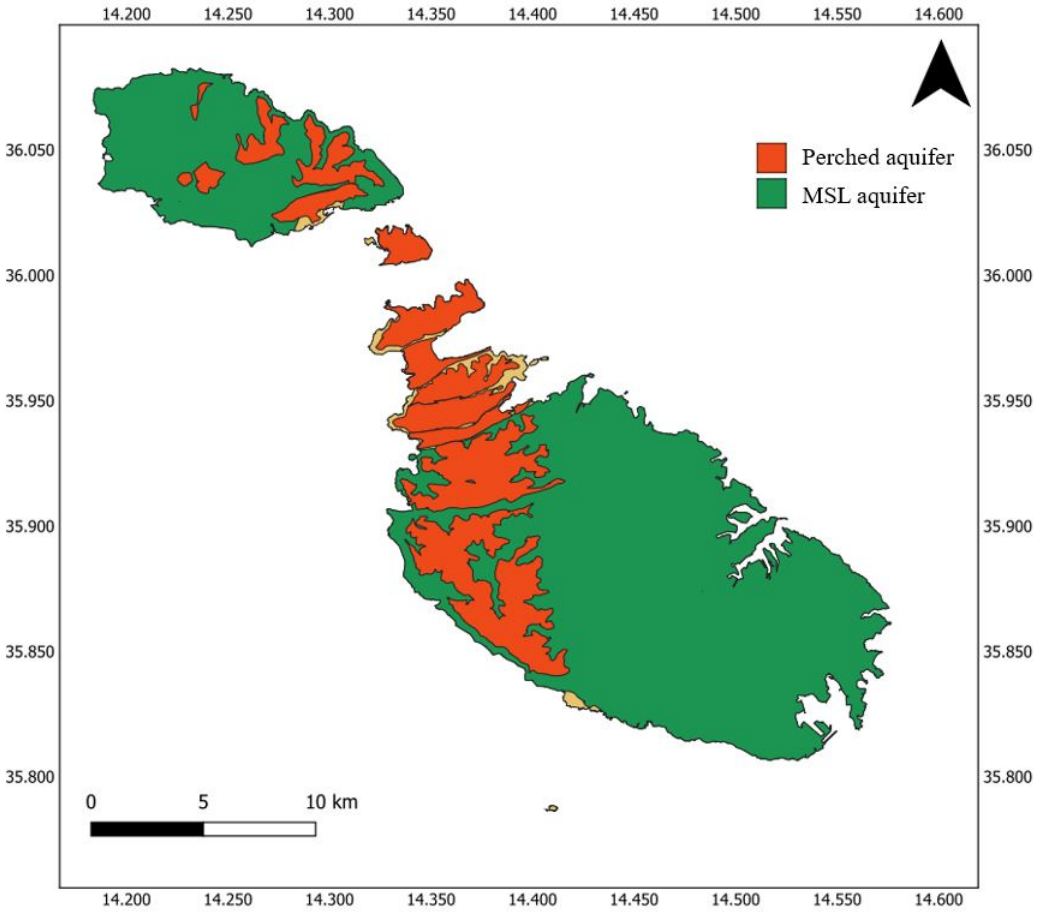

Figure 2.6.: The extent of the two main aquifer typologies in the Maltese islands; the perched aquifer in orange and the mean sea-level aquifer (MSLA) in green. The MSLA is evident throughout the islands. The perched aquifer occurs where the Blue Clay (BC) formation is present in the rock strata, which coincides with where UCL can be observed in the geological outcrop map in Figure 2.5.

2.3.1. The perched aquifer

The BC formation acts as an aquitard/aquiclude between the geological strata in the north (Newbery, 1968; Alexander, 1988). Percolating rainfall gives rise to a perched aquifer in the UCL layer overlying the BC formation (Newbery, 1968; Buhagiar, 2007; Lewis et al., 2015) (Figure 2.7). The perched aquifer depth varies from 20-50 m from ground level, and it does not suffer from saltwater intrusion due to its lack of contact with seawater (Lewis et al., 2015). This aquifer, which is mainly used for agricultural purposes, exhibits high porosity (41-45%) and low permeability (0.2-0.5 m/year), which yields a slow rate

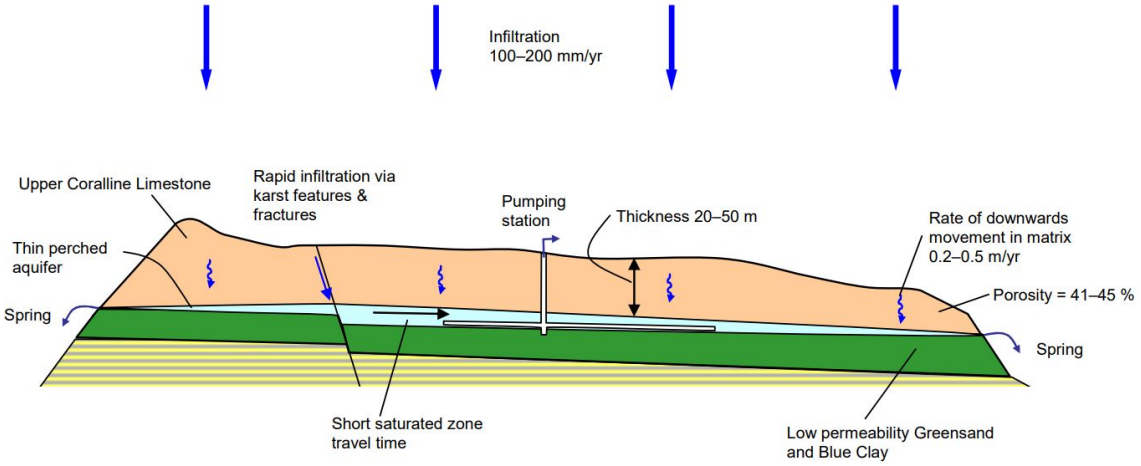

Figure 2.7.: A conceptual model of the perched aquifer and associated processes (Stuart et al., 2008). The cartoon depicts the perched aquifer found at a depth of 20–50 m below ground level. This aquifer is underlain by the BC aquitard, and springs develop at the margins of contact between the BC and UCL formations.

of downward percolation through the aquifer matrix (Lewis et al., 2015). While there are few surface waters that can be noted in the Maltese islands, springs are observed at the margins of contact between the BC and UCL formations (Newbery, 1968; Lewis et al., 2015; SEWCU, 2015). Changes in the water level of the perched aquifer are usually very small (within a couple of centimetres), and so, until now, water levels from this aquifer have not been recorded. Plans are underway for EWA to start measuring the flow rates (m^3/hour) from these springs to act as an indicator of the change in water level of the perched aquifer. Figure 2.7 shows a conceptual model of the perched aquifer and associated processes (Stuart et al., 2008; SEWCU, 2015).

2.3.2. The mean sea-level aquifer (MSLA)

The MSLA, which is the main aquifer used for the public supply of water, is mainly confined in the LCL formation at sea-level depths (Stuart et al., 2008; SEWCU, 2015), as illustrated in Figure 2.8. This aquifer consists of freshwater "floating" on top of seawater in the form of a Ghyben-Herzberg lens due to water density differences (FAO, 2006; Lewis et al., 2015). The freshwater extends below sea-level about 36 times, on average, as much as it extends above sea-level (FAO, 2006). The highest piezometric levels of this aquifer are observed at 3.387 m above mean sea-level (MSL). Piezometric levels from the central area of Malta have reached levels as low as 1 m above MSL due to groundwater abstraction (FAO, 2006; Lewis et al., 2015). Due to the MSL aquifer being prone to seawater upconing because of unsustainable groundwater abstraction, underground galleries were constructed to draw groundwater from the thin freshwater lens (Bakalowicz et al., 2003). The MSLA exhibits low porosity (7-20%) and a higher downward movement rate of 0.5-2.8 m/year,

when compared to the perched aquifer (Lewis et al., 2015). Figure 2.8 shows a conceptual model of the MSLA and associated processes (Sapiano, 2020; SEWCU, 2015).

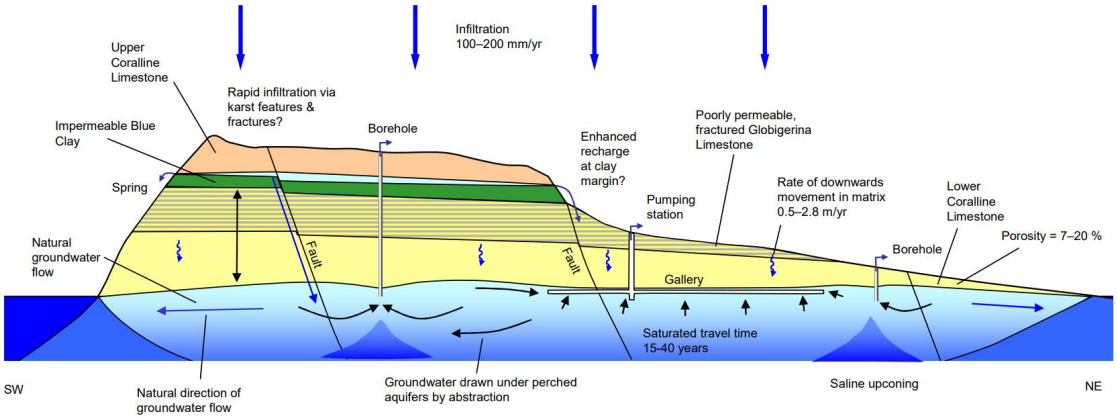

Figure 2.8.: A conceptual model of the Malta mean sea-level aquifer (MSLA) and associated processes (Stuart et al., 2008).

While the UCL allows rainfall to percolate freely, the impermeable BC formation and other marly deposits observed in the GL layer reduces water percolation speeds (Buhagiar, 2007; FAO, 2006). Still, seepage into the MSLA through the BC layer is anticipated, either from rainfall or from the overlying perched aquifer in the UCL (Alexander, 1988; FAO, 2006). This is probably due to the localised, but significant karstic evolution of rock strata in the Maltese islands, which modified the properties of the BC aquitard to allow this leakage from the UCL through the BC (FAO, 2006). Water from the perched aquifer may also contribute to the MSLA at points where the UCL is downfaulted to sea-level (FAO, 2006).

Although the fundamental sedimentary geology is a simple layer cake, normal faulting has divided the archipelago into a complex sequence of blocks and laterally discontinued formations (Galea et al., 2021). Whereas similar cross- and autocorrelation methods in other countries have dealt mostly with confined or well-defined water bodies, in Malta the changes in geology over short distances, coupled with the presence of two aquifers, may imply that the analysis and interpretation of CCFs over the whole archipelago is not straightforward. To this effect, this study acts as a proof-of-concept to determine to what extent, and with what limitations, the seismic velocity variations may be used as a proxy for groundwater variations within the Maltese islands.

3. Data

In this chapter, a description of the seismic stations and the boreholes from which ambient seismic noise and water level data were recorded will be given. As a pre-processing step, the seismic data was analysed to establish the filters to be used for the different types of stations that were available.

3.1. Seismic network data

The seismic data of the Malta Seismic Network (MSN) (Galea et al., 2021) and the "*FAglie Sismogeniche e Tsunamigeniche nei Mari ITaliani*" (FASTMIT) experiment (Bozionelos et al., 2019) was compiled into one dataset. The networks consist of a combination of eight broadband and six short-period, three-component seismic stations, respectively. All seismic stations are operated by the Seismic Monitoring and Research Group (SMRG) within the Department of Geosciences, University of Malta. The short-period stations were deployed from July 2017 to October 2018 (Bozionelos et al., 2019). Table 3.1 gives the technical specifications of the seismic stations of both seismic networks. Two of the broadband stations, HQIM and XROB, were recently installed and not used in this study. Temporary and permanent stations have network codes MT and ML, respectively. Station WDD is part of the network MN (Boschi and Morelli, 1994). Almost half of the stations (MSDA, WDD, XLND, FM01, FM02, FM04, FM06) lie either on the LCL or GL. These formations are found below the BC formation in the geological strata, i.e., below the perched aquifer (Pedley et al., 1978a). The remaining stations (CBH9, MELT, QALA, FM03 and FM05) were installed on the UCL, which lies on top of the BC. The maximum and minimum station distances between any two stations of the MSN and FASTMIT experiment are approximately 35 km and 3 km, respectively (Galea et al., 2021). Figure 3.1 shows the location of the seismic stations; the red triangles indicate the stations of the MSN, whereas the inverted purple triangles indicate the FASTMIT network stations. The elevation map in Figure 3.1 (provided by EWA) indicates that the highest elevation (yellower shading) is found in the western part of mainland Malta. The site selection criteria for the seismic stations were reviewed in a number of studies (Agius et al., 2015; Bozionelos et al., 2019; Galea et al., 2021).

The broadband stations record data at multiple sampling frequencies such as the HH (100 sps) and BH (20 sps). The short-period stations only record data at the HH (125 sps) sampling frequency. To limit the size of the dataset, the BH channels of the broadband stations were chosen for the processing.

Table 3.1. Technical specifications of the seismic stations of the Malta Seismic Network (MSN) and the "*FAglie Sismogeniche e Tsunamigeniche nei mari ITaliani*" (FASTMIT) network (Bozionelos et al., 2019; Galea et al., 2021)

Network code	Station name	Latitude (°)	Longitude (°)	Elevation (m)	Surface geology	Sensor and Digitizer
MT/ML	CBH9	36.0140	14.3314	27	UCL	Trillium Compact, Centaur
MT/ML	MELT	35.9747	14.3427	98	UCL	Trillium 120PA, Centaur
ML	MSDA	35.9012	14.4839	48	GL	Trillium 120PA, Centaur
ML	QALA	36.0349	14.3202	91	UCL	Trillium Compact, Centaur
MN	WDD	35.8375	14.5246	15	GL	STS-2, Quanterra
ML	XLND	36.0323	14.2200	6	LCL	Trillium Compact, Centaur
MT	FM01	35.8276	14.4426	128	LCL	Lennartz, RefTek
MT	FM02	35.8569	14.4467	95	GL	Lennartz, RefTek
MT	FM03	35.8845	14.4043	190	UCL	Lennartz, RefTek
MT	FM04	36.0342	14.2647	105	GL	Lennartz, RefTek
MT	FM05	35.8959	14.3492	205	UCL	Lennartz, RefTek
MT	FM06	35.9411	14.4208	6	LCL	Lennartz, RefTek

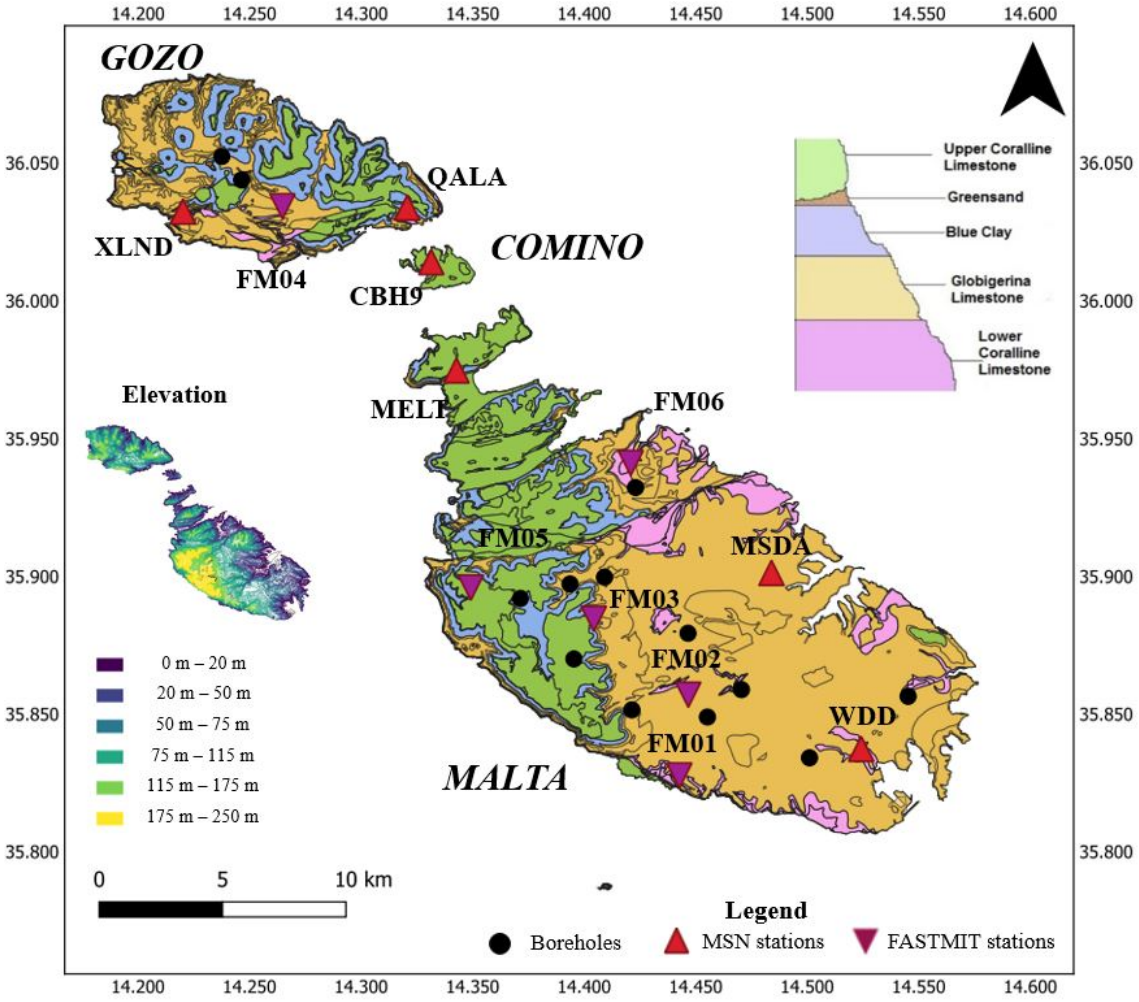

Figure 3.1.: Geological outcrop and elevation map of the Maltese islands (Continental Shelf Department), with the locations of the seismic stations and the boreholes. The red and inverted purple triangles indicate the location of the stations of the MSN and FASTMIT network, respectively. The black dots indicate the location of the boreholes from which water level data was recorded (see Section 3.3). The elevation map indicates that the highest elevation (yellower shading) is found int the western part of mainland Malta.

3.2. Spectral analysis

Power spectral density (PSD) provides information on the spectral content present in the seismic data. PSDs give an estimation of how power is distributed, according to the frequency of the recorded noise (e.g., McNamara and Buland, 2004). In order to study the distribution of the PSD of the seismic data, PSD plots were generated for each station per day. The patterns are compared to global low noise-model (LNM) and high noise-model (HNM) references. This is a powerful tool to determine the overall performance and sensitivity to the data of each station. The evaluation of the PSDs is highly important in the case here because the dataset consists of noise from two types of stations; broadband and short-period. The different frequencies recorded on a seismograph originate from different sources such as earthquakes or ambient seismic noise, which generate different spectral signatures. Analysing the spectral content over a number of weeks or months also gives insight to seasonal weather changes and cultural noise that could be picked up by seismic stations.

An example of a 24-hour PSD chart for the station MSDA on 2018-05-01 is shown in Figure 3.2. The y-axis is the amplitude, or the power of the noise and the x-axis represents the period. The graphs are built up from stacked curves, each of which representing 30 minutes of data, and the code processes the power for every frequency. The colour bar on the right of the plot represents the density of the PSD curves, with a lighter colour depicting higher densities of curves plotted on top of each other. The grey lines in the plot represent the LNM and the HNM references (Peterson, 1993), which gives an indication of station performance with respect to ambient seismic noise. Since the BH (20 sps) sampling stream was used for the broadband stations, the maximum frequency that can be observed (Nyquist frequency) is 10 Hz. Therefore, the x-axis of the PSD plot starts from 0.1 s. On this particular day, each PSD curve can be observed to fall within the noise levels, which indicates satisfactory performance of the station. Since Malta is an island, microseisms recorded by the seismic stations are dominated by the noise generated by continuous sea swells that crash into the coast (e.g., Agius et al., 2014). PSD curves peak at 1-2 s with very little scatter, corresponding to periods of ocean microseisms. A second peak at around a period of 3 s, with considerable scatter over the day, is visible on all stations (Figures 3.3 and 3.4), possibly being caused by storm activity reported on the previous day, with wave action dying down gradually. Cultural and ocean microseism noise typically correspond to a period of $\sim$0.1-1 s and $\sim$1-10 s, respectively (e.g., Agius et al., 2014).

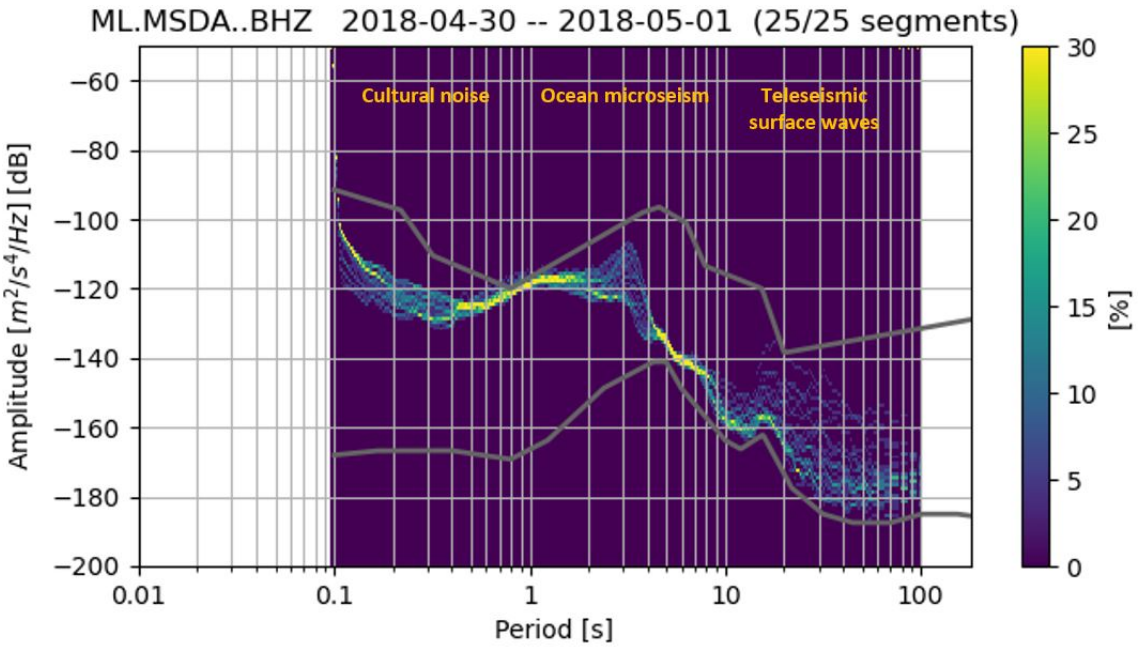

Figure 3.2.: Power spectral density (PSD) chart for a broadband station. The chart is computed for the noise recorded by station MSDA on 2018-05-01. The recorded noise in the 0.1-1 s and 1-10 s periods are typical of cultural noise and ocean microseisms, respectively. The colour bar on the right of the plot represents the density of the PSD curves, with a lighter colour depicting higher densities of curves plotted on top of each other.

To check for patterns in the distribution of amplitude of all broadband stations, Figure 3.3 shows PSD charts for broadband stations for the date 2018-05-01. All broadband stations show the same pattern for the distribution of amplitude. Most microseismic energy has a period range of 1-10 s, and is of more interest for this study.

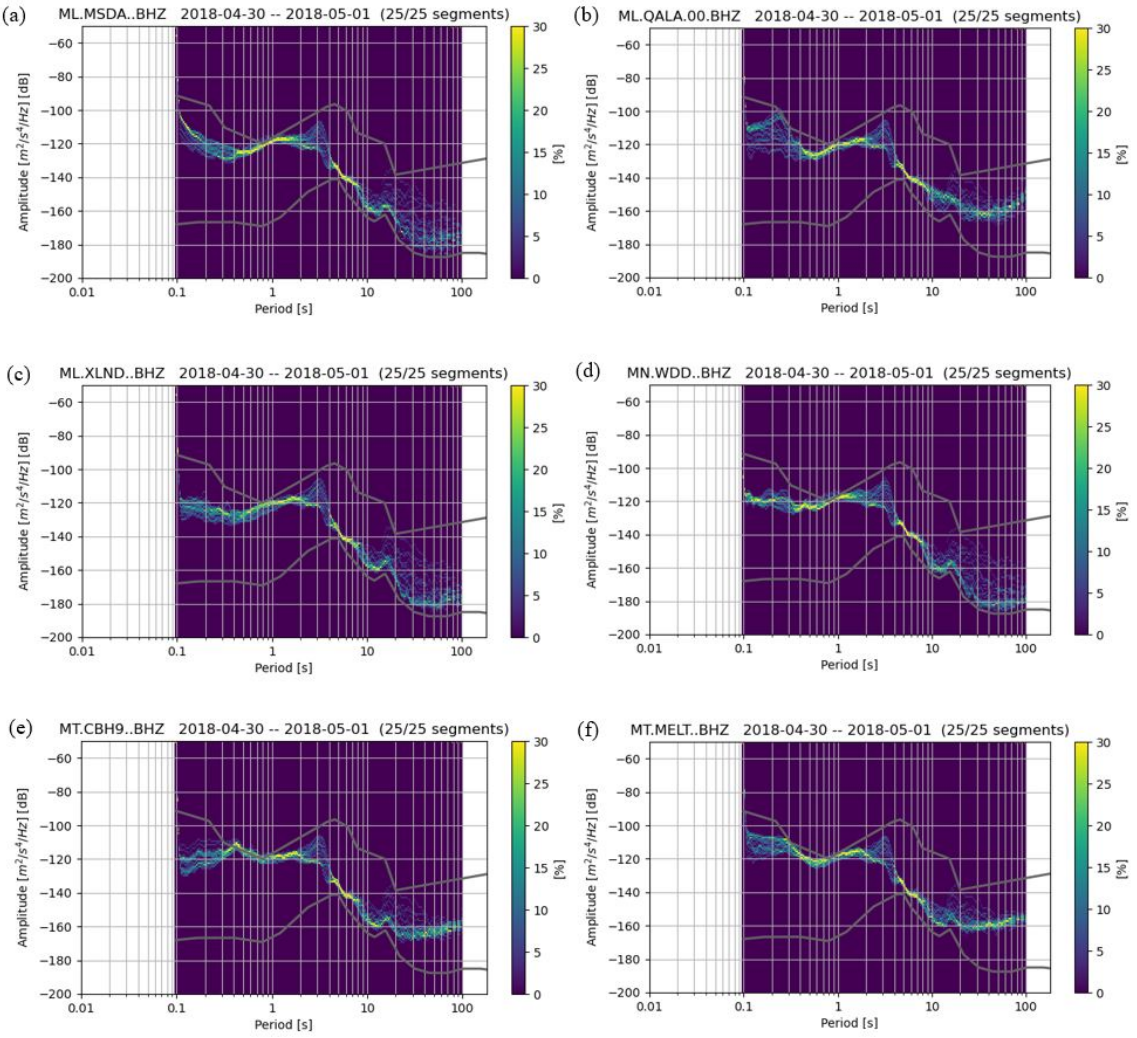

Figure 3.3.: PSD charts for all broadband stations: (a) MSDA, (b) QALA, (c) XLND, (d) WDD, (e) CBH9, and (f) MELT for the day 2018-05-01. See Figure 3.2 for details on colour bars.

PSD charts for the short-period stations for the same date 2018-05-01 are shown in Figure 3.4. Again, all stations show the same pattern for the distribution of amplitude, and the PSD curves peak at 1-2 s with very little scatter. The seismic data of the FASTMIT stations was recorded in the HH sampling stream (125 sps), which means that the Nyquist frequency is 62.5 Hz. Therefore, the x-axis of the plot starts at the 0.016 s period. The cut-off period of these short period stations is at 3-4 s, where the PSD is observed to increase rapidly. This suggests that the instrument is not responsive to the ground vibrations beyond this period, as expected, and thus is unsuitable below about 0.3 Hz. All the PSD charts in Figure 3.4 exhibit the same cut-off period. The short-period stations are shown to be sensitive to the peak at 3 s, which was possibly because of storm activity on the day.

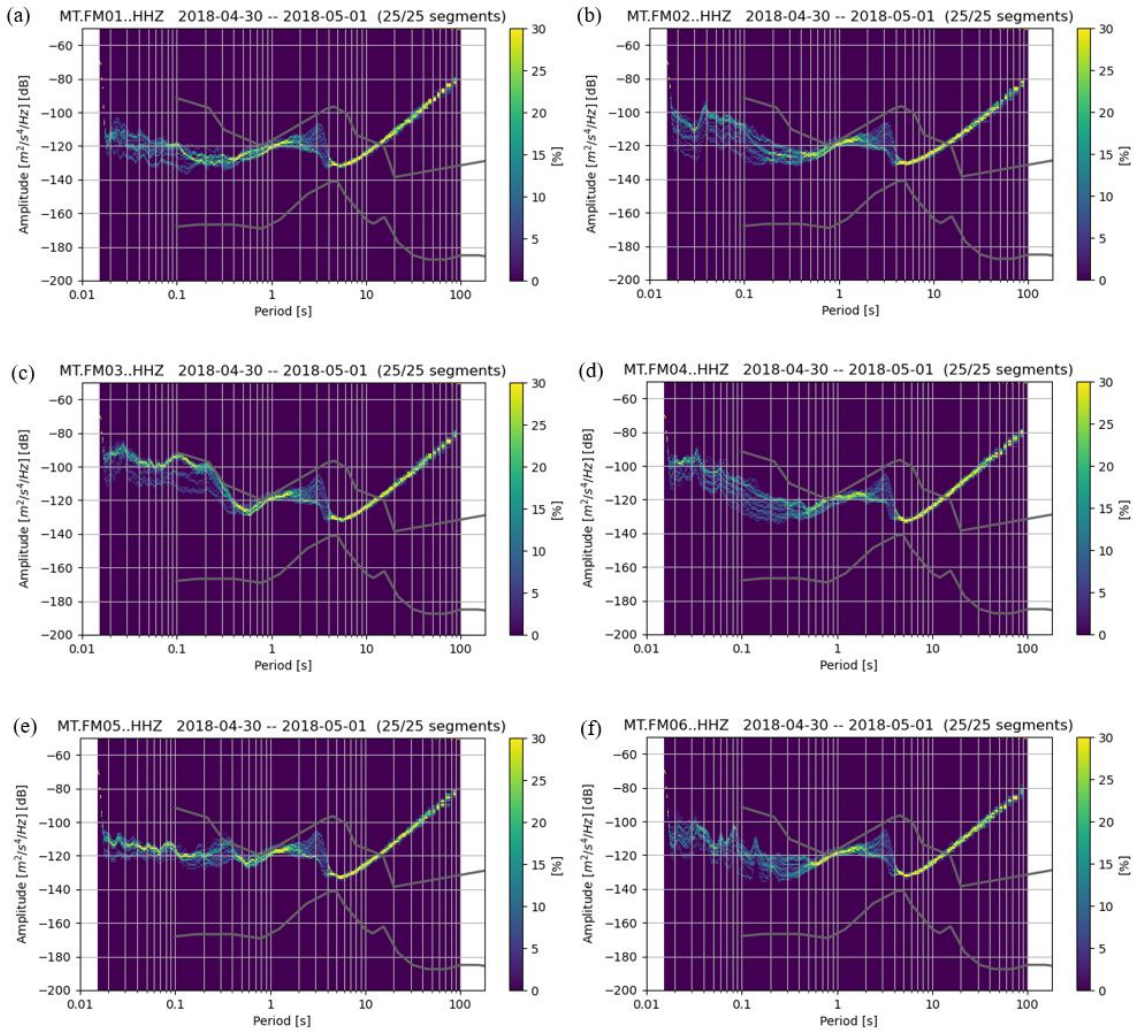

Figure 3.4.: PSD charts for all short-period stations: (a) FM01, (b) FM02, (c) FM03, (d) FM04, (e) FM05, and (f) FM06, for the day 2018-05-01. See Figure 3.2 for details on colour bars.

To investigate the difference in the spectral power between summer and winter periods, the PSDs of two representative dates were compared. Figures 3.5a and b show the PSD charts for the MSDA station for the days 2017-12-22 and 2018-06-22, respectively. Figures 3.5c and d show the PSD charts for the FM01 station for the same dates. Although the distributions are quite different from the previous graphs, the microseismic noise still peaks in the region of 1-5 s. The power distribution of the MSDA station PSD from 1-10 s (0.1-1 Hz) and the FM01 station PSD from 0.3-3.3s (0.3-3 Hz) is shown to decrease in the summer months when compared to winter since ocean microseisms are stronger during the winter months.

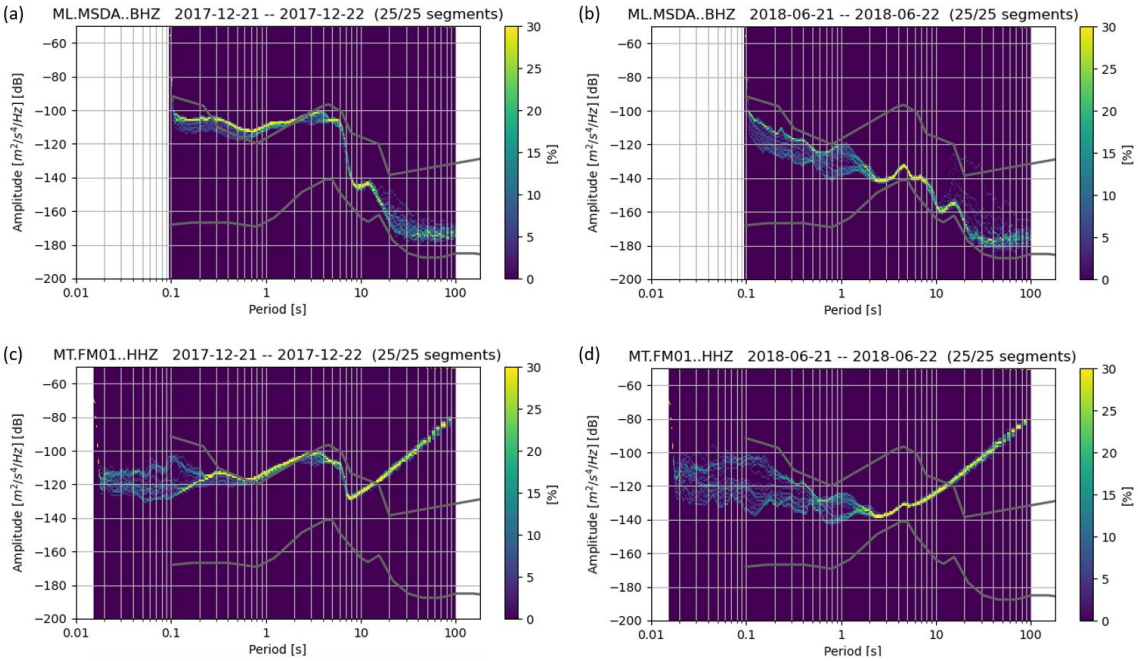

Figure 3.5.: Example of spectral difference between winter and summer. PSD charts for the station MSDA for the day (a) 2017-12-22 (winter) (b) 2018-06-22 (summer) and for the station FM01 for the day (c) 2017-12-22, (d) 2018-06-22. See Figure 3.2 for details on colour bars.

The PSD analysis was useful in setting up the filter bands to be used for analysing the seismic data. It was deemed fit to have two filters, one for the broadband and one for the short-period stations, at 0.1-1.0 Hz and 0.3-3.0 Hz, respectively. The results are discussed in Chapter 5.

3.3. Borehole data

Water level data was compiled from 2016 till the end of 2021 from a number of boreholes in Malta and Gozo that are managed by the WSC and EWA. Table 3.2 lists some specifications about every borehole, such as the borehole ID, name, locality, the elevation of the top

Table 3.2. Specifications of the boreholes managed by the Water Services Corporation (WSC) and Energy and Water Agency (EWA), from which water level data was recorded.

ID	Name	Locality	Elevation (m)	Water level (m above MSL)
10035	Buqana	Mosta	93	1.910-2.789
10058	Gholja 1	Siġġiewi	152	1.299-2.276
10077	Wied il-Qliegha	Rabat	107	1.769-3.387
10078	Gomerino	Rabat	159	1.617-2.281
10081	Kandja	Siġġiewi	78	0.434-2.548
10089	L-Gharbi	Żebbuġ	83	1.232-2.276
10097	Karwija 1	Safi	77	1.003-1.564
10224	Mdawra 1	Burmarrad	9	0.597-1.635
10271	Buskett	Rabat	195	1.860-2.645
10300	Hal-Farruġ	Luqa	68	2.069-2.774
10353	Hal-Tmiem	Żejtun	51	0.279-0.959
10821	Wied Sara	Gozo	59	0.617-1.241
10866	Republic Street	Gozo	75	0.805-1.403

of the borehole above MSL (m), and the range of water level measurements recorded at that borehole (in m above MSL). Figure 3.6 shows a map of the locations of the boreholes from which water level data was recorded.

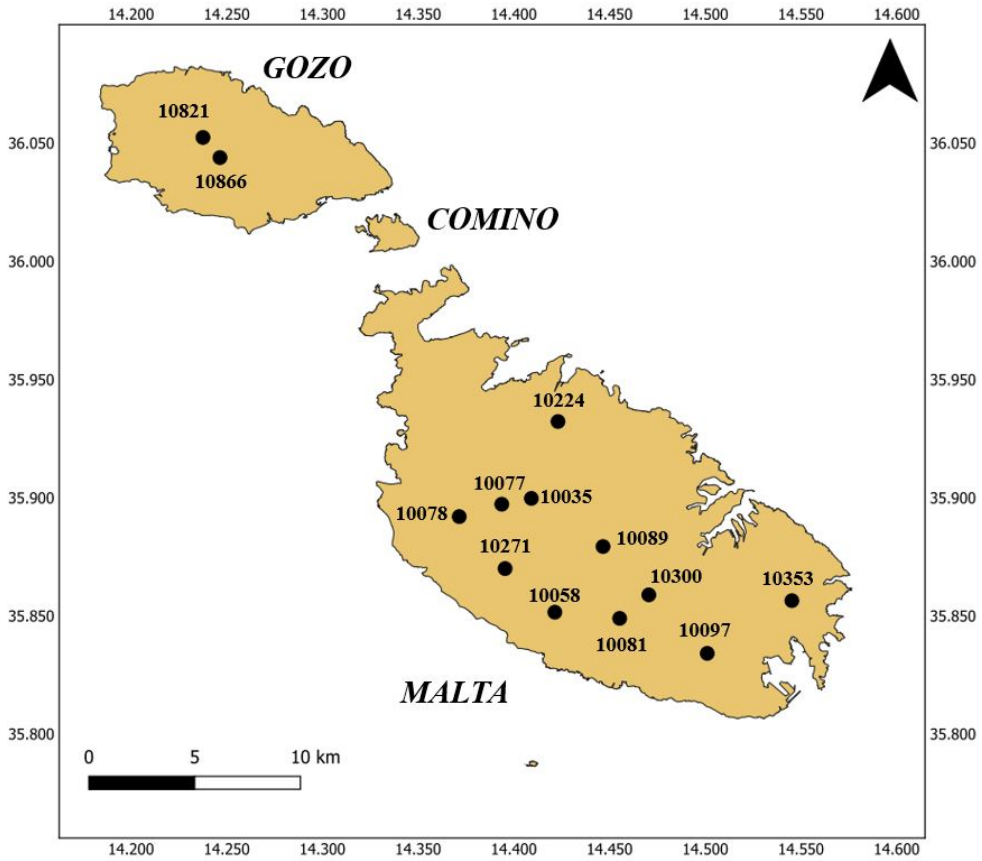

Figure 3.6.: Map showing the locations of the boreholes (provided by the Energy and Water Agency). The black dots indicate the locations of the boreholes from which water level data was obtained. The numbers adjacent to each borehole represent the borehole ID (see Table 3.2).

Patterns in the seasonal variation of water levels from each borehole were identified. Lower water levels were generally recorded in the summer months, and higher water levels in the winter months. Figure 3.7 shows a water level plot (in metres above MSL) for all the boreholes that were used in this study, where each plot represents data with a 30-day rolling average. Generally, all the water level plots in Figure 3.7 exhibit similar seasonal variations from 2016 to the end of 2021. This data does not consider any changes in the water level from the perched aquifer, but only from the MSLA because the borehole sensors are all found at the level of the MSLA. The dates of the *x*-axis represent the first day of the year.

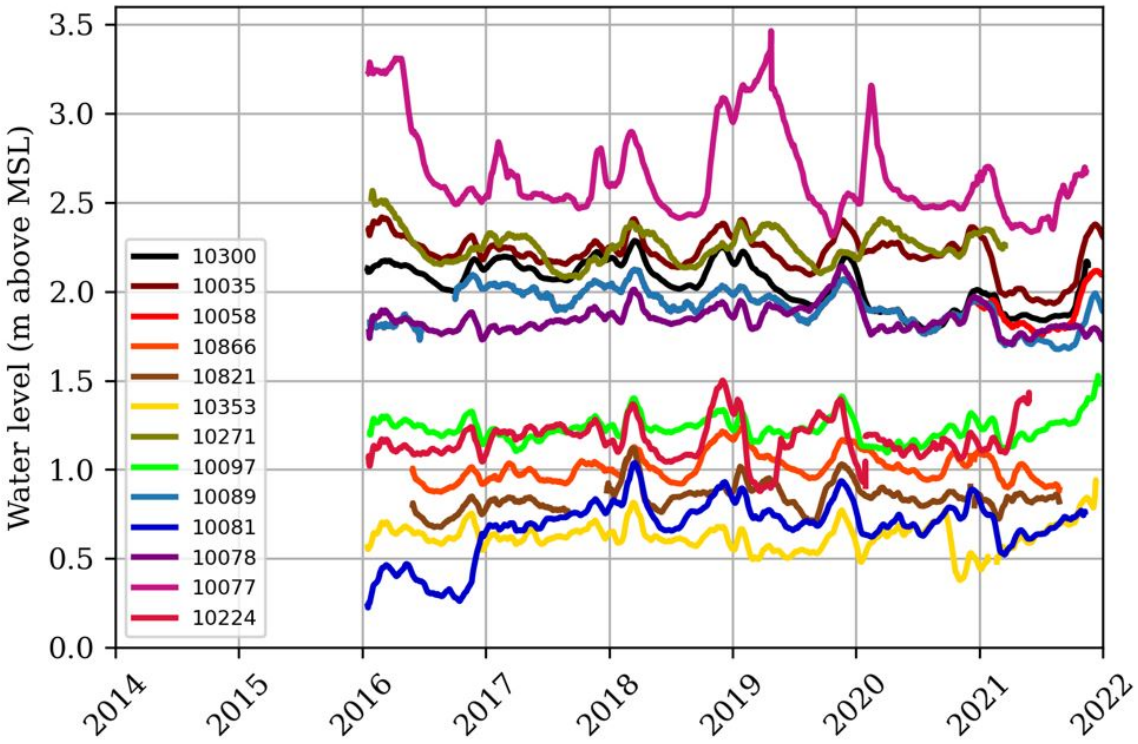

Figure 3.7.: Water level plots (in metres above mean sea-level) for every borehole from 2016 till the end of 2021. Each plot represents data with a rolling average of 30 days. The dates of the x-axis represent the first day of the year.

Generally, boreholes located closer to the shore exhibit lower ranges of water level change data. For example, water level data from borehole 10353 (Hal-Tmiem), 10821 (Wied Sara, Gozo) and 10866 (Republic Street, Gozo) range from 0.279-0.959 m, 0.617-1.241 m and 0.805-1.403 m respectively. On the other hand, greater water levels above MSL can be observed inland, in the centre of Malta (farther away from the coast). In fact, boreholes 10077 (Wied il-Qliegha), 10035 (Buqana), 10300 (Hal-Farrug), and 10089 (L-Gharbi) range from 1.769-3.387 m, 1.910-2.789 m, 2.069-2.774 m and 1.232-2.276 m respectively. However, proximity to the coast is not the sole factor that may affect the water level data from boreholes, since the extent of groundwater abstraction for agricultural purposes and its effect on the water level data is not taken into consideration in the present

study. For example, Figure 3.8 shows a water level plot of a borehole that is constantly affected by groundwater abstraction from other nearby boreholes. The episodes of groundwater abstraction from nearby boreholes are noticeable by the scatter points below the trend suggestive of a sudden decrease in water level. Most groundwater abstraction occurs in the summer periods (indicated by the vertical white bands), when rainfall is scarcer.

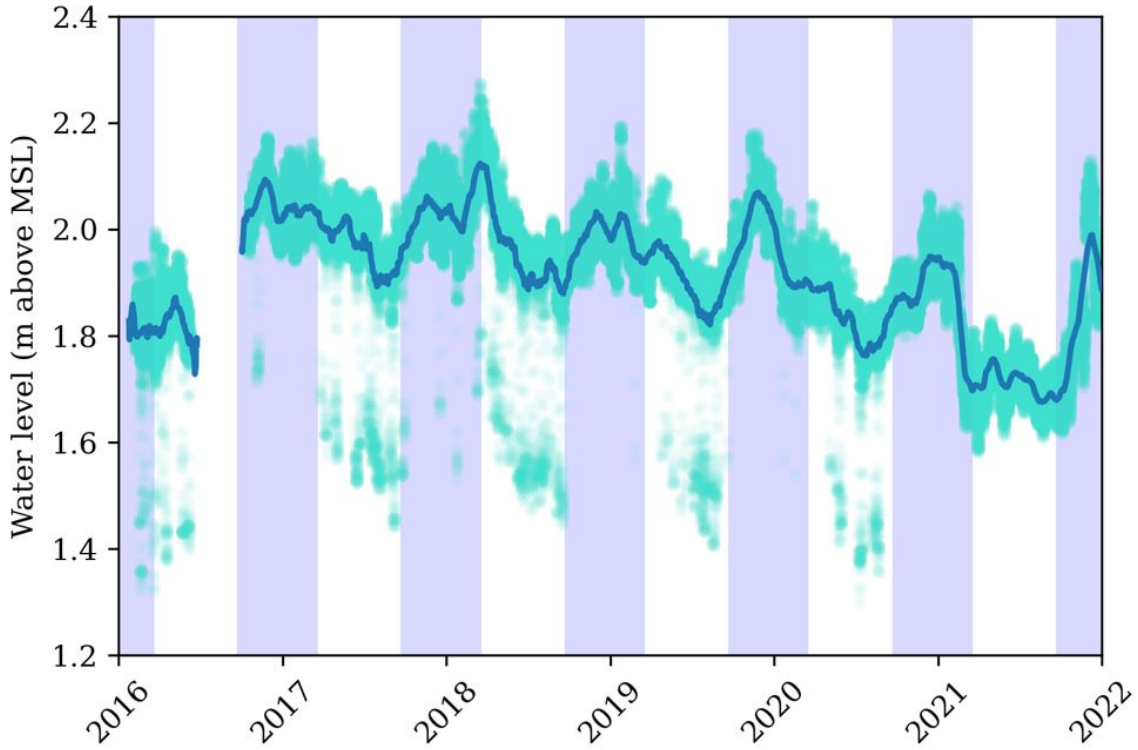

Figure 3.8.: Example of sudden groundwater level changes due to nearby abstraction. A water level plot from borehole 10089 (L-Gharbi), which shows the groundwater abstraction that has been recorded. The alternating light blue and white shading in the plot indicate the winter and summer periods, respectively. The scatter points below the trend line indicate a sudden decrease in water level from groundwater abstraction. Most groundwater abstraction occurs in the summer periods, when rainfall is scarcer. The trend is determined from a 30-day rolling average.

Apart from groundwater abstraction, there are other factors that may affect groundwater levels. For example, the amount of water from precipitation that percolates into the underground, shallow rock layers depends on the degree of surface runoff exhibited in the area. For example, urban regions tend to exhibit lower groundwater recharge rates (and more surface runoff) when compared to more agricultural ones, due to a higher degree of impervious areas (Niemczynowicz, 1999). In agricultural areas, the types of agricultural practices used, and soil properties such as texture, porosity, bulk density and hydraulic conductivity all determine how much rainwater percolates into groundwater (Owuor et al., 2016). Agricultural practices and soil properties are variable from one area to another, which may also contribute to varying levels of surface runoff and hence, water levels from boreholes. The geological setting of the boreholes is shown in Figure 3.1.

4. Methods

The MSNoise (Measuring with Seismic Noise) program (Lecocq et al., 2014), was used for the data management and processing. MSNoise is a complete Python package capable of extracting signal from noise, and that determines changes in seismic velocity using ambient seismic noise. To monitor changes in seismic velocities in the Earth's interior, MSNoise computes the CCFs of ambient noise time series recorded by seismic stations. MSNoise then determines small changes in the seismic velocity (delay times) between the CCFs and a reference CCF (Lecocq et al., 2014). The Python programming language (version 3.9.13) and the module ObsPy (version 1.3.0) from Beyreuther et al. (2010) were installed to run MSNoise (version 1.6). The seismic waveforms, stored in the Standard for the Exchange of Earthquake Data (SEED) format, were compiled in a SeisComp Data Structure. A Structured Query Language (SQL) database connection was also required, in this case MySQL, as recommended by Lecocq et al. (2014). Figure 4.1 shows the workflow steps that were followed in this study.

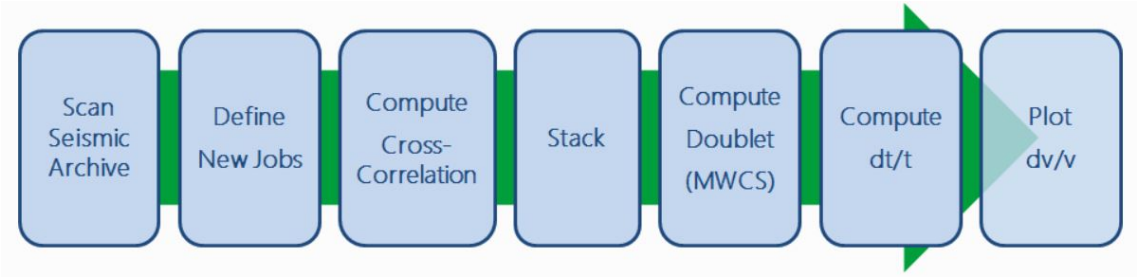

Figure 4.1.: MSNoise workflow steps, from the scanning of the seismic archive to finally plotting $\delta v/v$ (Lecocq et al., 2014)

Here, each step and the configuration used to run MSNoise will be discussed. In the following sections, plots that were generated by MSNoise that help in visualising the generated cross- and autocorrelation functions and their quality, will be shown. See Appendix A for details on the chosen configuration parameters when running MSNoise.

4.1. Data compilation

The first step was to populate the *stations* table with all the recognised networks, stations and channels after the data archive was rapidly scanned. The *network* and *channels* configuration settings were set to all the networks and channels available, and the *startdate* and

enddate parameters were set to 2016-01-01 and 2021-12-31 respectively, which spanned the total extent of seismic noise data availability. In this data discovery step, the identified files were inserted in the data availability table (Figure 4.2) of the dataset used in this study. The broadband stations have data availability spanning from 2016 to the end of 2021, while the short-period FASTMIT stations were only operational for around 14 months from the end of July 2017 to October 2018. Gaps in the data are generally caused by internet or power outage, or stations being shutdown for maintenance. The bottom plot of Figure 4.2 shows the number of stations (N) that have data available during a specific time period, where almost all the stations had data available from November 2017 to September 2018.

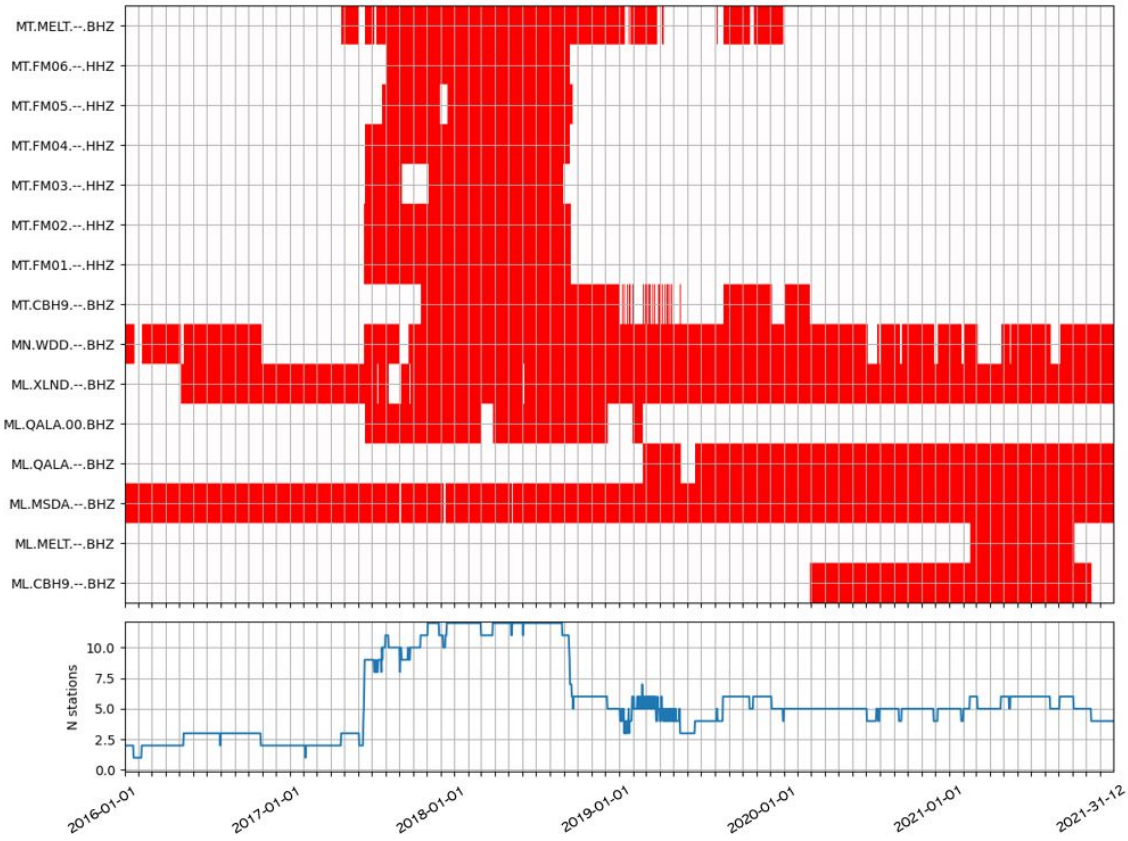

Figure 4.2.: Data availability plot from all the seismic stations from 2016-01-01 to 2021-12-31. The top plot represents the data availability for each station (red bars), and the bottom plot represents the number of stations (N) that have data available during a specific time period.

4.2. Job Definition

The scanning of the seismic archive was then followed by the job definition, where the days and station pairs that need to be processed for the files in the database are defined. In this step, MSNoise checks whether other stations are available for each date in the configured range. The jobs that were defined were inserted in the *jobs* table of the database. Equation

4.1 gives the total number of autocorrelation and cross-correlation station pairs (M) for the number of stations available (N):

$$M = \frac{N(N-1)}{2} + N \tag{4.1}$$

Therefore, the 12 stations yielded a total of 78 station pairs; 66 cross-correlations and 12 autocorrelations.

4.3. Waveform pre-processing

Before computing the CCFs the waveforms were pre-processed automatically as per MSNoise workflow (Figure 4.3).

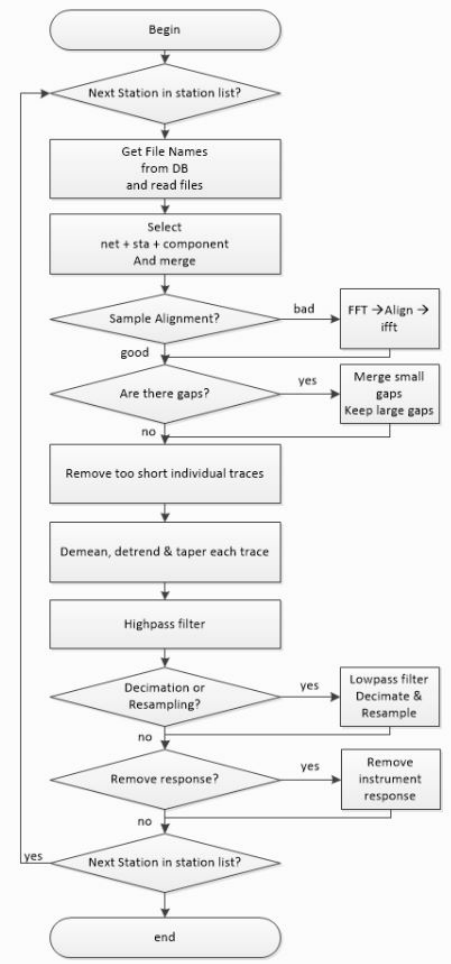

Figure 4.3.: Waveform pre-processing workflow before cross-correlation computations (Lecocq et al., 2014)

Initially, the daily miniSEED (MSEED) files of each individual station were read and

the possible combination of station pairs were identified. The station pairs were divided into separate stations and the station list was created. The file paths were obtained through the querying of the database. Daily MSEED files were opened for each station. The data was then checked for alignment on the sampling grid, and for gaps. If the data required sample alignment, it was first tapered and phase-shifted into the frequency domain using a Fast Fourier Transform. The data traces were then passed back to the time domain using an Inverse Fast Fourier Transform. In the unlikely case when the seismic data was split due to gaps, the split traces were merged to form a continuous single day trace. Moreover, *preprocess_max_gap* was set to 10 seconds, which means that gaps of 10 seconds or less were filled with interpolated values, while gaps greater than 10 seconds were not interpolated. Traces were padded with zeroes whenever they were shorter than 1 day. If they were longer than 1 day, traces were cut to fit the relevant start and end of the day. The data was pre-processed by demeaning (setting the mean of the traces to zero), detrending (removal of any trends in the data traces), and tapering (*preprocess_taper_length* at 20 seconds). Each day-long trace was then band-pass filtered (*preprocess_highpass* and *preprocess_lowpass* at 0.01 and 8 Hz, respectively) and downsampled (*resampling_method* was set to the Lanczos, or downsampling option). Although decimation is faster than downsampling, the latter does not only allow data to be downsampled at integer factors only (like decimation), but also at any factor. Instrument response was then removed from each trace. Instrument correction was removed by performing bandpass pre-filtering in the frequency domain (before multiplying with the inverse spectrum). This was done by setting *response_prefilt* to 0.005 Hz, 0.006 Hz, 30.0 Hz, and 35.0 Hz respectively. These four frequencies are the corner frequencies of the frequency taper.

4.4. Processing

In Section 3.2, the broadband and short-period stations exhibited different PSD charts. This led to specific tests on the type of filters to be used for further processing, particularly for the cross- and autocorrelations of the short-period stations. Therefore, different filters were tested and eventually chosen for the different types of stations. Four processing runs were completed in total. In two of the runs, the data from all the stations was filtered at 0.1-1 Hz for the cross- and autocorrelations of the broadband stations. In the other two runs the data was filtered at 0.3-3 Hz, to cater for the cross- and autocorrelations of the short-period stations. Before deciding on these filters, higher frequencies were also tested on the data (at 0.5-5 Hz and 0.01-10 Hz). Since a number of processing runs were completed using different parameters, the following sections will detail the configuration steps completed for each run.

Figure 4.4 shows a CCF spectrum against time plot for a cross-correlation between a broadband (XLND) and short-period (FM04) station, for the two tested filters. While the PSD charts show the spectrum of the raw data before filtering and processing, these CCF spectrum plots show the spectral energy of the CCF for each day after filtering and processing. Each black trace represents a CCFs' spectrum. The y- and x-axis represent the date and frequency of the CCF, respectively.

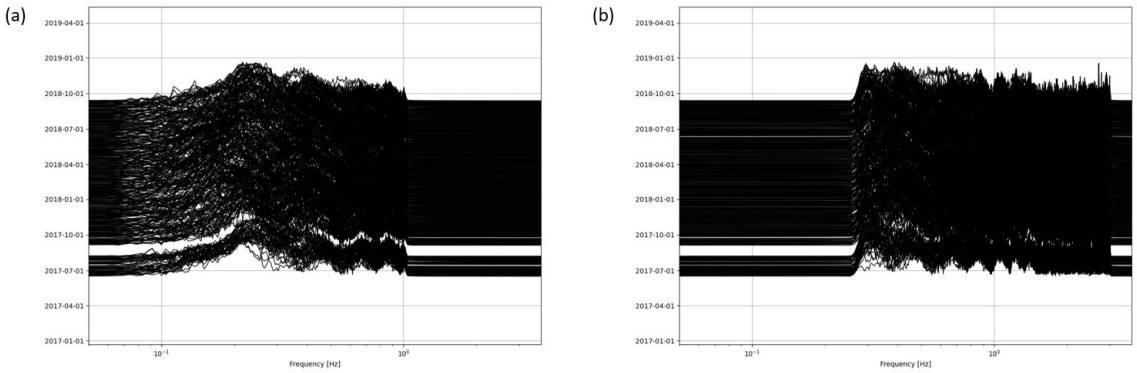

Figure 4.4.: Spectrum against time plot for the cross-correlation between a broadband (XLND) and short-period (FM04) station at different filters: (a) 0.1-1 Hz (b) 0.3-3 Hz. Each black trace represents the spectrum of a cross-correlation function (CCF). The y- and x-axis represent the date and frequency of the CCF respectively.

The next step in the workflow is the computation of the CCFs. An advantage of MSNoise is that it can run multiple processes in parallel allowing for faster execution of large datasets. The *analysis_duration* and *cc_samping_rate* for cross-correlation were set to 1 day and 20 Hz respectively. The components to compute (*components_to_compute* and *components_to_compute_single_station*), were set to the vertical component (Z) and the filtering range were specified for every filter. The cross-correlation and autocorrelation type were also specified, if they were required to be computed during that specific filter (*cc_type*, *cc_type_single_station_AC*). The maximum lag (*maxlag*) was set to 120 seconds, and each window was of 30 minutes length (*corr_duration* set to 1800 seconds) and an overlap of 0.5 (i.e., 15 minutes).

Station pairs are processed in a sequential manner. The CCFs were processed according to the different filters for each defined 30 minute window. For each of these windows in the signal, and for each of the filters previously mentioned, windsorizing (Tukey, 1962) of three times the root-mean-square (RMS) (*windsorizing* set to 3) was applied to the traces. This was completed to attenuate the effects of seismic events of varying extents, which cause parastic signals in the traces (e.g., Lecocq et al., 2014). The amplitudes of the traces were then whitened in the frequency domain between two configured frequency bounds. In this case, *whitening* was performed for all stations, except for auto-correlation, and the *whitening_type* was configured as brutal, which amplifies the signal to an amplitude of 1.

Equation 4.2 shows the cross-correlation (cc) of two time series $a(t)$ and $b(t)$:

$$cc_k = \frac{1}{N+M-1} \sum_p a_p b_{k+p} \tag{4.2}$$

where k is the lag, N and M represent the lengths of a and b respectively (Gubbins, 2004). The sum is taken over all possible products of N+M+1. Equation 4.3 defines autocorrelation (ac), which involves the cross-correlation of a time series recorded from a single station with itself:

$$ac_k = \frac{1}{2N-1} \sum_p a_p a_{k+p} \tag{4.3}$$

The CCF was completed in the frequency domain, once both traces were ready. Consider that $A(f)$ and $B(f)$ are the Fourier transforms of $a(t)$ and $b(t)$, respectively. Equation 4.4 defines the correlation function:

$$C(f) = A^*(f) \times B(f) \tag{4.4}$$

where $A^*(f)$ is the complex conjugate of $A(f)$. An autocorrelation would be computed if $a(t)$ and $b(t)$ were equal. An inverse Fourier transform was applied to $C(f)$ to get $c(t)$. Data for time lags can be found in the returned function, which corresponds to the maximum time lag (120 seconds in this case) in the negative (acausal) and positive (causal) time lags.

Figure 4.5 shows a CCF against time lag plot for the cross-correlation of two broadband stations (MSDA and CBH9). This plot shows all the CCFs stacked in one plot for the respective station pair, and each black trace represents the CCF for a day. The y- and x-axis represent the date of the CCF and the time lags where the CCF peak, respectively. The CCFs peak at about $\pm$10 s. All of the following CCF against time lag plots were generated with the 0.1-1 Hz filter.

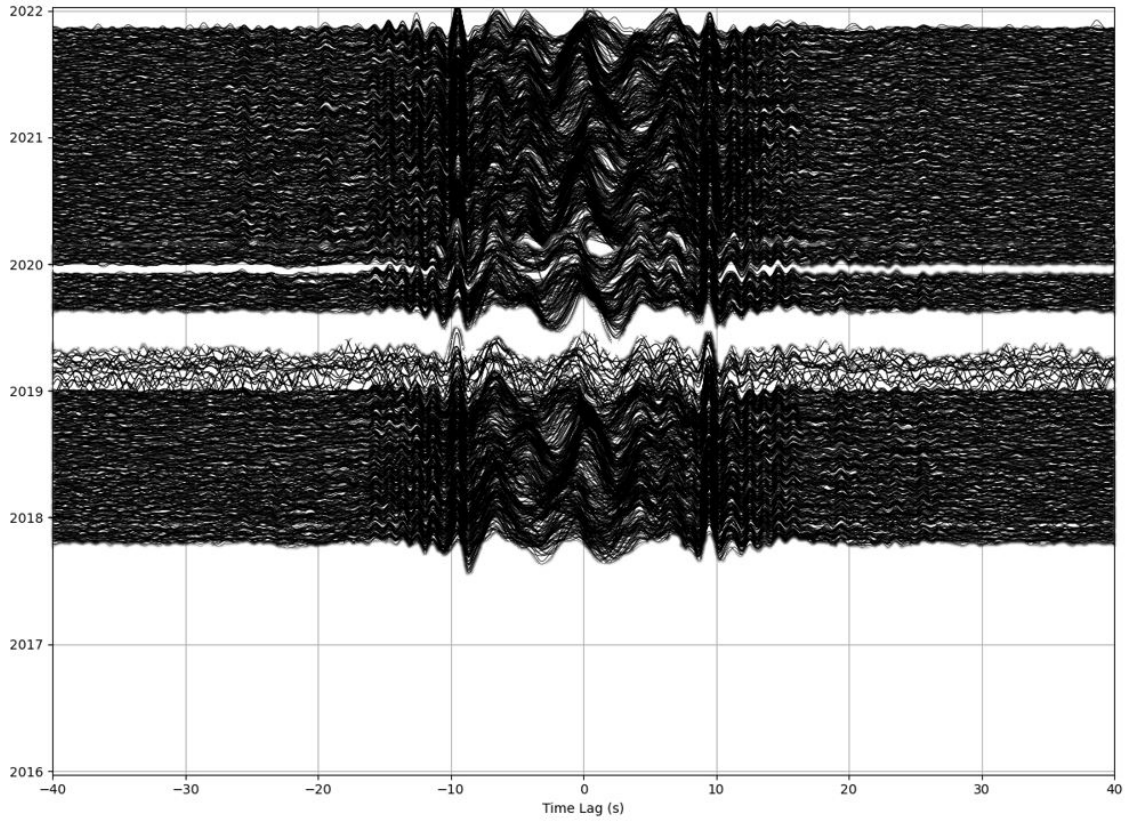

Figure 4.5.: CCF against time lag plot for the cross-correlation of two broadband stations. This plot shows all the CCFs stacked in one plot for the MSDA-CBH9 station pair. Each horizontal black line represents the CCF for a day. The y- and x-axis represent the date of the CCF and the time lags, respectively. The CCFs peak at about $\pm$10 s. This plot was generated with the 0.1-1 Hz filter.

Figure 4.6 shows more examples of CCF against time lag plots for different filters. The CCF against time lag plots are for the cross-correlation of: a broadband and short-period station (Figures 4.6a and b), and two short-period stations (Figures 4.6c and d). Figures 4.6a,c, and 4.6b,d were developed with the 0.1-1 Hz and 0.3-3 Hz filter respectively. The plot of each station pair has CCFs that peak at different time lags. These time lags are specific to the interstation distance of the station pair. A wider gap between the peaks of the time lags of the CCFs indicates a longer interstation distance. Although short period instruments are being used in Figures 4.6, the signal can still be clearly observed. The CCFs peak at about $\pm$12 s and $\pm$10 s respectively in Figures 4.6a and c. Peaks at 0 s in Figures 4.6a and c are probably caused by teleseismic earthquakes, and are completely removed from Figures 4.6b and d when applying the higher 0.3-3 Hz filter.

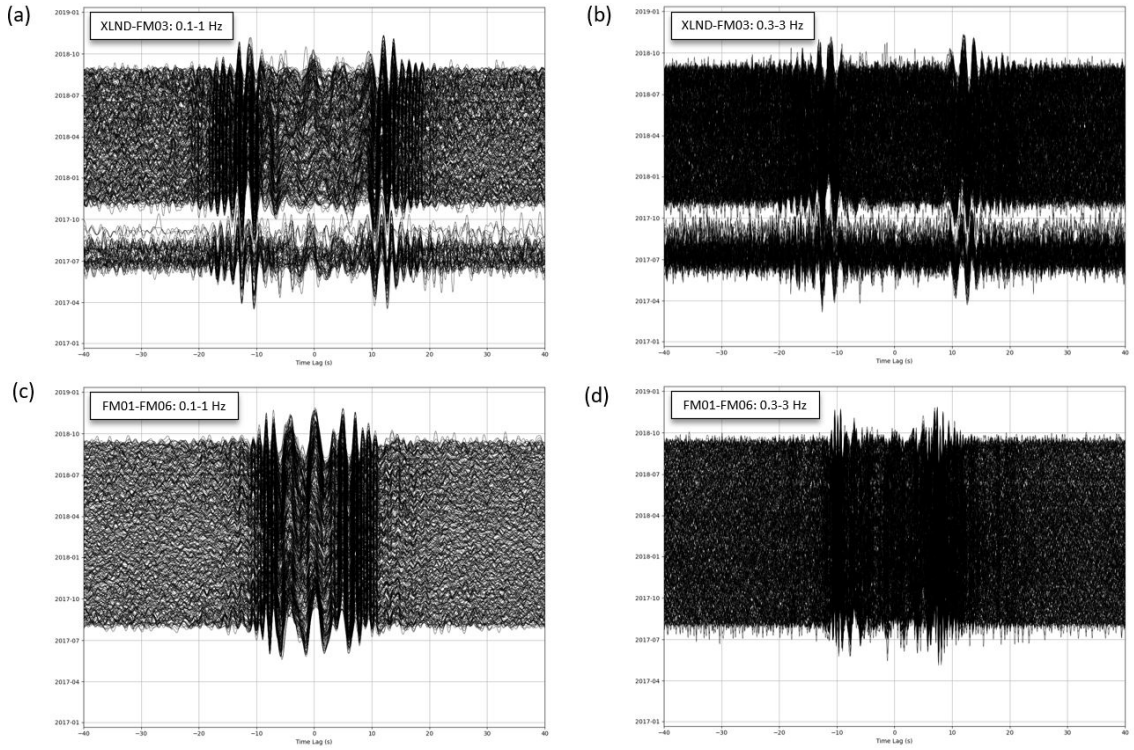

Figure 4.6.: CCF against time lag plot for the cross-correlations of broadband and short-period stations at different filters. The CCF against time lag plots are for the cross-correlation of: (a),(b) a broadband (XLND) and short-period station (FM03), and (c),(d) two short-period stations (FM01 and FM06). Figures (a),(c), and (b),(d) were developed with the 0.1-1 Hz and 0.3-3 Hz filter respectively. The CCFs peak at about (a) $\pm$12 s and (c) $\pm$10 s respectively.

Autocorrelations were also computed by correlating the noise recorded by a single station with itself (Gubbins, 2004). Figure 4.7 shows CCF against time lag plots for the autocorrelation of a broadband (MSDA) and short-period station (FM02) at filters 0.1-1 Hz and 0.3-3 Hz, respectively. In this case, the CCFs peak at 0 s since the cross-correlation type is an autocorrelation.

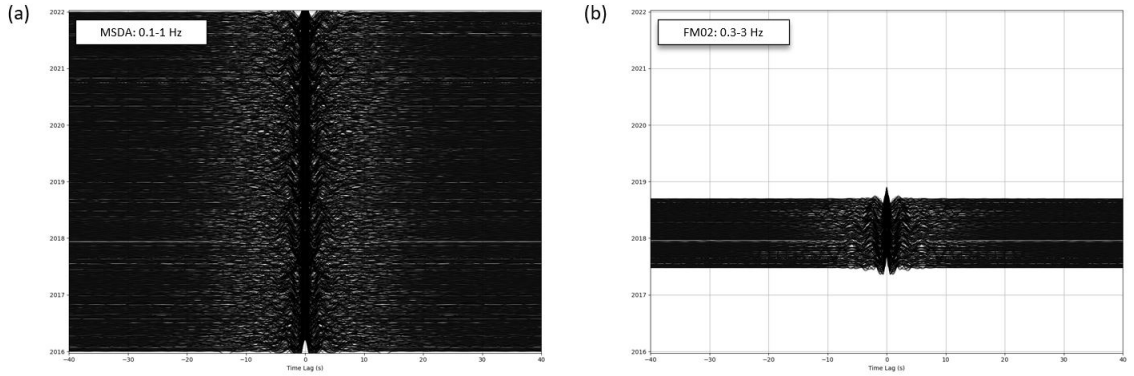

Figure 4.7.: CCF against time lag plots for the autocorrelation of broadband and short-period stations. The CCF against time lag plots are for the autocorrelation of: (a) a broadband station (MSDA), and (b) a short-period station (FM02). To generate these plots, the 0.1-1 Hz and 0.3-3 Hz filters were respectively used. See Figure 4.5 for more details on the CCF curves.

Figure 4.8 is an interferogram plot for the cross-correlation of two short-period stations. This plot is similar to the CCF against time plot (Figure 4.5), with the difference that the axes of the plots are inverted, and the amplitudes of the CCFs are represented in colour. Subtle seasonal changes can be seen visually in this plot.

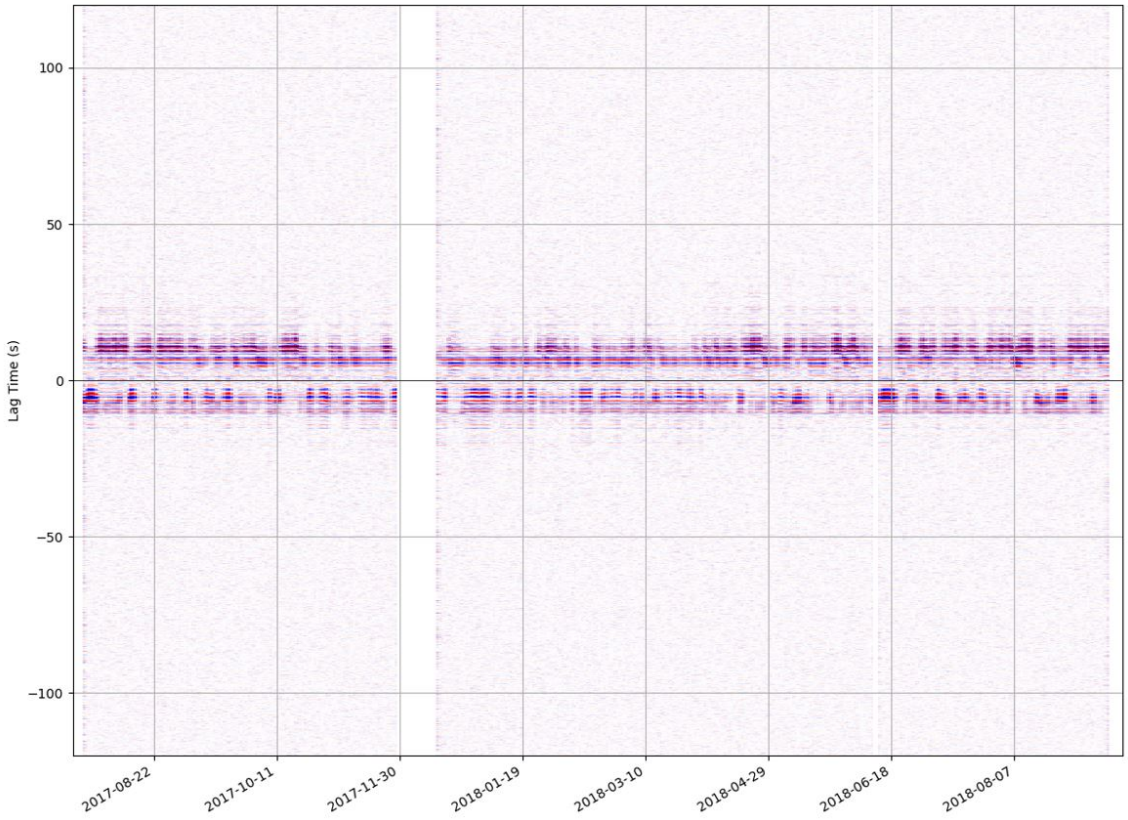

Figure 4.8.: Interferogram for the cross-correlation of two short-period stations (FM01 and FM05). The CCFs are shown as an image, with the different colours representing the amplitude of the CCFs.

4.5. Reference function

The reference function represents the stacking of the CCFs specified by the *ref_begin* and *ref_end*. To choose the reference function, Lecocq et al. (2014) proposes that all CCFs should be plotted and analysed for stable and consistent time spans, which could be defined as the reference. Taking the whole archive data as the reference involves the risk of diminishing the REF quality if very strong velocity variations are observed as a result of, for example, time errors at one of the stations (e.g., Duputel et al., 2009; Mordret et al., 2010). This was the case for station XLND, which experienced timing errors in its clock from 2019-08-01 onwards. When setting the reference end date to this date (*ref_end*), MSNoise failed to compute past this date on all the other stations because there was no reference available for that time period of the CCFs. Therefore, it was decided to use the

whole data archive as a reference, by setting *ref_begin* and *ref_end* to 2016-01-01 and 2022-01-01 respectively. This bug in the code is thought to have been solved in the latest version of MSNoise.

The interstation distance plots in Figure 4.9 shows all the reference cross- and auto-correlation functions for the vertical (Z) component for each different station pair. Of the three components recorded, the Z component recordings were utilised in this study. This was deemed sufficient to present the discussed technique as a proof of concept, since most Rayleigh waves can be picked up by the Z component of seismometers. These reference correlograms were obtained from the whole set of data. Each horizontal black line represents a reference cross- or auto correlation function for each station pair. The y-axis of this plot represents the interstation distance (km) of each station pair, and the x-axis represents the time lag (s). Each reference CCF peaks in the causal and acausal time lags. As the interstation distance increases, the time lag of the peaks of the reference CCF also increase. The red, green, and blue lines in the plot indicate the velocity of ballistic waves to be avoided. The reference correlation functions at an interstation distance of 0 km are for autocorrelations. It can be observed that the plot is symmetric suggesting that the ambient seismic noise received by the stations is isotropic, and that the ocean microseism noise sources are from random and equally distributed sources and directions. This is likely due to the fact that Malta is an island.

Figure 4.9 compares the reference CCFs from the 0.1-1 Hz filter and from the 0.3-3 Hz filter, both using the Z component. The two plots have similar CCFs, however, the higher filter seems to eliminate the peaks of the stacked CCFs at 0 s (in Figure 4.9a), which could be indicative of teleseismic earthquakes. Nonetheless this peak at 0 s does not affect the further processing.

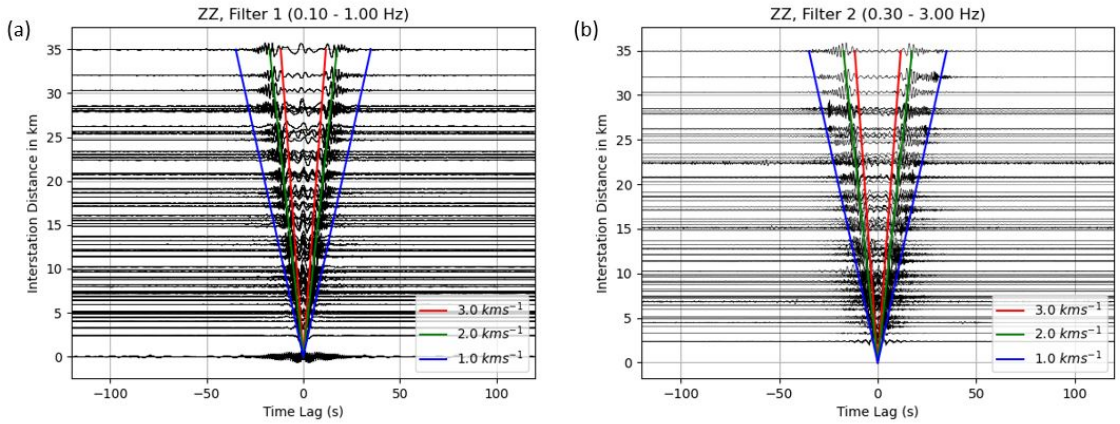

Figure 4.9.: Reference cross- and autocorrelation curves. Interstation distance (km) against time lag (s) plots for the vertical component (Z) for filter (a) 0.1–1.0 Hz, (b) 0.3-3 Hz. The red, green and blue lines indicate the velocity of ballistic waves. The correlation functions at an interstation distance of 0 km are from the autocorrelations. The symmetry of the plot indicates that noise received by the stations is isotropic.

4.6. Stacking

Ideally, a single CCF gives the expected theoretical Green's function. However, due to noise in the data, the CCFs are not always clearly observed. Thus, stacking is applied, whereby CCFs from numerous time windows are stacked together. The *stack_method* used was "Linear Mean", which saves the daily CCF as a simple mean CCF of all windows. The daily CCF stack consists of 96 CCFs from 30-minute time windows at a time step of 15 minutes. This may also not be sufficient, and a moving-window stack encompassing a number of days may be necessary to enhance the signal of the CCF.

When comparing the daily CCFs in different moving-window stacks with the reference, a correlation coefficient between the two can be determined (e.g., Lecocq et al., 2014). Signals can be different between the positive and negative time lags (e.g., Lecocq et al., 2014; Mordret et al., 2010), as can be observed in the interferogram plot (Figure 4.8). Changes in the correlation can be smooth, due to a change in the velocity, or dramatic, if there are changes in the origin of the seismic noise or in the position of some of the scatterers (Wegler and Sens-Schönfelder, 2007). As a result of noisy CCFs, comparing the CCFs to the reference can yield strong velocity variations between the two (Lecocq et al., 2014). While a long moving-window stack is recommended to reach a correlation coefficient of 0.96, a moving-window stack that is too long (e.g., 10 days) will drastically decrease the resolution of the CCF (Lecocq et al., 2014). Being able to control the moving-window stack length can help in both hiding or highlighting certain important features in the data (Liu et al., 2010). From the 1, 2, 5, and 10 day default stacking that was tested (*mov_stack* = 1,2,5,10), the 2 day stacking was chosen as the most reasonable, to maintain a high resolution. Figure 4.10 shows an example of the CCF against time plot for the MSDA-WDD cross-correlation for 2016 at a stacking of: (a) 1 day, (b) 2 days, (c) 5 days, and (d) 10 days. The higher the stacking, the smoother the CCFs and the clearer the peaks in the CCFs.

The reconstruction of stable, in time, CCFs determines the accuracy of the seismic velocity change measurements (Hadziioannou et al., 2009). To tackle this, utilising noise time series that are long enough ensure that an adequate coherence between an individual CCF and the reference of a certain threshold, is reached (Lecocq et al., 2014). While a greater coherence can be achieved when using longer noise time series, the time resolution is diminished (Lecocq et al., 2014).

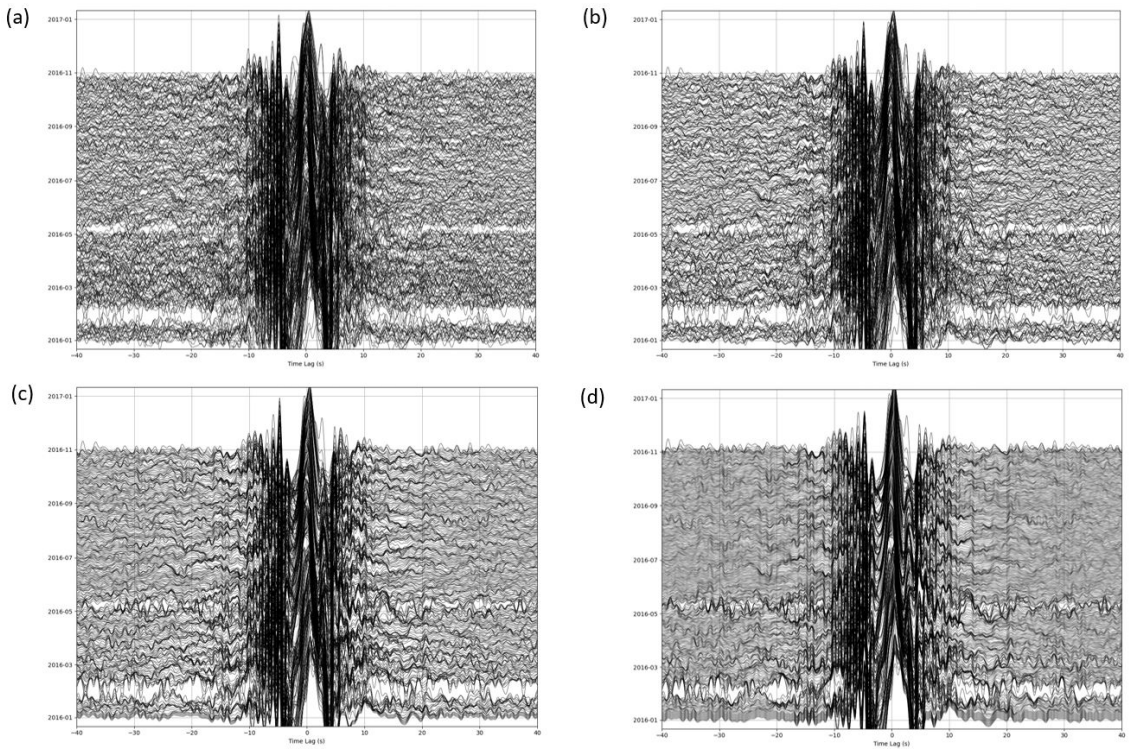

Figure 4.10.: CCF against time lag plots for the different stacking. The CCF against time lag plot for the MSDA-WDD cross-correlation from 2016 at a stacking of (a) 1 day, (b) 2 days, (c) 5 days, and (d) 10 days. See Figure 4.5 for more details on the stacked CCF curves.

4.7. Moving-Window Cross-Spectral technique

MSNoise incorporates the Moving-Window Cross-Spectral (MWCS) technique (Clarke et al., 2011) to calculate the time lag (δt) between the "current" CCF and the reference within a number of overlapping moving time-windows. Before calculating the difference between both time series, the "current" and reference CCFs were split into overlapping windows N_w and preprocessed. The N_w, window length and overlap were chosen according to the signal-to-noise ratio and frequency content of the *current* CCF. Once the moving time-windows were mean-adjusted and cosine-tapered, the windows were transformed into the frequency domain from the time domain using the Fourier transform.

Adapted from Clarke et al. (2011), Figure 4.11 illustrates the process of how -$\delta t/t$ is calculated using the MWCS technique. Figure 4.11a shows two CCFs plotted on top of eachother, where the red and black line represent a "current" CCF and a reference CCF for a time interval from -30 to 30 s. The difference between the two lines in the plot is not visible to the reader, since the CCFs are similar and the difference between both CCFs is very small. The black box represents the moving time window, for which δt is calculated. For the first filtering band of 0.1-1 Hz, the window length *mwcs_wlen* and overlap length *mwcs_step* to perform MWCS were set to 12 s and 4 s, respectively. These parameters were chosen since a window of width 12 s would encompass one full wavelength (which is

at most 10 s for the 0.1-1 Hz filter) and each time window would be sampled three times in total (since three 4 s steps fit in a 12 s window). The same reasoning was followed for the 0.3-3 Hz filter of the short period stations, where the window length *mwcs_wlen* and overlap length *mwcs_step* to perform MWCS were set to 6 s and 2 s respectively.

Equation 4.5 shows the cross-spectrum ($X(v)$) between both windowed time-series in Figure 4.11a:

$$X(v) = F_{ref}(v) \cdot F^{*}_{cur}(v) \tag{4.5}$$

where $F_{ref}(v)$ and $F^{*}_{cur}(v)$ are the Fourier transformed windowed current and reference time series, * represents the complex conjugation and v is the frequency in Hz. Equation 4.5 can be translated into Equation 4.6 since it is more useful for the complex cross-spectrum to be represented in terms of its amplitude ($\mid X(v) \mid$) and phase ($\phi(v)$):

$$X(v) = \mid X(v) \mid e^{i\phi(v)} \tag{4.6}$$

Then, the cross-coherence between energy densities $C(v)$ (Equation 4.7) in the frequency domain are used to quantify the similarity between both CCFs, since both windowed CCFs are assumed to be similar:

$$C(v) = \frac{\overline{\mid X(v) \mid}}{\sqrt{\overline{\mid F_{ref}(v) \mid}^{2} \cdot \overline{\mid F_{cur}(v) \mid}^{2}}} \tag{4.7}$$

The overlines in the equation represents the applied smoothing, that consists of a sliding raised-cosine function with a half-width of 0.1 Hz to the energy density spectra of the two windowed Fourier- transformed time-series and to the real and imaginary parts of the complex-valued cross-spectrum. The cross-coherence values range from zero to one, with one being the maximum value of cross-coherency that can be reached between the two spectral densities (see Figure 4.13b).

The time lag between each "current" and reference CCF is proportional to frequency, and is found in the unwrapped phase ($\phi(v)$) of the cross spectrum, as shown in Equations 4.8 and 4.9:

$$\phi_j = m \cdot v_j \tag{4.8}$$

$$m = 2\pi\delta t \tag{4.9}$$

The lower *mwcs_low* and upper *mwcs_high* frequency bounds of the linear regression were set to the lower and upper frequency bounds of each filter, respectively. For every time window, the small difference (δt_i, where i represents the ith window) between

the current and reference CCF is calculated and plotted in Figure 4.11b, as the black dots. Figure 4.11b is a graph of delay times (y-axis) vs time lags (x-axis), where the red line is the fitted slope for the set of black points. The slope of this line (m), which is equal to $-\delta t/t$, is calculated as a weighted linear regression (WLS). The output of the MWCS technique in MSNoise is a text file containing the central time lag, the delay times measured at each time window ($-\delta t/t$), the error and mean coherence of the segment.

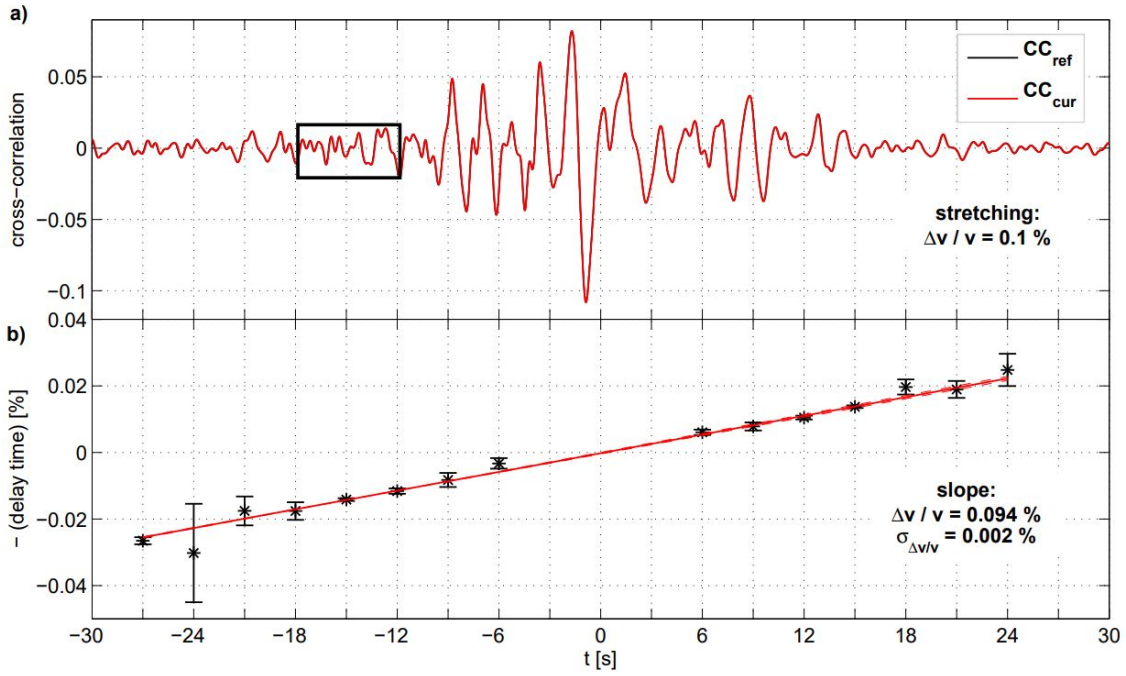

Figure 4.11.: The Moving-Window Cross-Spectral (MWCS) technique as illustrated by Clarke et al. (2011). (a) The red and black lines are the current CCF and the reference CCF respectively, along the time interval of -30 to 30 s. The difference between the two lines in the plot is not visible to the reader, since the CCFs are similar and the difference between both CCFs is very small. The black box represents the moving time window for which δt is calculated. In this plot, the moving time window is 6 s, and with a 3 s drift. (b) The black points represent each δt calculation for every moving time window, and the red line is the fitted slope for those set of points. The slope of this line is equal to $-\delta t/t$.

Figure 4.12 shows an example of a $\delta t/t$ plot generated by MSNoise for the cross-correlation of XLND-CBH9 for the day 2018-08-01. This plot is the same type of plot as Figure 4.11b. The blue dots are calculated from the small difference between the "current" and reference CCF in every moving time window, and the black line (M) is the slope calculated from a weighted linear regression. The slope of this line (M) is the $-\delta t/t$. The red line ($M0$) is the same as M, but $M0$ has no offset to have no y-intercept. Both M and $M0$ were tested in the $\delta v/v$ computations, but there was a negligible difference between the two. Therefore, it was decided that M was to be used (Lecocq, personal communication). The purple band in the plot is specific to the interstation distance of the station pair being considered and help with selecting the points for the WLS. The blue dots within the purple band are expected to be the most stable that follow a linear trend.

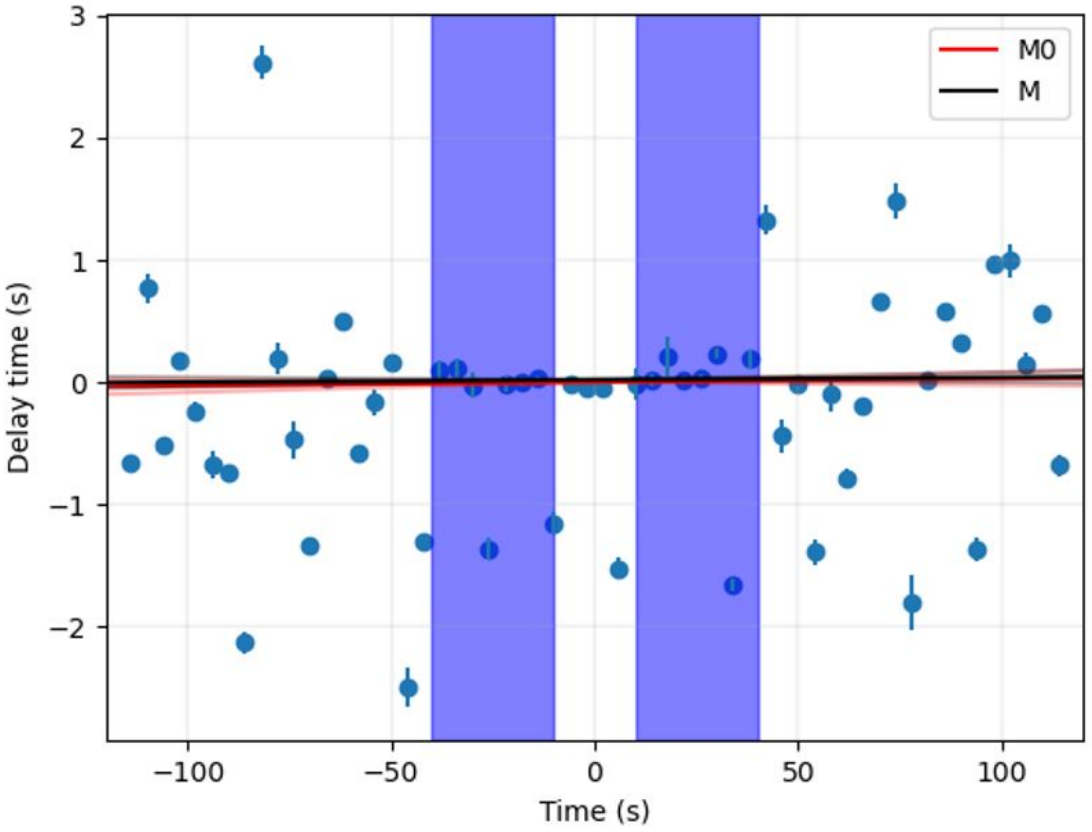

Figure 4.12.: Example of a delay time against time lag plot of the cross-correlation of XLND-CBH9 for the day 2018-08-01. The blue dots are calculated from the small difference between the "current" and reference CCF in every moving time window. The black line is the slope (M) calculated by a weighted linear regression (WLS) through points within the purple band. The red line is the fit with no intercept ($M0$). The slope represents the $-\delta t/t$ value. The blue dots within the purple band are expected to be the most stable that follow a linear trend.

A zoom-in on the "current" and reference CCFs in the respective time window shown in Figure 4.11a can be observed in Figure 4.13a. As previously mentioned, the cross-coherence values range from zero to one, with one being the maximum value of cross-coherency that can be reached between the two spectral densities (Figure 4.13b). The *min_coh* parameter in MSNoise was set to 0.65, which means that MWCS points below this value were skipped and not used in the following weighted linear regression. A minimum coherence that is too high may lead to a loss of data points. Contrastingly, a coherence value that is too low would lead to a higher degree of noise in the processing of the data. 0.65 was decided to be an adequate value for the minimum coherence (Lecocq, personal communication). This minimum coherence could have been set to a different value for the different networks available, but this was not within the scope of the study. Between the two windowed time series in Figure 4.13a, a linear regression for the phase displacement is completed at the frequency ranges of 0.1-1 Hz and 0.3-3 Hz that were used in this study.

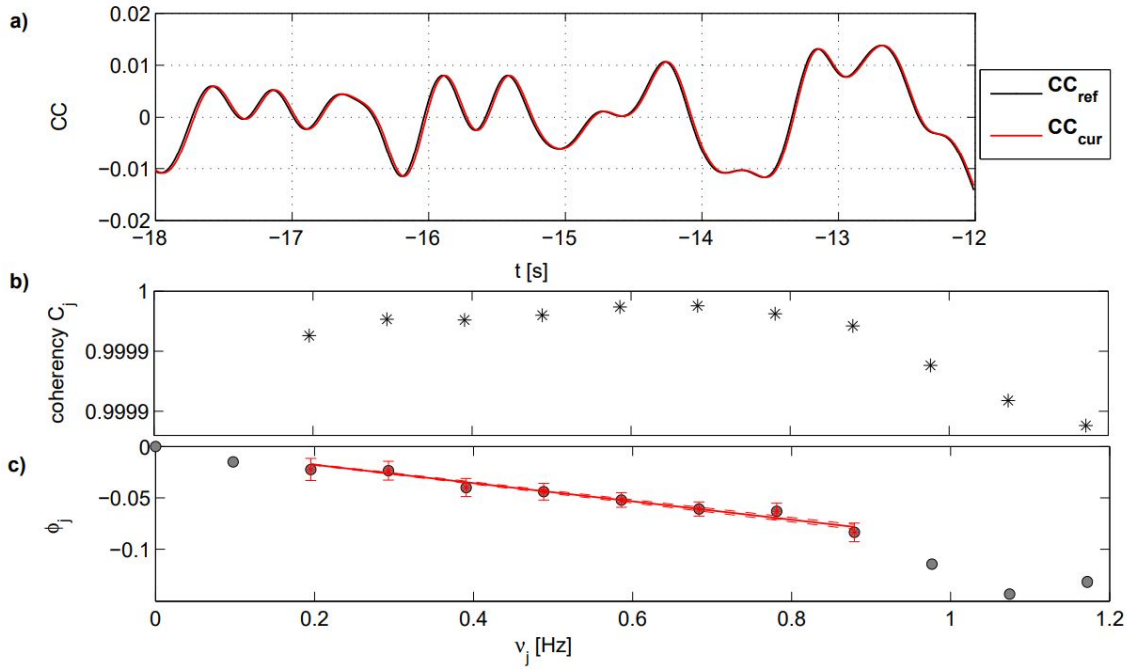

Figure 4.13.: Example of how a delay-time between two windowed cross-correlations is measured. A plot by Clarke et al. (2011) that shows: a) a zoom-in on the "current" and reference CCFs in the respective time window shown in Figure 4.11a and b) the calculation of coherency between two windowed time-series at all frequencies, and c) Linear regression for the phase displacement between the two windowed time-series at a frequency of interest.

Figures 4.14 and 4.15 show MWCS plots from MSNoise for the cross-correlation of a broadband and short-period station, and the autocorrelation of a short-period station respectively. The horizontal green lines in all four subplots indicated the selected time lags for the $\delta t/t$ calculation, specific to the interstation distance of the respective station pair being considered. The vertical red dotted lines indicate the maximum δt (top right) set at ± 0.1 s and the minimum coherence (bottom right) set at 0.65. The figure in the top left of Figure 4.14 shows the horizontally stacked δt against time lag plot of different days for the cross-correlation of MSDA-FM01. The separated red and blue bands lines in the δt plot are evident, and these colour bands are representative of the positive and negative time lags ($\pm\ \delta t$). The figure in the top right shows the mean and standard deviation of the time lag for the respective δt plot (left).

The bottom left plot shows the horizontally stacked coherence against time lag plot of different days. From the mean coherence plot in both figures, a high mean coherence between the "current" and reference CCF curves is noticed from the whiter horizontal band at around 0 s lag time between the green horizontal lines. If the mean coherence was low, then a darker orange band would be expected at 0 s lag time. The figure in the bottom right shows the mean and standard deviation of the mean coherence for the respective mean coherence plot (left). Some data points were omitted from the MWCS calculation since they did not satisfy the 0.65 minimum coherency criteria (Figure 4.15). The advantage of such MWCS plots are that they show all the data for a specific station pair in one plot.

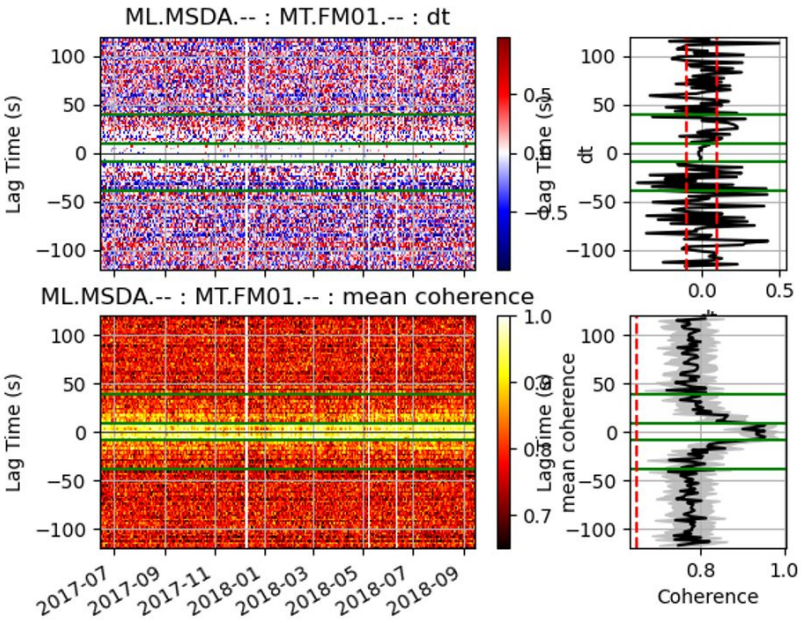

Figure 4.14.: MWCS analysis plot for a cross-correlation of broadband stations. Top left: Horizontally stacked δt vs time lag of different days. The blue/red colours represent the $\pm$ δt, respectively. Top right: The mean and standard deviation of the time lag for the whole image (left). Bottom left: Horizontally stacked coherence vs time lag of different days. The red/white shade represent the mean coherence. Bottom right: The mean and standard deviation of the mean coherence for the whole image (left). The horizontal green lines in all 4 subplots indicate the data points used for processing. The green lines are automatically determined depending on the interstation distance of the MSDA-FM01 station pair. The vertical red dotted lines indicate the maximum δt (top right) set at $\pm$0.1 s and the minimum coherence (bottom right) set at 0.65.

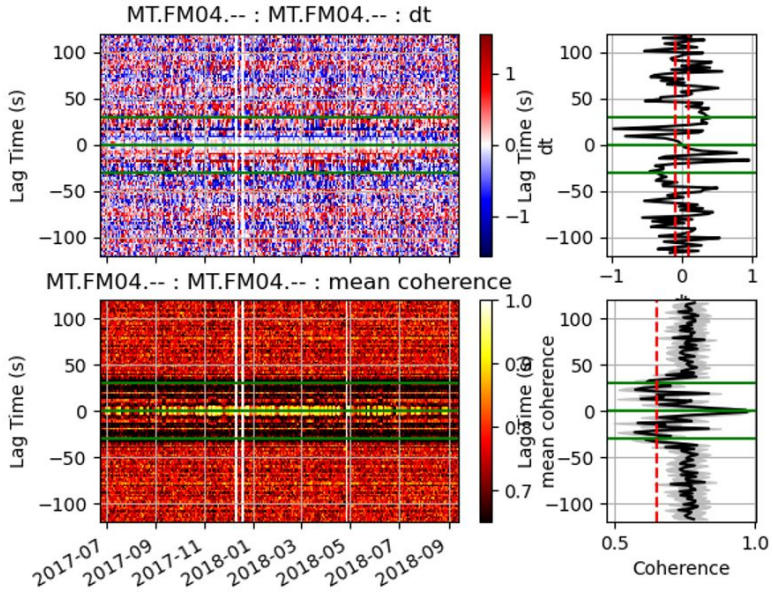

Figure 4.15.: MWCS plot for an autocorrelation of a short-period station. See Figure 4.14 for plot details.

4.8. Plotting the changes in seismic velocity

The final step of the MSNoise workflow is to compute and plot the velocity variations. Assuming that the seismic velocity change within the region is homogeneous, stretching in the $-\delta t/t$ of the "current" CCF relative to the reference is observed. This stretching is constant over t and is numerically opposite the seismic velocity change (Poupinet et al., 1984), as shown in Equation 4.10:

$$\frac{\delta v}{v} = \frac{-\delta t}{t} \tag{4.10}$$

In order to compute the time shift computations, the essential task of choosing adequate minimum and maximum lag times can be done either absolutely or dynamically. When *dtt_lag* is set to *dynamic*, the minimum time lag is determined by the interstation distance of each used station pair and the velocity of the ballistic waves to be avoided (*dtt_v*) (see Figure 4.9). The *dtt_lag* was set to *dynamic*, and *dtt_v* was set to 1.0 km/s. This set velocity allowed to avoid ballistic waves of a velocity greater than 1.0 km/s. If for example the interstation distance for a station pair is 10 km, the minimum time lag with this set velocity would be 10 s. Once the minimum time lag is determined, the width of the time lag window (*dtt_width*) was set to 30.0 s. This means that time lags from 10.0 to 40.0 s will be used in the current example, on both the causal and acuasal sides of the CCF (*dtt_sides* = both).

Figure 4.16 shows a quick $\delta v/v$ plot generated by MSNoise, for a cross-correlation of two broadband stations. The different frames each represent the 1, 2, 5, and 10 days of stacking that were considered. The blue lines in the plot represent the $\delta v/v$ of station pair XLND-WDD, and the orange and green lines signify the mean and median respectively. Although MSNoise provides this tool to quick view the seismic velocity changes at different stacking, custom python code was instead written to visualise the $\delta v/v$ against water level results for this study.

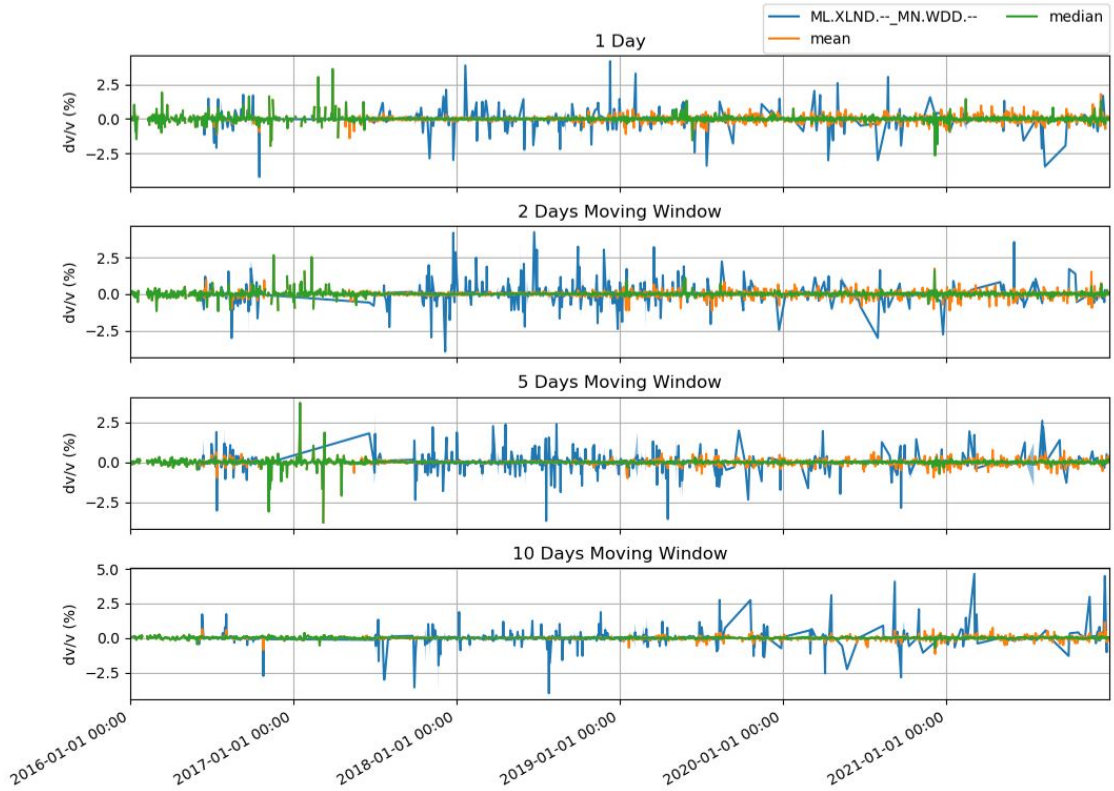

Figure 4.16.: $\delta v/v$ against time plot for the cross-correlation of two broadband stations. This plot has been generated by MSNoise The different frames represent the 1, 2, 5, and 10 days of stacking that were considered. The blue lines in the plot represent the $\delta v/v$ of station pair XLND-WDD, and the orange and green lines signify the mean and median respectively.

5. Results

Time-dependent seismic velocity changes from cross- and autocorrelations of ambient seismic noise from the MSN and the FASMIT seismic network in Malta will be presented in this chapter. The velocity changes show seasonal summer-winter variations, with patterns similar to the water level data from nearby boreholes. In total, 66 cross-correlation and 12 autocorrelation station pairs were generated. A selected number of these results of different auto- and cross-correlation plots from different combinations of broadband and short-period stations, and at different interstation distances, will be shown. A 30-, 60-, and 90-day moving average was also tested on the $\delta v/v$ and borehole data to smoothen out anomalies that are hard to explain. A 30-day rolling average was eventually selected, so as to give the best detail on a monthly scale (see Appendix B).

5.1. Cross-correlations

The results illustrated in the following figures show the $\delta v/v$ (%, primary y-axis) in red against water level (m, secondary y-axis) in blue. The axis of the $\delta v/v$ is inverted to help visualise the relationship between the change in seismic velocity and the changes in water level from nearby boreholes. As water level increases, the change in $\delta v/v$ is expected to be a negative one due to an increase in pore pressure in the grains of underground rocks. Each red scatter point represents a one-day measure for the $\delta v/v$ following a 2-day CCF stacking, and each blue scatter point is from a 30-minute measurement for the water level data. A 30-day rolling average was applied on all the scatter points respectively. The intervals in the x-axis mark the first day of the respective month or year. The light blue shading in the background of the plot indicates the autumn and winter months from September 21st to March 21st. These months are typically the rainiest in Malta.

Figure 5.1 is an example of $\delta v/v$ from the cross-correlation between a broadband (MSDA) and short-period (FM05) station versus the water level above MSL from a nearby borehole 10035 (Buqana). The CCFs in this plot were filtered at 0.3-3 Hz. The $\delta v/v$ varies over a range of $\sim$0.125%. Unfortunately, since only one year of data is available for the short period stations, annual variations in cross-correlations of short-period stations cannot be studied. However, a seasonal variation in the $\delta v/v$ can still be noted. An increase in water level at the end of the winter season (between 2018-03 and 2018-04) causes a negative change in the $\delta v/v$. Decreases in the water level, such as in the summer of 2017 and 2018 have caused a positive change in the $\delta v/v$.

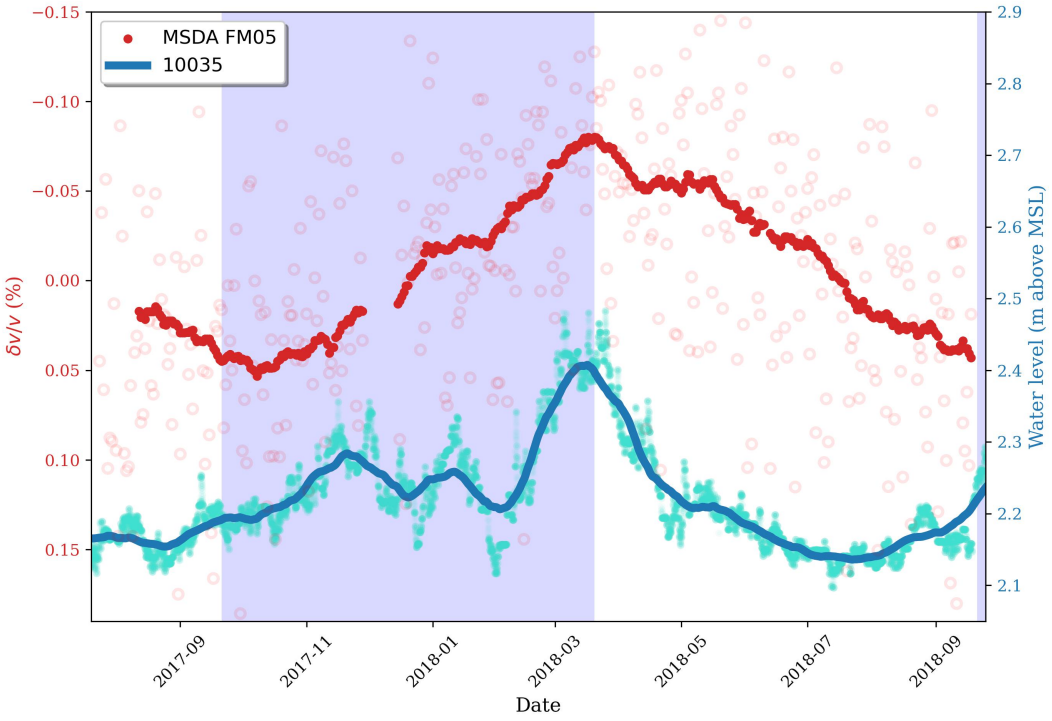

Figure 5.1.: Plot showing changes in seismic velocity ($\delta v/v$) for station pair MSDA-FM05 and water level data. The red and blue curves represent a 30-day rolling average of the $\delta v/v$ (%) and of the water level (m above MSL) from a nearby borehole 10035 (Buqana), respectively. Each red scatter point represents a one-day measure for the $\delta v/v$ following a 2-day CCF stacking, and each blue scatter point is from a 30-minute measurement for the water level data. The intervals in the x-axis mark the first day of the respective month. The light blue shading in the background indicates the winter months, generally the rainiest months in Malta (21st September to 21st March).

More examples of $\delta v/v$ of other cross-correlations of broadband with short-period stations (e.g., MSDA-FM02, MSDA-FM06, MELT-FM06, WDD-FM05, QALA-FM04, and WDD-FM06) against nearby water level borehole data are shown in Figure 5.2. The CCFs in these plots were filtered at 0.3-3 Hz. The $\delta v/v$ varies in the order of $\sim\pm0.05\%$, and seasonal variations in the $\delta v/v$ can be observed in all the plots with a peak generally towards the end of the winter season. All examples show similar general trends, where increases in water level in the winter period coincide with a negative change in the $\delta v/v$, while lower water levels in the summer months coincide with a positive change in the $\delta v/v$. This gives confidence in the data processing, particularly for the FASTMIT stations which only had a one-year recording. Note that, not all peaks in the $\delta v/v$ correspond with peaks in the water level data (e.g., at 2018-06 in Figure 5.2f).

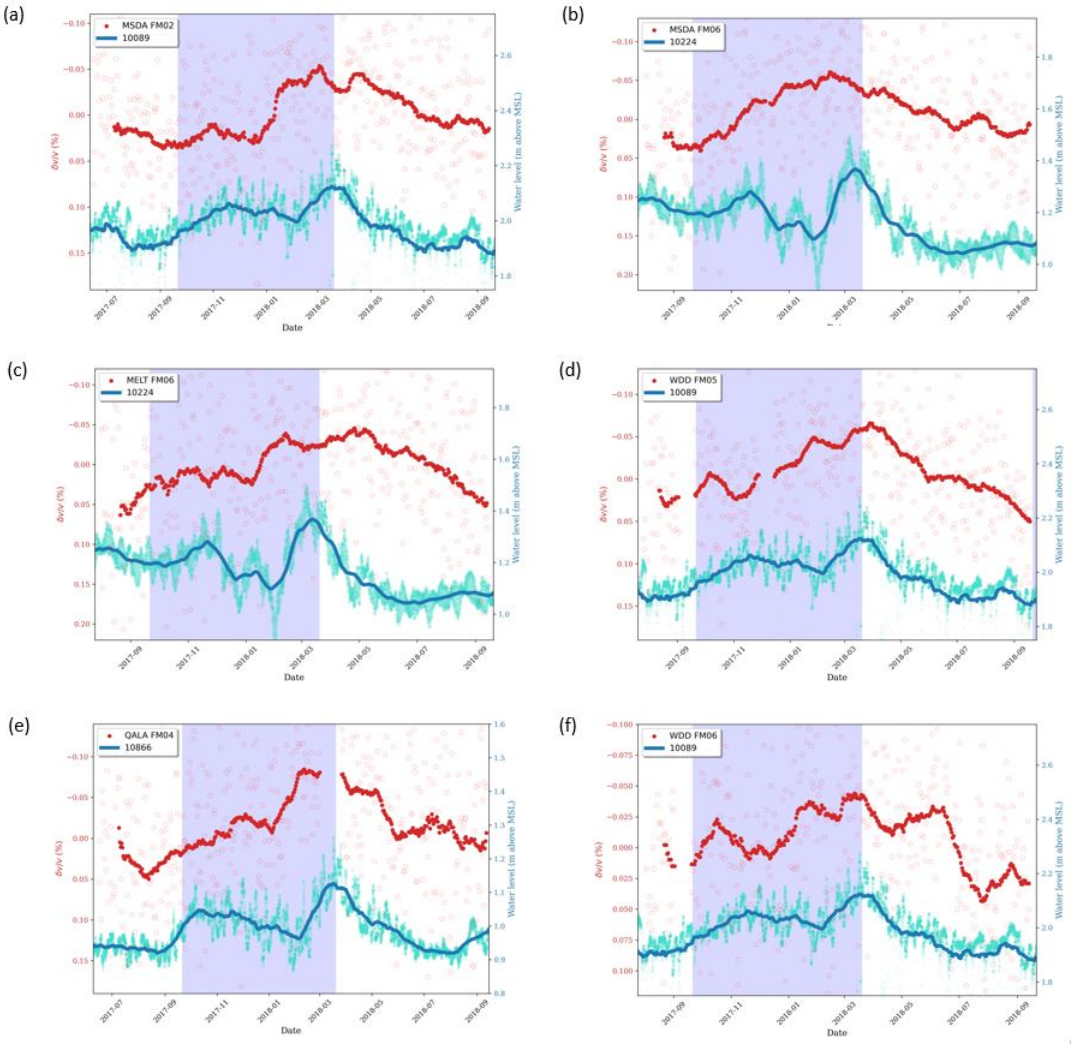

Figure 5.2.: Plots showing changes in seismic velocity ($\delta v/v$) from the cross-correlation of other broadband and short-period station pairs and water level data from nearby boreholes: (a) MSDA-FM02 (borehole 10089, L-Gharbi), (b) MSDA-FM06 (borehole 10224, Mdwara 1), (c) MELT-FM06 (borehole 10224, Mdawra 1), (d) WDD-FM05 (borehole 10089, L-Gharbi), (e) QALA-FM04 (borehole 10866, Republic Street, Gozo), (f) WDD-FM06 (borehole 10089, L-Gharbi). See Figure 5.1 for details on the plots.

Seasonal changes were also noted in the $\delta v/v$ from the cross-correlation of short-period station pairs. The $\delta v/v$ against water level plots of FM01-FM05, FM01-FM02, FM02-FM05, FM02-FM06, FM04-FM06, and FM05-FM06 are shown in Figure 5.3. The CCFs in these plots were all filtered at 0.3-3 Hz. The $\delta v/v$ varies in the order of $\sim\pm 0.05\%$ in all the plots. Very good agreement of certain peaks in the borehole levels with peaks in the $\delta v/v$ can be observed (e.g., in Figures 5.3b and e).

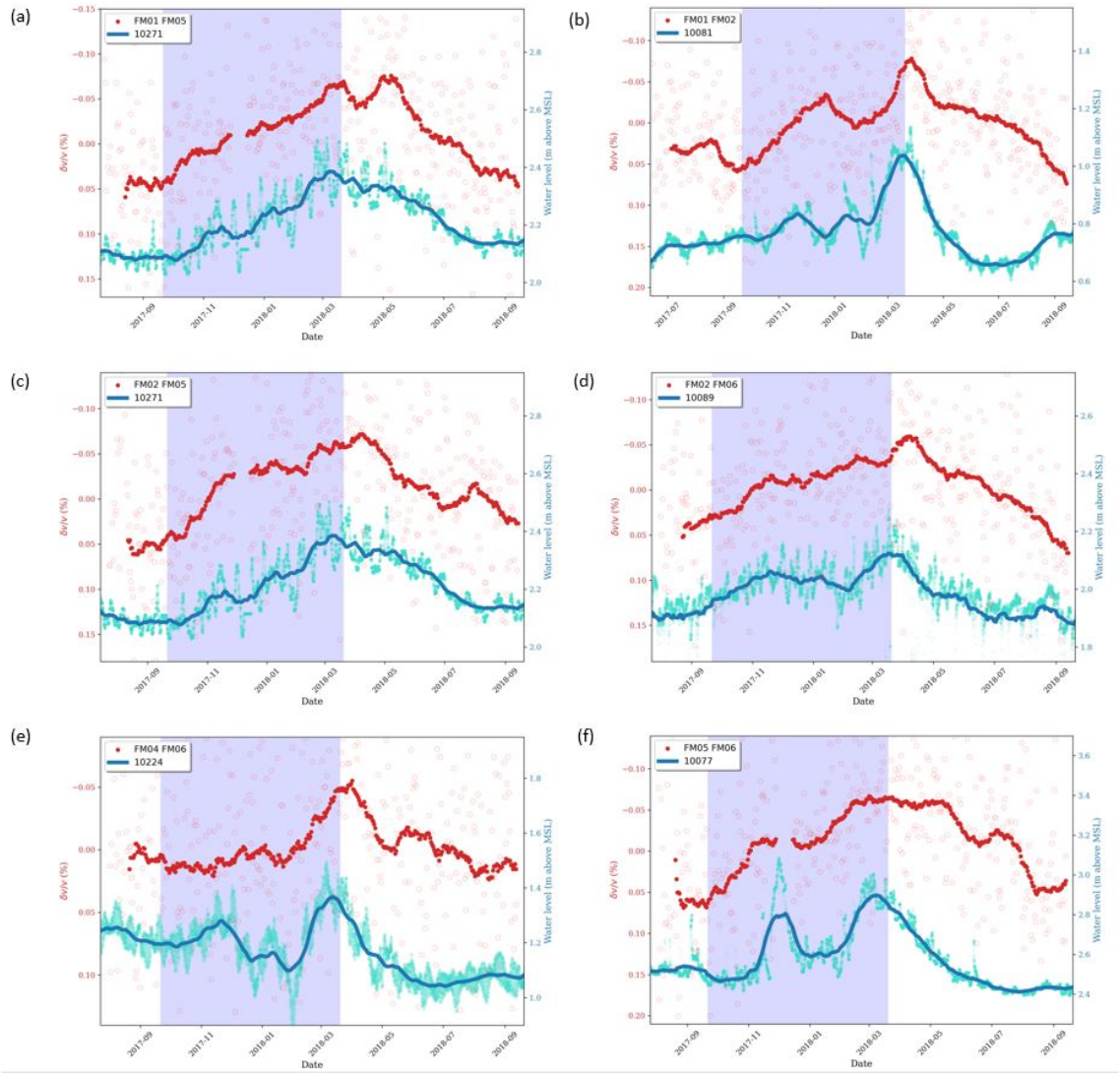

Figure 5.3.: Plots showing changes in seismic velocity ($\delta v/v$) from the cross-correlation of short-period station pairs and water level data from nearby boreholes: (a) FM01-FM05 (borehole 10271, Buskett), (b) FM01-FM02 (borehole 10081, Kandja), (c) FM02-FM05 (borehole 10271, Buskett), (d) FM02-FM06 (borehole 10089, L-Gharbi), (e) FM04-FM06 (borehole 10224, Mdawra 1), and (f) FM05-FM06 (borehole 10077, Wied il-Qliegha). See Figure 5.1 for details on the plots.

The cross-correlations between broadband stations did not turn out as good as one would have expected. The $\delta v/v$ against water level plots of CBH9-XLND, CBH9-QALA, CBH9-MELT, and MELT-QALA are shown in Figure 5.4. The CCFs in these plots were filtered at 0.1-1 Hz. The $\delta v/v$ has a maximum variation of $\sim$0.3%. Unfortunately, some of these stations (XLND, QALA, and MELT) had technical problems during various periods of 2019-2021 which hindered the processing. The effect of these problems are discussed in the next chapter. Seasonal variations in the $\delta v/v$ can still be observed to a certain extent in Figure 5.4b, and till the end of 2018 in Figures 5.4a and c. Data gaps in the $\delta v/v$ are evident in all figures, and an explanation of the cause of these gaps can be found in Section 6.1.

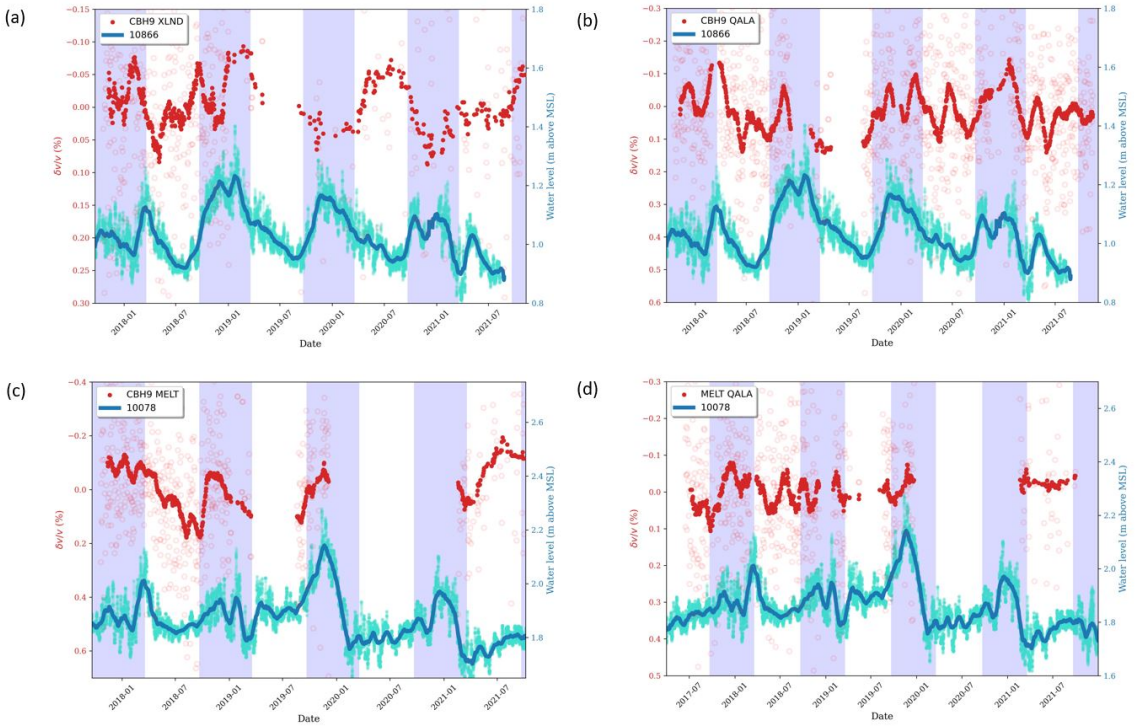

Figure 5.4.: Plots showing changes in seismic velocity ($\delta v/v$) from the cross-correlation of broadband station pairs and water level data from nearby boreholes: (a) CBH9-XLND (borehole 10866, Republic Street, Gozo), (b) CBH9-QALA (borehole 10866, Republic Street, Gozo), (c) CBH9-MELT (borehole 10078, Gomerino), and (d) MELT-QALA (borehole 10078, Gomerino). See Figure 5.1 for details on the plots.

5.2. Autocorrelations

Similarly, annual and seasonal variations can be observed in the $\delta v/v$ from autocorrelation functions. Figure 5.5 shows plots of $\delta v/v$ derived from autocorrelations of broadband stations MSDA, WDD, XLND, CBH9, MELT, and QALA against water level plots from nearby boreholes. The $\delta v/v$ has a maximum variation of $\sim$1% in all the plots. The CCFs in these plots were filtered at 0.1-1 Hz. Annual and seasonal variations in $\delta v/v$ are very

clear in Figures 5.5a-c, and till the end of 2018 in Figures 5.5 and e. Some data gaps and sudden changes in the $\delta v/v$ are evident in Figures 5.5d and f, and these will be discussed in Section 6.1.

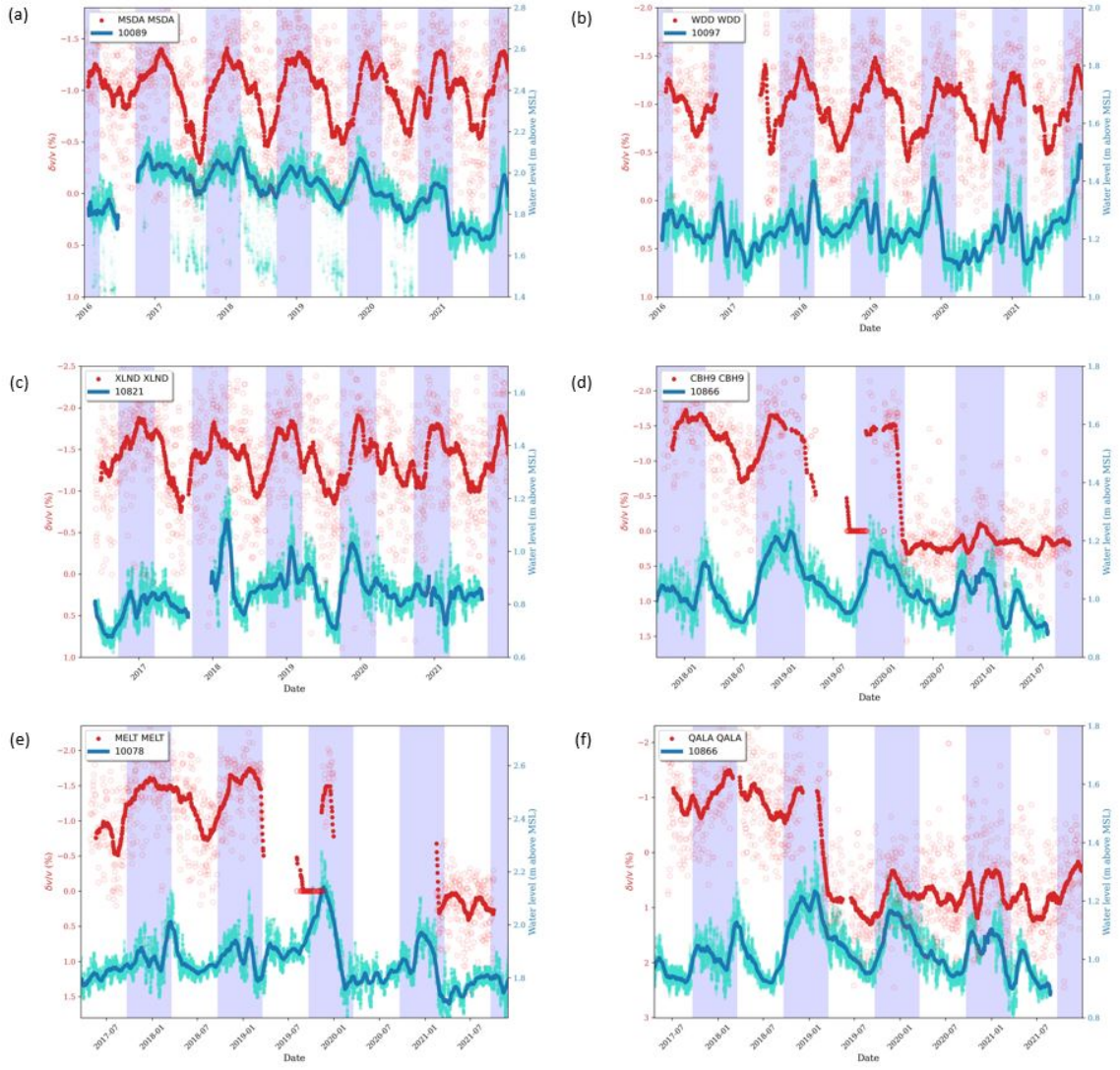

Figure 5.5.: Plots showing changes in seismic velocity ($\delta v/v$) from the autocorrelation of broadband stations and water level data from nearby boreholes: (a) MSDA (borehole 10089, L-Gharbi), (b) WDD (borehole 10097, Karwija 1), (c) XLND (borehole 10821, Wied Sara), (d) CBH9 (borehole 10866, Republic Street, Gozo), (e) MELT (borehole 10078, Gomerino), and (f) QALA (borehole 10866, Republic Street, Gozo). See Figure 5.1 for details on the plots.

Seasonal variations are also noted in most of the $\delta v/v$ from short-period autocorrelations. Figure 5.6 shows plots of $\delta v/v$ for autocorrelations of short-period stations FM01, FM02, FM03, FM04, FM05, and FM06 against water level data from nearby boreholes. The CCFs in these plots were filtered at 0.3-3 Hz. The $\delta v/v$ has a maximum variation of $\sim$2% in Figures 5.6b and d. The remaining plots exhibit a maximum variation of $\sim$0.5%. The $\delta v/v$ and water level peaks do not always coincide as they do in, for example, Figure 5.3. Still, the peaks in the $\delta v/v$ coincide with peaks in the water level at certain points, such as at 2018-03 in Figure 5.6c.

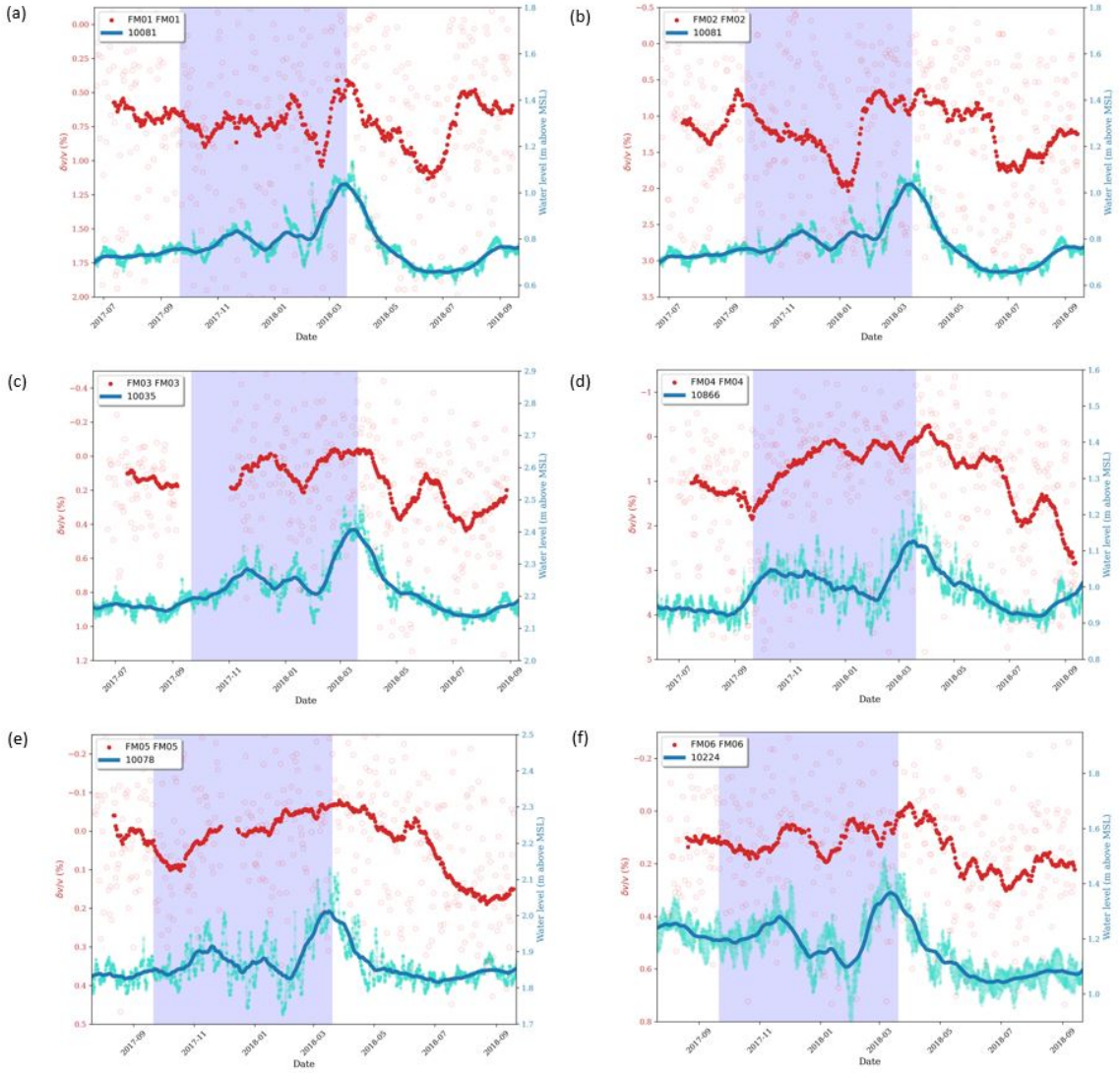

Figure 5.6.: Plots showing changes in seismic velocity ($\delta v/v$) from the autocorrelation of short-period stations and water level data from nearby boreholes: (a) FM01 (borehole 10081, Kandja), (b) FM02 (borehole 10081, Kandja), (c) FM03 (borehole 10035, Buqana), (d) FM04 (borehole 10866, Republic Street, Gozo), (e) FM05 (borehole 10078, Gomerino), and (f) FM06 (borehole 10224, Mdawra 1). See Figure 5.1 for details on the plots.

6. Discussion

The results demonstrate that seasonal and annual changes in the groundwater levels can be detected by changes in seismic velocity ($\delta v/v$) for small islands such as Malta. This is important as most studies that have detected seasonal changes in the $\delta v/v$ so far have been from large groundwater basins (Clements and Denolle, 2018; Kim and Lekic, 2019; Mao et al., 2022), complex aquifer systems (Lecocq et al., 2017), volcanoes (Sens-Schönfelder and Wegler, 2006, 2011), mountain regions (Illien et al., 2021), geothermal fields (Sánchez-Pastor et al., 2019), groundwater exploitation fields (Garambois et al., 2019; Voisin et al., 2017), larger islands (Wang et al., 2017), and volcanic islands (Grobbe et al., 2021). Malta has relatively smaller aquifer systems, it is surrounded by saltwater at close distances, and it has no rivers, lakes, or mountain regions.

The methods work for both cross- and autocorrelation functions of ambient seismic noise, the latter being an order of magnitude more sensitive. Two types of stations were investigated: broadband from the MSN and short-period from the FASTMIT network, and show that both stations can provide similar sensitivity to the $\delta v/v$ when taking into consideration appropriate filters.

The agreement between the temporal variation of $\delta v/v$ and the borehole water level is not always consistent. In some cases, the $\delta v/v$ follows the water level very closely, while in other cases, the agreement is poor. This could be due to the fact that the borehole was distant from the region being sampled, and perhaps in a different geological setting, or that changes in water content were highly localised near the borehole. The water level sensors are also known to undergo periods of unreliability. One should also take into consideration the changes in geology of the Maltese islands, characterised by normal faults, which may also have an effect on the dynamics of the changes in seismic velocity and groundwater level.

It could also be that water level changes are not the sole reason that the $\delta v/v$ varies seasonally, and other geophysical considerations such as from meteorological phenomena may play a role as discussed in Section 6.6. For these reasons, finding a statistical correlation between the changes in seismic velocity and the water level data may not be useful. Nevertheless, the clear seasonal variation of our results gives us confidence that $\delta v/v$ may conceptually act as a suitable proxy for monitoring groundwater levels in the Maltese islands in regions where borehole measurements are sparse. In this chapter, some further issues related to the performance of the method are discussed, as well as the comparison of the $\delta v/v$ with the nearest borehole water level, with interstation distance, rainfall, seasonal air temperatures, and atmospheric pressure.

6.1. Station problems: Timing issues, power outage, station reconfiguration

Before interpreting the results of this study, it is important to first identify any errors in the performance of the seismic stations throughout the study period. Gaps in the data availability plot (Figure 4.2) highlight that some stations might have a regular power problem. This is also reflected in the $\delta v/v$ computed from the autocorrelations of the CBH9, QALA, and MELT stations (Figures 5.5d-f), which have a lack of scatter points during specific time periods. Station CBH9 was switching on and off from January to June 2019, and was completely switched off up till August 2019. The sudden change in $\delta v/v$ from -1.5% to $\sim$ 0.5% is due to the reconfiguration of station CBH9 that occurred in the beginning of March 2020. The network code of station CBH9 was switched from MT to ML at this point. Station QALA was also reinstalled, and this is signified by the sudden change in $\delta v/v$ from $\sim$ -1% to 1% in January 2019. Similarly, station MELT, apart from being reconfigured and experiencing power cuts, was also flooded due to heavy rainfall at a point between April 2019 and February 2021. The network codes of stations QALA and MELT was also switched from MT to ML. Despite the reconfigurations, the $\delta v/v$ is still computed after the station, as expected, however it is interesting to see how small changes to a station can yield significant changes in the $\delta v/v$. These may be due to slight changes in the vertical orientation of the station and the other components, when reinstalled. Separate reference CCFs might need to be considered for the parts of the $\delta v/v$ computed before and after the station reinstallation. One of the limitations of MSNoise is that the user cannot set individual references when there are timing errors, missing data, power problems or the reconfiguration of the stations. The user is strictly limited to setting the start and end date of one individual reference. This limitation is thought to have been considered in the latest version of MSNoise.

CCF against time plots provide the opportunity to do this by identifying possible timing errors in the data from the seismic stations. Timing problems can be visually noted in a single CCF, or noticed when comparing several days, weeks, or months of CCFs, whereby the CCFs will be asymmetric. The CCF against time lag plot for the cross-correlation of MSDA-WDD shows consistent day-to-day waveforms and thus, that none of the stations MSDA or WDD have an unlikely timing problem. The shifted CCFs in the cross-correlations of MSDA-XLND (Figure 6.1a) and WDD-XLND (Figure 6.1b) suggest that station XLND has a timing error from mid-2019 till the end of 2021 due to the shifted CCFs. The same issue has been identified for station MELT (Figures 6.1c and d) during 2021, and for station QALA (Figures 6.1e and f) in the end of 2020. These timing problems were confirmed by the network operators and were either due to the GPS antenna being damaged or obstructed, or because of cabling problems.

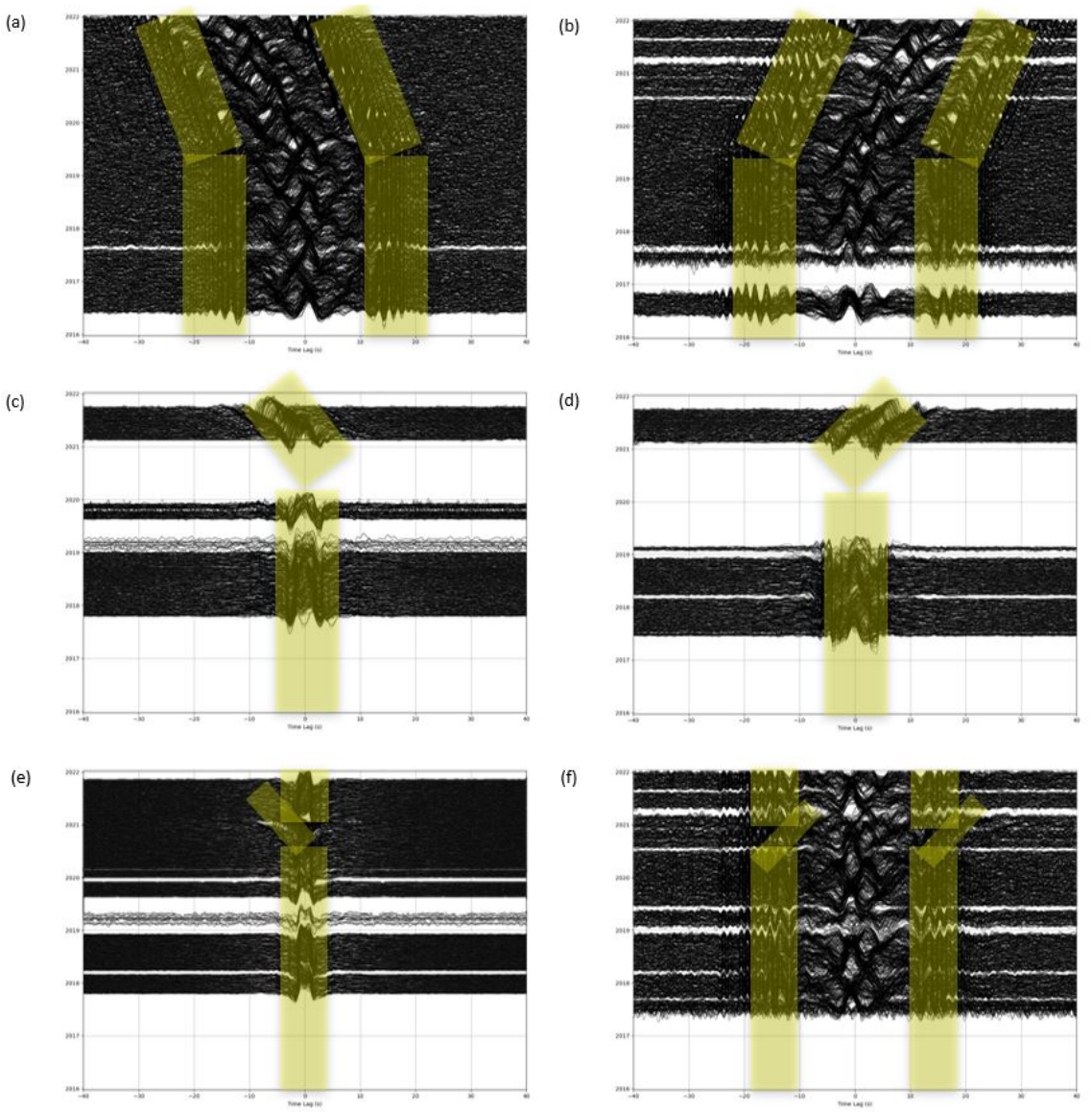

Figure 6.1.: CCF against time lag plots showing examples of timing problems of broadband stations. The yellow boxes highlight the shifted peaks of the CCFs which are caused by timing errors. Timing problems can be observed in the cross-correlations of: (a) MSDA-XLND, (b) WDD-XLND, (c) CBH9-MELT, (d) MELT-QALA, (e) CBH9-QALA, and (f) QALA-WDD. Station XLND has a timing problem from mid-2019 till the end of 2021. MELT and QALA have timing problems during 2021, and the end of 2020 respectively. See Figure 4.5 for details of the plots.

These timing problems can also be noted in the $\delta v/v$. In the $\delta v/v$ plot for the cross-correlation of CBH9-XLND (Figure 5.4a), the presumed timing problem of XLND can be noticed from the sudden reduction in number of $\delta v/v$ scatter points from mid-2019 onwards. Due to the timing problem, either a bad or no solution could have been found in computing the $\delta t/t$, which led to a lack of data points and wrong estimates (decreased $\delta v/v$ in summer). Similarly, the timing problem of station MELT in 2021 is noticeable from the $\delta v/v$ plot of the cross-correlation of CBH9-MELT (Figure 5.4c). A visible decrease in the number of $\delta v/v$ scatter points and an unexpected pattern can be observed in 2021. For this

reason, when looking at seasonal variations, timing errors in the $\delta v/v$ were considered.

Interestingly, timing problems cannot be identified in the CCF-time lag plots of autocorrelations because the CCF cancels out such a negligible error when correlating data of the same day and station. Thus the $\delta v/v$ of autocorrelations are still valid and can be used. In fact, station XLND maintains the seasonal changes throughout the dataset when seen through its autocorrelation function (Figure 5.5c). At present, the timing problems of all MSN stations have been resolved. This would ensure that if continuous monitoring of the $\delta v/v$ were to be done, clearer seasonal and annual variations in the $\delta v/v$ may be observed.

6.2. Seasonal variations and amplitude of seismic velocity changes

In general, the results show a satisfactory quality of the $\delta v/v$ based on seasonal and annual variations for both the cross- and autocorrelations of broadband and short-period stations. It is of note that the cross-correlations between broadband stations did not turn out as good as one would have expected. This could possibly be due to various reasons such as: timing and station problems, long distance between stations, station paths crossing heterogeneous geology, crossing different aquifers, and across the sea. Still, seasonal variations in the $\delta v/v$ from cross-correlations of broadband stations could be observed to a certain extent, but not as pronounced as the seasonal variations in the $\delta v/v$ from the short-period stations. On the other hand, autocorrelations resulted in more pronounced seasonal variations in the $\delta v/v$ for both broadband and short-period stations.

To our knowledge, $\delta v/v$ studies have not yet considered cross-correlations of broadband with short-period stations to link changes in seismic velocity with groundwater level. Most studies only computed cross- and autocorrelations of ambient seismic noise data from broadband stations (Clements and Denolle, 2018; Illien et al., 2021; Kim and Lekic, 2019; Lecocq et al., 2017; Mao et al., 2022; Meier et al., 2010), while Wang et al. (2017) used short-period stations to detect changes in seismic velocities across Japan. The results of the present study show that the combination of both types of stations can also be used especially when deploying temporary networks.

Cross-correlations of broadband station pairs yielded a seismic velocity change of a higher amplitude (maximum of $\sim$0.3%) than the cross-correlations between broadband and short-period, or between short-period stations (maximum of $\sim$0.15%). These seismic velocity changes are similar in amplitude to the peak variations in the $\delta v/v$ from other studies, such as a $\sim$0.2% variation in the $\delta v/v$ from Clements and Denolle (2018). However, changes in groundwater level of 25 m were observed in San Gabriel Valley over a 17-year period (Clements and Denolle, 2018), which are much larger than the groundwater variations exhibited in Malta. Some other studies found maximum variations of $\sim$0.07%

(Mao et al., 2022) and ∼0.02% (Lecocq et al., 2017) in the $\delta v/v$ that are smaller than the maximum variations obtained in this study. Basins near Los Angeles, California (including the San Gabriel Valley) experienced changes in groundwater level of ∼17 m over a 20-year period (Mao et al., 2022). Despite these significant groundwater level changes, the changes in seismic velocity are smaller than the maximum variations in $\delta v/v$ from this study. The study conducted in the Grafenberg Array in south-east Germany (Lecocq et al., 2017) experienced maximum water level variations of ∼2 m over an 18-year period in the area's complex aquifer system. These groundwater level variations are less than the one exhibited in Malta, which may explain the smaller change in seismic velocity from Lecocq et al. (2017).

It is important to note that these studies averaged for the $\delta v/v$ throughout the whole period that ambient seismic noise data was collected (e.g., Clements and Denolle, 2018; Lecocq et al., 2017; Mao et al., 2022). This allowed for the identification of long-term trends in the $\delta v/v$. For example, Mao et al. (2022) averaged the $\delta v/v$ because data from a total of 50 broadband stations was utilised, which was much more than the number of stations considered in this study. The seismic noise and water level datasets in the present study only covered a period of six years. Therefore, identifying long-term, decades-long trends in the $\delta v/v$ was not within the scope of this study.

From the cross-correlations of seismic noise recorded from short-period stations, Wang et al. (2017) generally found seismic velocity changes that are similar in amplitude to the $\delta v/v$ from the cross-correlation of short-period stations in the Maltese islands.

Here, it was also noted that autocorrelations have produced larger variations in the $\delta v/v$. Autocorrelations of broadband and short-period stations show a maximum variation of $\delta v/v$ of ∼1% and ∼2%, respectively. Cross-correlations from the present study generally show maximum variations in the $\delta v/v$ of ∼0.3%, which is an order of magnitude less than the autocorrelations. D'hour et al. (2016) also observed that autocorrelations are capable of sampling larger depths and are more sensitive to local changes in the $\delta v/v$. Other studies demonstrated stronger maximum variations in the $\delta v/v$ from autocorrelations, at ∼8% (Illien et al., 2021) and ∼15% (Kim and Lekic, 2019). These studies only used a maximum of two stations for autocorrelation. The study by Illien et al. (2021) was conducted in the Himalayan mountain ranges which transport large volumes of water downstream from glacier melt. This may lead to larger groundwater level fluctations (Illien et al., 2021) when compared to the Maltese islands, which range from 0.279-3.387 m in this study. Kim and Lekic (2019) also detects groundwater level fluctuations of 0-25 m in the Gulf Coast Aquifer system (southern Texas). Greater water level fluctuations may have led to changes in $\delta v/v$ of a higher amplitude from autocorrelations in these studies.

An interesting note is about the sign of the amplitude of the $\delta v/v$ from cross- and autocorrelations of the seismic stations in Malta. As expected, the $\delta v/v$ from cross-correlations crossed between the negative and positive axes. Contrastingly, autocorrelations did not

exhibit the same change in sign. The autocorrelations of broadband and short-period stations led to $\delta v/v$ that remained in the negative and positive axes, respectively. However, the $\delta v/v$ from the autocorrelation of some broadband stations was noted to switch from the negative to the positive axis once the stations were reconfigured (see Section 6.1).

6.3. Errors in the data

There are two types of errors in the seismic data that were considered in the processing: errors of the individual daily measurements, and error for the rolling average. In the MWCS technique by Clarke et al. (2011), an error is generated for every daily measurement when performing the weighted linear regression (WLS, see section 4.7). The error of each scatter point is calculated from the gradient of the WLS. MSNoise caters for scatter points with a large error with the *dtt_maxerr* parameter. This sets a maximum limit on the error on the δt measurement. MWCS points that have a δt measurement error that is greater than *dtt_maxerr* (0.1 s) are not used in the WLS. From the daily DTT file that MSNoise generates, the errors on a daily basis for every $\delta v/v$ data point can be plotted as shown in Figure 6.2. An error bar was not plotted for some scatter points because the error was not generated by the WLS.

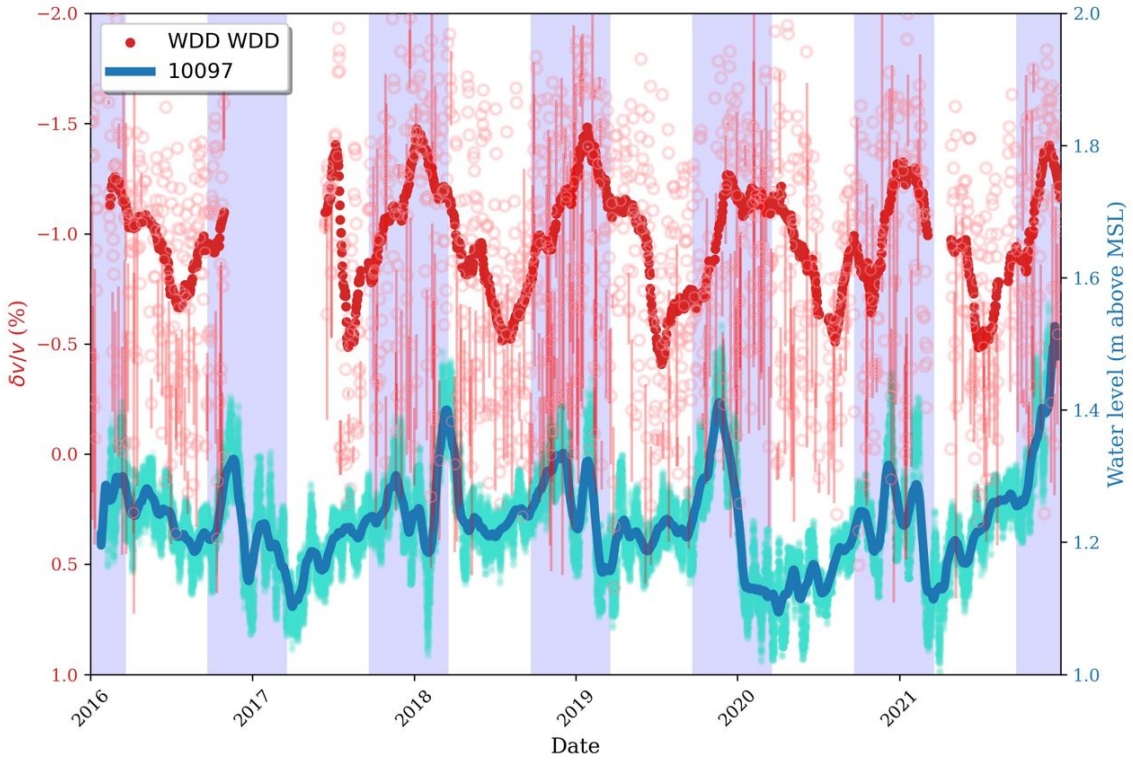

Figure 6.2.: Plot showing an example of the errors (vertical red lines) on the daily $\delta v/v$ data points.

The standard deviation was used as the representative error of the rolling average of the $\delta v/v$ (semi-transparent vertical grey bands in Figure 6.3). In order to obtain robust and smoother rolling averages, outlier scatter points of the $\delta v/v$ that did not fall within the standard deviation were then neglected in a second run of the rolling average calculation.

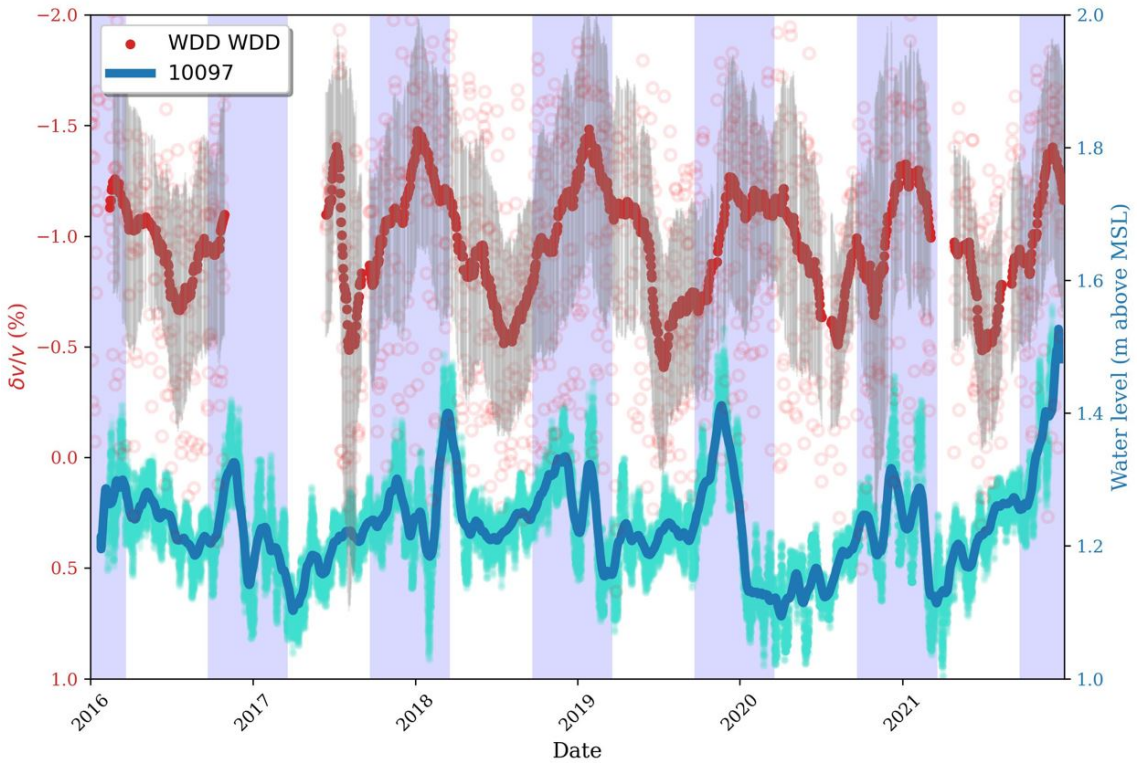

Figure 6.3.: Example of the standard deviation calculated on the $\delta v/v$. Scatter points of the $\delta v/v$ that do not fall within the standard deviation (semi transparent vertical grey bands) were not used in the rolling average calculation.

6.4. Filtering

In this study, the CCFs were processed with two types of filters, 0.1-1 Hz and 0.3-3 Hz. This was intended to obtain the best quality of $\delta v/v$, according to the two types of stations that were used. These frequency ranges are similar or within the range of other studies (e.g., Clements and Denolle, 2018; Lecocq et al., 2017; Mao et al., 2022).

As expected, the quality of the $\delta v/v$ from cross- and autocorrelations of broadband stations was better when using the 0.1-1 Hz filter. In the case of cross- and autocorrelations of short-period stations, the 0.3-3 Hz filter showed better quality of the $\delta v/v$. An interesting observation in the results was that the $\delta v/v$ computed from the cross-correlation of broadband and short-period station pairs was of better quality when using the 0.3-3 Hz filtering band. This shows that the PSD analysis in Section 3.2 was beneficial in determining the optimum frequency range for the data here to be processed. For this reason, the results in

this study were presented after being processed with the above-mentioned filters for each type of cross- and autocorrelation station pair setup.

6.5. Interstation distance

In an effort to establish any recognisable temporal variation in the $\delta v/v$ from each cross-correlation station pair at different interstation distances, all of the data was looked at and judged accordingly. It is observed that the quality of the $\delta v/v$ deteriorates with increased interstation distance, as shown in Table 6.1. The table also lists details about the medium being sampled in each cross-correlation function, such as if the medium crosses different types of geology, or the sea. At longer interstation distances, the medium being sampled between both stations is more likely to cross different types of geological layers and aquifers. Computing cross-correlations across the three islands would also mean that the sea would be part of the medium that is being sampled. The list of cross-correlations in Table 6.1 are sorted by interstation distance in ascending order. The station pairs with the shortest interstation distance tend to have better quality of the $\delta v/v$ and a more pronounced seasonal variation. The seasonal variation of the $\delta v/v$ also correlate quite well with the water level measurements from nearby boreholes. For example, CBH9-QALA, FM01-FM02, XLND-FM04, FM02-FM03, QALA-FM04, MELT-FM05, FM03-FM05, and MSDA-FM02 have interstation distances between 2.4-6.0 km.

In general, the quality of the $\delta v/v$ with respect to the seasonal variation is poor at the longest interstation distances, such as FM01-FM04, XLND-FM02, QALA-WDD, XLND-FM01, WDD-FM04, and WDD-XLND. Figure 6.4 shows the plot of the $\delta v/v$ for the cross-correlation of these station pairs, against the water level data from nearby boreholes. These station pairs all have an interstation distance varying from 28.0-34.9 km. During certain months, the quality of the $\delta v/v$ can be considered sufficient (for example in Figures 6.4a, b, and e), such that the seasonal variations in the $\delta v/v$ even matches with the water level data. However, it is clear that the general quality of the $\delta v/v$ deteriorates at longer interstation distances, with seasonal variations in the $\delta v/v$ becoming less obvious. Presumable, this is because of a loss in quality of the cross-correlation functions. Meier et al. (2010) stated that the signal of cross-correlations was observed to decrease with increasing interstation distance, however their interstation distances reached 200 km, which are much longer than the interstation distances of this study. Studies that were conducted at interstation distances similar to this study (e.g., Clements and Denolle, 2018; Lecocq et al., 2017) did not comment on how the quality of the cross-correlation signal changes at the longer interstation distances.

Table 6.1. Data quality assessment based on interstation distance. Table showing the station pairs, their interstation distance (km), information about the medium being sampled, and the assessment of any recognisable temporal or seasonal variation in the $\delta v/v$ from each cross-correlation station pair. Station pairs that are in bold have been presented as results in Chapter 5.

Station pair	Interstation distance (km)	Medium crossing different geology types?	Medium crossing the sea?	Assessment based on seasonal change
CBH9-QALA	2.4	No	Yes	Good
FM01-FM02	3.3	No	No	Good
XLND-FM04	4.0	No	No	Good
FM02-FM03	4.9	Yes	No	Good
QALA-FM04	5.0	Yes	No	Good
MELT-FM05	5.1	No	No	Good
FM03-FM05	5.1	No	No	Good
MSDA-FM02	6.0	No	No	Good
CBH9-FM04	6.4	Yes	Yes	Good
FM03-FM06	6.5	Yes	No	Good
MELT-FM06	7.0	Yes	No	Good
FM01-FM03	7.1	Yes	No	Fair
MSDA-FM06	7.2	No	No	Good
FM02-FM06	7.3	No	No	Good
WDD-FM02	7.3	No	No	Good
MSDA-FM03	7.4	Yes	No	Fair
WDD-FM01	7.4	No	No	Good
MSDA-WDD	8.0	No	No	Bad
CBH9-MELT	8.2	No	Yes	Good
FM05-FM06	8.2	Yes	No	Good
MELT-FM03	8.4	Yes	No	Fair
MSDA-FM01	9.0	No	No	Fair
QALA-XLND	9.1	Yes	No	Fair
FM02-FM05	9.8	Yes	No	Good
CBH9-XLND	10.2	Yes	Yes	Good
QALA-MELT	10.5	No	Yes	Fair
FM01-FM05	11.3	Yes	No	Good
CBH9-FM06	11.4	Yes	Yes	Good
WDD-FM03	12.0	Yes	No	Fair
MSDA-FM05	12.2	Yes	No	Good
MELT-FM04	12.5	Yes	Yes	Fair
FM01-FM06	12.8	No	No	Good
CBH9-FM05	13.2	No	Yes	Good
MELT-FM02	13.2	Yes	No	Fair
MSDA-MELT	13.5	Yes	No	Fair
QALA-FM06	13.7	Yes	Yes	Bad
XLND-MELT	15.0	Yes	Yes	Fair
MELT-FM01	16.0	Yes	No	Fair
QALA-FM05	15.5	No	Yes	Bad
CBH9-FM03	15.8	Yes	Yes	Bad
WDD-FM05	17.1	Yes	No	Good
FM04-FM05	17.2	Yes	Yes	Bad
FM04-FM06	17.5	Yes	Yes	Good
QALA-FM03	18.2	Yes	Yes	Bad
MSDA-CBH9	18.6	Yes	Yes	Bad
XLND-FM05	19.1	Yes	Yes	Bad
WDD-FM06	20.0	No	No	Good
WDD-MELT	20.0	Yes	No	Bad
CBH9-FM02	20.3	Yes	Yes	Fair
XLND-FM06	20.7	Yes	Yes	Bad
MSDA-QALA	20.8	Yes	Yes	Bad
FM03-FM04	20.8	Yes	No	Good
QALA-FM02	22.7	Yes	Yes	Bad
CBH9-FM01	23.0	Yes	Yes	Fair
XLND-FM03	23.3	Yes	Yes	Bad
MSDA-FM04	24.7	Yes	Yes	Bad
QALA-FM01	25.4	Yes	Yes	Bad
FM02-FM04	25.6	Yes	Yes	Fair
WDD-CBH9	26.2	Yes	Yes	Bad
MSDA-XLND	27.9	Yes	Yes	Fair
FM01-FM04	28.0	Yes	Yes	Fair
XLND-FM02	28.2	Yes	Yes	Bad
QALA-WDD	28.5	Yes	Yes	Bad
XLND-FM01	30.3	Yes	Yes	Bad
WDD-FM04	32.0	Yes	Yes	Bad
XLND-WDD	34.9	Yes	Yes	Bad

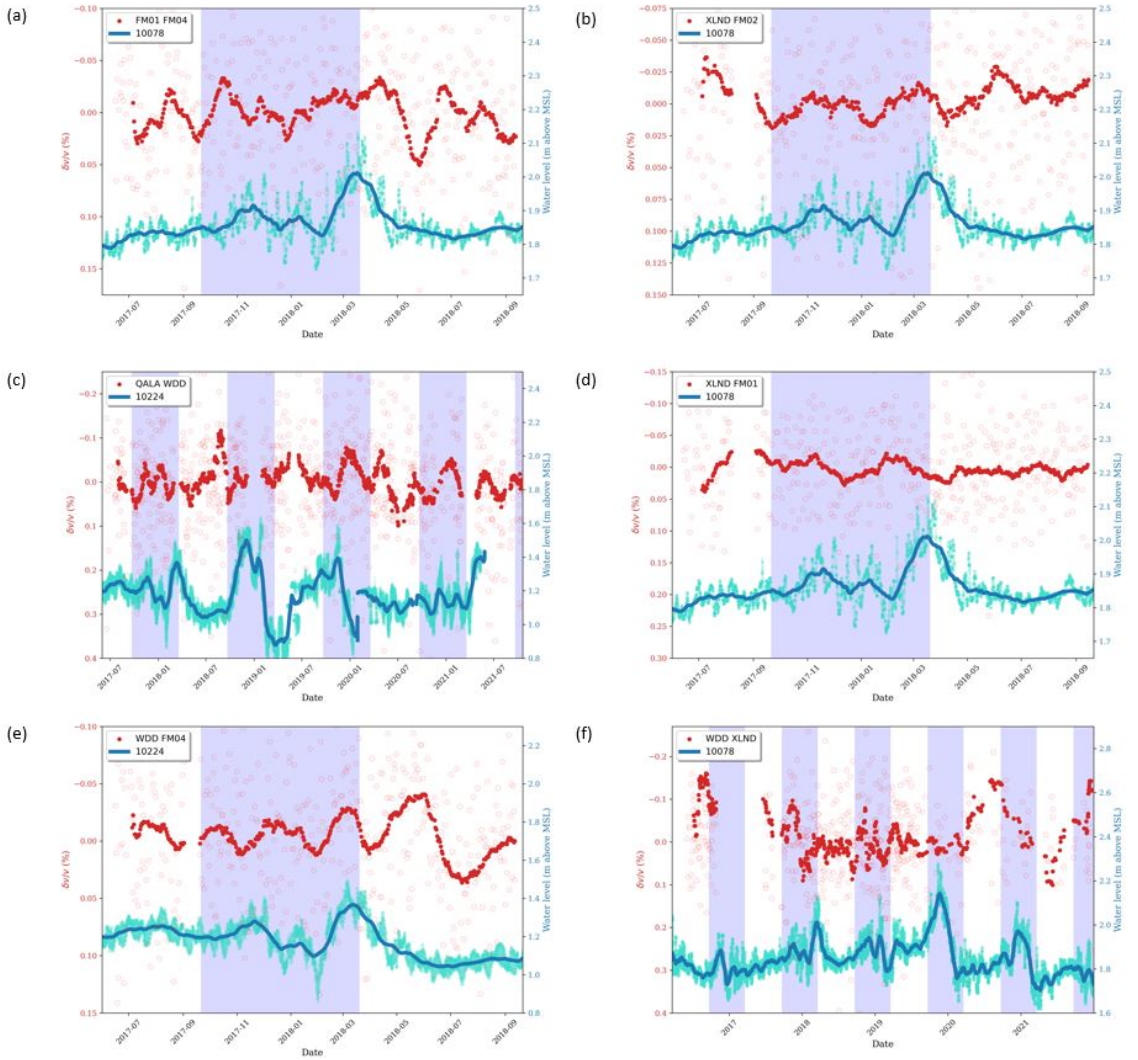

Figure 6.4.: Plots showing changes in seismic velocity ($\delta v/v$) from the cross-correlations of broadband and short-period stations at a long interstation distance, and water level data from neaby boreholes: (a) FM01-FM04 (borehole 10078, Gomerino), (b) XLND-FM02 (borehole 10078, Gomerino), (c) QALA-WDD (borehole 10224, Mdawra 1), (d) XLND-FM01 (borehole 10078, Gomerino) (e) WDD-FM04 (borehole 10224, Mdawra 1), and (f) WDD-XLND (borehole 10078, Gomerino). These station pairs have an interstation distance varying from 28.0-34.9 km. See Figure 5.1 for details on the plots.

It is difficult to establish a cut-off interstation distance that determines the quality of the seasonal variations in the $\delta v/v$. In a few cases, seasonal variations in $\delta v/v$ can still be of good quality at high interstation distances. For example, the cross-correlations of FM04-FM06, WDD-FM06, and FM03-FM04 all show good seasonal variations in the $\delta v/v$ (see Table 6.1). In contrast at shorter interstation distances, seasonal variations in the $\delta v/v$ are not always observed as is the case for MSDA-FM03 (7.4 km) and MSDA-FM01 (9.0 km) (Figure 6.5). The lack of agreement could also be because of the choice of filter, as might be the case of the broadband station pair of MSDA-WDD (at an interstation distance of 8.0 km). Despite being broadband stations, this station pair shows seasonal $\delta v/v$ variations of lower quality at 0.1-1 Hz (Figure 6.6a), when compared to the 0.3-3 Hz

filter (Figure 6.6b).

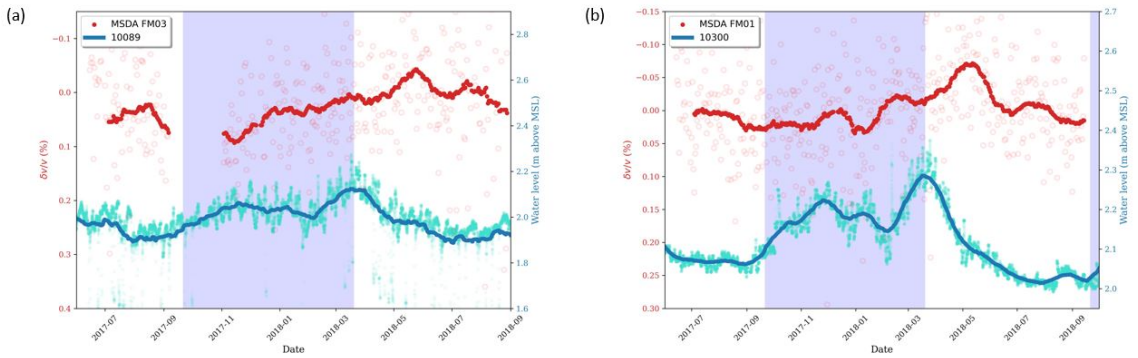

Figure 6.5.: Plots showing changes in seismic velocity ($\delta v/v$) from cross-correlations against water level data from the nearest borehole: (a) MSDA-FM03 (borehole 10089, L-Gharbi) (b) MSDA-FM01 (borehole 10300, Hal Farruġ). Both station pairs have a relatively short interstation distance of 7.4 km and 9.0 km, respectively. The CCFs were filtered at 0.3-3 Hz in this plot. Seasonal variations of the $\delta v/v$ are not as clear as one would expect at these interstation distances. See Figure 5.1 for details on the plots.

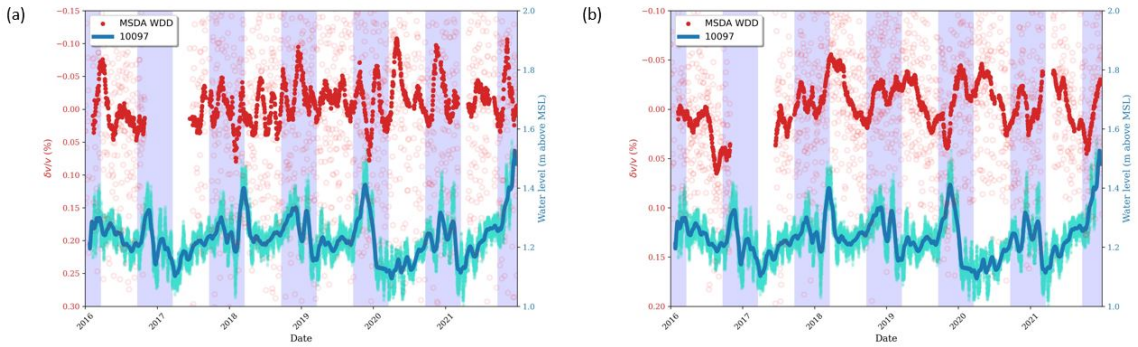

Figure 6.6.: Plots showing changes in seismic velocity ($\delta v/v$) from the MSDA-WDD cross-correlation at both tested filters: (a) 0.1-1 Hz, (b) 0.3-3 Hz. The MSDA-WDD station pair has a relatively short interstation distance of 8.0 km. Seasonal variations of the $\delta v/v$ are not as clear as one would expect when using the 0.1-1 Hz filter. Better seasonal variations can be observed when CCFs were filtered at 0.3-3 Hz. See Figure 5.1 for details on the plots.

6.6. Meteorological considerations

Numerous studies have tested for a correlation between variations in $\delta v/v$ and seasonal variations of meteorological parameters such as precipitation (Hillers et al., 2015, 2014; Illien et al., 2021; Sens-Schönfelder and Wegler, 2011; Wang et al., 2017), air temperature (Clements and Denolle, 2018; Lecocq et al., 2017; Mao et al., 2019; Meier et al., 2010), and atmospheric pressure (Hillers et al., 2015). Precipitation, air temperature and atmospheric pressure data were obtained from the meteorological station at the national airport in Luqa (Figure 6.7). This study did not go into the correlation between these meteorological

parameters and seasonal changes in the $\delta v/v$, mainly due to time constraints. Nevertheless, a plot of the data shows seasonal patterns for all three parameters, as expected, particularly the precipitation and temperature. Naturally, these show general agreement with the $\delta v/v$ from station WDD, the closest seismic station to the Luqa meteorological station (Figures 6.7a-c).

The amount of water from precipitation that percolates into the underground, shallow rock layers depend on the degree of surface runoff exhibited in the area. For example, urban regions tend to exhibit lower groundwater recharge rates (and more surface runoff) when compared to more agricultural ones, due to a higher degree of impervious areas (Niemczynowicz, 1999). In agricultural areas, the types of agricultural practices used, and soil properties such as texture, porosity, bulk density and hydraulic conductivity all determine how much rainwater percolates into groundwater (Owuor et al., 2016). Agricultural practices and soil properties are variable from one area to another, which may also contribute to varying levels of surface runoff and hence, water levels from boreholes. Precipitation events may not have an instant effect on the $\delta v/v$, as shown by Illien et al. (2021). Additionally, the effect on the $\delta v/v$ may vary from one place to another depending on the amount of rainfall percolating to groundwater, or that is being lost to surface runoff in a specific location.

The amount of rainwater percolating to groundwater also depends on whether rainfall events are constant and gradual, or more intense. Gradual rain events would allow rainwater to steadily percolate through the vadose zone and into groundwater, since the soil would not immediately reach its field capacity. Generally, this is not the case for Malta. Due to Malta's rainfall events being mainly torrential, the field capacity of the soil is easily reached, and this may lead to water stored in the soil pores to block subsequent rainwater from percolating down into groundwater.

Generally, studies that looked at how variations in the $\delta v/v$ correlate with precipitation found that peaks in the $\delta v/v$ coincide with precipitation events. Similarly, a visual agreement between precipitation events and the variation in $\delta v/v$ can be seen for the autocorrelation of station WDD (Figures 6.7a and b). Although this is encouraging, a detailed investigation is necessary to establish the relationship between precipitation and its effect on groundwater levels and changes in the seismic velocity, whilst taking into account the above-mentioned considerations.

Changes in air temperatures may also influence the changes in $\delta v/v$ in the Earth's shallow crustal layers (e.g., Clements and Denolle, 2018; Lecocq et al., 2017; Mao et al., 2019; Meier et al., 2010). Although air temperature changes affect the $\delta v/v$ in the first tens to hundreds of centimetres of the Earth's crust, these changes induce thermoelastic strains in the crust (Mao et al., 2019) that may extend even deeper (Tsai, 2011). A study by Hillers et al. (2015) found that changes in air temperature and thermoelastic strain dominate changes in $\delta v/v$ in the shallow crustal layers of an arid region. On the other hand,

Clements and Denolle (2018) concluded that changes in seismic velocity were mainly derived by hydrological effects rather than thermoelastic strains. It was also shown that a mixture of both hydrological effects and thermoelastic strains may determine the changes in seismic velocity in the medium being studied (Lecocq et al., 2017).

In Figure 6.7c, the seasonal air temperature changes seem very regular in period and amplitude, with higher temperatures in the summer periods and lower temperatures in the winter periods. In general, increases in air temperature coincide with troughs in the $\delta v/v$. However, the $\delta v/v$ have more irregular patterns that seem to relate to the precipitation such as the case of winter 2020, when it rained less and the $\delta v/v$ amplitude is less pronounced. In general, increases in air temperature coincide with troughs in the $\delta v/v$. The aim of the present study was to understand how seismic velocities change with variations in groundwater levels in Maltese aquifers. The role that seasonal temperature variations may have on the $\delta v/v$ in the subsurface rocks of the Maltese islands was not considered. Nevertheless, very good agreement of some patterns in $\delta v/v$ with corresponding patterns in the water level (e.g., Figures 5.2e and 5.3b) can be observed. Additionally, episodes of groundwater abstraction from a nearby borehole correspond very well with troughs in the $\delta v/v$ from station MSDA (Figure 5.5a). These patterns lead us to believe that the water content, at least in certain regions, has a larger influence than temperature on seismic velocity changes.

The effect that atmospheric pressure may have on seismic velocity changes was considered as negligible in one study by Hillers et al. (2015). Atmospheric pressure data (Figure 6.7d) shows that there is a seasonal variation in atmospheric pressure in Malta, with higher pressures in winter, and lower pressures in summer. Detailed studies to understand the effect that these meteorological parameters may have on the seismic velocity changes in the Maltese islands are desirable.

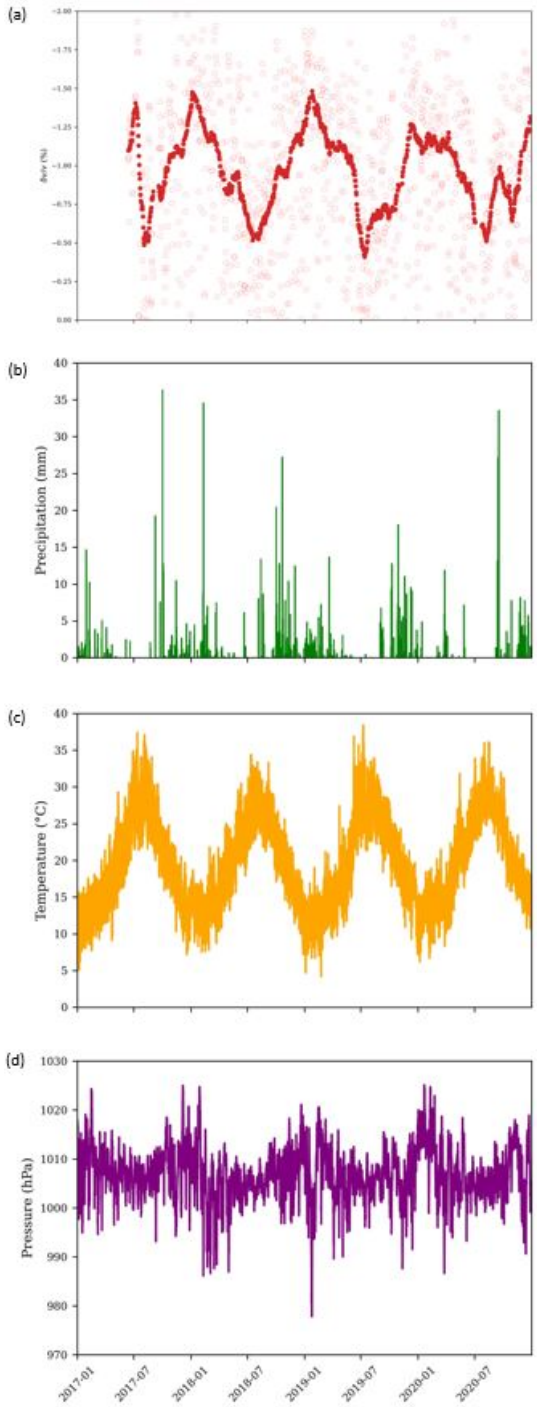

Figure 6.7.: Meteorological considerations. A plot showing recorded meteorological parameters and seismic velocity changes: (a) $\delta v/v$ plot from the autocorrelation of station WDD, (b) precipitation (mm), (c) air temperature (°C), and (d) pressure (hPa).

6.7. Future work

The aim of this study was to identify any form of correlation between temporal changes in seismic velocities, derived from cross- and auto-correlations of ambient seismic noise, with water level change data from nearby boreholes. MSNoise (Lecocq et al., 2014) provides the

opportunity of daily and routine monitoring of $\delta v/v$, which could provide a real-time tool to continuously monitor groundwater in the Maltese islands. The present study only looked at the vertical component of the seismic data, mainly due to time limitations. Future studies could make use of the horizontal components to investigate if there are any increased sensitivities in the compared $\delta v/v$.

Attempting to differentiate between the very shallow perched aquifer and the mean sea-level aquifer when looking at the $\delta v/v$ could also be considered, using other frequency filtering techniques such as the wavelet transform method. These would provide a more complete picture of the hydrogeological processes, and demonstrate how ambient seismic noise can complement *in-situ* borehole measurements at different depths and scales to ensure more accurate quantitative groundwater monitoring for the Maltese islands. The seismic data can also be used for other geophysical studies, such as Horizontal-to-Vertical-Spectral-Ratios (HVSR). The HVSR technique would be best applied in regions that are underlain by the BC layer and demonstrate a prominent and consistent site resonance frequency. Changes in water content of the rocks lead to changes in the shallow seismic velocities and hence to changes in the site response frequency, providing a further possible monitoring tool. Another popular technique is seismic tomography. Unlike point measurements or station pairs, tomography can map information of the structures across all the islands and can be processed over different timescales to determine possible seasonal changes in the tomographic models.

The installation of more seismic stations in the Maltese archipelago as planned by the Seismic Monitoring and Research Group, would present an opportunity for better coverage and for more accurate $\delta v/v$ computations to compare to borehole readings for groundwater monitoring in a more localised context. As more seismic data is collected over the years, it would also be interesting to identify any long-term, decades-long variations in the $\delta v/v$ and how these correlate with long-term seasonal variations in water level and the discussed meteorological parameters.

Possible future projects such as Managed Aquifer Recharge (MAR) in Maltese aquifers would present a good opportunity to establish relationships between the injected volume of water and the changes in $\delta v/v$. Such experiments may also help establishing to what extent meteorological parameters such as precipitation, air temperature and atmospheric pressure have an effect on the $\delta v/v$.

7. Conclusion

In conclusion, the results demonstrate that seasonal and annual changes in the groundwater levels can be detected by changes in seismic velocity ($\delta v/v$) for small islands such as Malta. Two types of stations were investigated: six broadband from the Malta Seismic Network (MSN) and six short-period from the FASTMIT network, and show that both stations can provide similar sensitivity to the $\delta v/v$ when taking into consideration appropriate filters (0.1-1 Hz for the broadband and 0.3-3 Hz for the short-period stations). The method works for both cross- and autocorrelation functions of ambient seismic noise, the latter being an order of magnitude more sensitive. Cross-correlations of broadband station pairs yielded a seismic velocity change of a higher amplitude (maximum of $\sim$0.3%) than the cross-correlations of short-period, or of broadband and short-period station pairs (maximum of $\sim$0.15%). On the other hand, autocorrelations of broadband and short-period stations show a maximum variation of $\delta v/v$ of $\sim$1% and $\sim$2%, respectively.

The cross-correlation of short-period stations, and of short-period with broadband stations provided the best seasonal variations of $\delta v/v$ from cross-correlations. Generally, seasonal and annual variations of the $\delta v/v$ from autocorrelations of some stations were found to be more pronounced than from cross-correlations. While an agreement is not always obvious, in general, temporal variations in the $\delta v/v$ coincide with those in the water level data. This gives us confidence that $\delta v/v$ may act as a suitable proxy for monitoring groundwater levels in the Maltese islands in regions where borehole measurements are sparse.

Timing problems and other station errors were also identified from the results before attempting to interpret the data. The quality of the $\delta v/v$ was observed to deteriorate at longer interstation distances when seasonal variations in the $\delta v/v$ are less obvious. Presumable, this is because of a loss in quality of the cross-correlation functions since the longer interstation paths tend to traverse more complex geology, different types of aquifers, or even the sea. It is difficult to establish a cut-off interstation distance that determines the quality of the seasonal variations in the $\delta v/v$ because, in a few cases, seasonal variations in $\delta v/v$ were still of good quality at high interstation distances.

A number of considerations for future work were listed in Section 6.7. These present promising research opportunities in the view of enhanced groundwater monitoring for the Maltese islands, and for other similar island environments globally.

Bibliography

Agius, M., D'Amico, S., and Galea, P. (2015). Setting up the Malta Seismic Network: instrumentation, site selection and real-time monitoring. In Lombardo, G. and Panzera, F., editors, *Establishment of an integrated Italy-Malta cross border system of Civil Protection: Geophysical Aspects*, pages 11–30. Aracne.

Agius, M., Magrini, F., Diaferia, G., Kästle, E., Cammarano, F., Faccenna, C., Funiciello, F., and van der Meijde, M. (2022). Shear-velocity structure and dynamics beneath the Sicily Channel and surrounding regions of the Central Mediterranean inferred from seismic surface waves. *Geochemistry, Geophysics, Geosystems*, 23(10).

Agius, M. R., D'Amico, S., Galea, P., and Panzera, F. (2014). Performance evaluation of Wied Dalam (WDD) seismic station in Malta. *Xjenza*, 2(1):72–80.

Alexander, D. (1988). A review of the physical geography of Malta and its significance for tectonic geomorphology. *Quaternary Science Reviews*, 7(1):41–53.

Asefa, T., Kemblowski, M. W., Urroz, G., McKee, M., and Khalil, A. (2004). Support vectors–based groundwater head observation networks design. *Water Resources Research*, 40(11).

Asten, M. W. (1978). Geological control on the three-component spectra of Rayleigh-wave microseisms. *Bulletin of the Seismological Society of America*, 68(6):1623–1636.

Asten, M. W. and Henstridge, J. (1984). Array estimators and the use of microseisms for reconnaissance of sedimentary basins. *Geophysics*, 49(11):1828–1837.

Bakalowicz, M., Mangion, J., et al. (2003). The limestone aquifers of Malta: Their recharge conditions from isotope and chemical surveys. *International Association of Hydrological Sciences, Publication*, (278):49–54.

Baldassini, N. and Di Stefano, A. (2017). Stratigraphic features of the Maltese Archipelago: a synthesis. *Natural Hazards*, 86(2):203–231.

Bawden, G. W., Thatcher, W., Stein, R. S., Hudnut, K. W., and Peltzer, G. (2001). Tectonic contraction across Los Angeles after removal of groundwater pumping effects. *Nature*, 412(6849):812–815.

Bensen, G., Ritzwoller, M., Barmin, M., Levshin, A. L., Lin, F., Moschetti, M., Shapiro, N., and Yang, Y. (2007). Processing seismic ambient noise data to obtain reliable

broad-band surface wave dispersion measurements. *Geophysical journal international*, 169(3):1239–1260.

Beyreuther, M., Barsch, R., Krischer, L., Megies, T., Behr, Y., and Wassermann, J. (2010). Obspy: A Python toolbox for seismology. *Seismological Research Letters*, 81(3):530–533.

Blaine, B. E. (2018). Winsorizing. In Frey, B., editor, *The SAGE encyclopedia of educational research, measurement, and evaluation*, pages 1817–1818. SAGE Publications.

Bonnefoy-Claudet, S., Cotton, F., and Bard, P.-Y. (2006). The nature of noise wavefield and its applications for site effects studies: A literature review. *Earth-Science Reviews*, 79(3-4):205–227.

Boretti, A. and Rosa, L. (2019). Reassessing the projections of the World Water Development Report. *NPJ Clean Water*, 2(1):1–6.

Boschi, E. and Morelli, A. (1994). The mednet program. *Annals of Geophysics*, 37(5).

Bozionelos, G., Galea, P., D'Amico, S., Plasencia Linares, M., Romanelli, M., Rossi, G., Vuan, A., Sugan, M., and Agius, M. (2019). An augmented seismic network to study off-shore seismicity around the Maltese Islands: The FASTMIT experiment. *Xjenza*, 7:104–121.

Brenguier, F., Campillo, M., Hadziioannou, C., Shapiro, N. M., Nadeau, R. M., and Larose, É. (2008a). Postseismic relaxation along the San Andreas fault at Parkfield from continuous seismological observations. *science*, 321(5895):1478–1481.

Brenguier, F., Campillo, M., Takeda, T., Aoki, Y., Shapiro, N., Briand, X., Emoto, K., and Miyake, H. (2014). Mapping pressurized volcanic fluids from induced crustal seismic velocity drops. *Science*, 345(6192):80–82.

Brenguier, F., Rivet, D., Obermann, A., Nakata, N., Boué, P., Lecocq, T., Campillo, M., and Shapiro, N. (2016). 4-d noise-based seismology at volcanoes: Ongoing efforts and perspectives. *Journal of Volcanology and Geothermal Research*, 321:182–195.

Brenguier, F., Shapiro, N. M., Campillo, M., Ferrazzini, V., Duputel, Z., Coutant, O., and Nercessian, A. (2008b). Towards forecasting volcanic eruptions using seismic noise. *Nature Geoscience*, 1(2):126–130.

Buhagiar, K. (2007). Water management strategies and the cave-dwelling phenomenon in late-medieval Malta. *Medieval Archaeology*, 51(1):103–131.

Campillo, M. (2006). Phase and correlation in random seismic fields and the reconstruction of the green function. *Pure and applied geophysics*, 163(2):475–502.

Campillo, M. and Paul, A. (2003). Long-range correlations in the diffuse seismic coda. *Science*, 299(5606):547–549.

Chaussard, E., Milillo, P., Bürgmann, R., Perissin, D., Fielding, E. J., and Baker, B. (2017). Remote sensing of ground deformation for monitoring groundwater management practices: Application to the Santa Clara Valley during the 2012–2015 California drought. *Journal of Geophysical Research: Solid Earth*, 122(10):8566–8582.

Christensen, N. and Wang, H. (1985). The influence of pore pressure and confining pressure on dynamic elastic properties of Berea sandstone. *Geophysics*, 50(2):207–213.

Clarke, D., Zaccarelli, L., Shapiro, N., and Brenguier, F. (2011). Assessment of resolution and accuracy of the Moving Window Cross Spectral technique for monitoring crustal temporal variations using ambient seismic noise. *Geophysical Journal International*, 186(2):867–882.

Clements, T. and Denolle, M. A. (2018). Tracking groundwater levels using the ambient seismic field. *Geophysical Research Letters*, 45(13):6459–6465.

Continental Shelf Department (2022). Geological Map of the Maltese Islands. https://continentalshelf.gov.mt/en/Pages/Geological-Map-of-the-Maltese-Islands.aspx. Accessed: 15-12-2022.

Cupillard, P., Stehly, L., and Romanowicz, B. (2011). The one-bit noise correlation: a theory based on the concepts of coherent and incoherent noise. *Geophysical Journal International*, 184(3):1397–1414.

Davy, C., Stutzmann, E., Barruol, G., Fontaine, F. R., and Schimmel, M. (2015). Sources of secondary microseisms in the Indian Ocean. *Geophysical Journal International*, 202(2):1180–1189.

Duputel, Z., Ferrazzini, V., Brenguier, F., Shapiro, N., Campillo, M., and Nercessian, A. (2009). Real time monitoring of relative velocity changes using ambient seismic noise at the Piton de la Fournaise volcano (La Réunion) from January 2006 to June 2007. *Journal of Volcanology and Geothermal Research*, 184(1-2):164–173.

D'hour, V., Schimmel, M., Do Nascimento, A. F., Ferreira, J. M., and Lima Neto, H. C. (2016). Detection of subtle hydromechanical medium changes caused by a small-magnitude earthquake swarm in NE Brazil. *Pure and Applied Geophysics*, 173(4):1097–1113.

Elshall, A. S., Castilla-Rho, J., El-Kadi, A. I., Holley, C., Mutongwizo, T., Sinclair, D., and Ye, M. (2022). Sustainability of groundwater. In *Imperiled: The Encyclopedia of Conservation*. Elsevier.

Famiglietti, J. S. (2014). The global groundwater crisis. *Nature Climate Change*, 4(11):945–948.

Farrugia, D., Paolucci, E., D'Amico, S., and Galea, P. (2016). Inversion of surface wave data for subsurface shear wave velocity profiles characterized by a thick buried low-velocity layer. *Geophysical Journal International*, 206(2):1221–1231.

Felix, R. (1973). Oligo-Miocene stratigraphy of Malta and Gozo. *Meded. Landbouwhogesch.*, 73-20:1–103.

Fenech, S., Knox, J., Borg, M., Camilleri, C., and Rizzo, A. (2019). Estimating impacts of land use change on evapotranspiration for three agricultural crops in Malta—A preliminary assessment. *Journal of Agricultural Science*, 11(3):67–74.

Fokker, E., Ruigrok, E., Hawkins, R., and Trampert, J. (2021). Physics-Based Relationship for Pore Pressure and Vertical Stress Monitoring Using Seismic Velocity Variations. *Remote Sensing*, 13(14).

Food and Agricultural Organisation (2006). Malta water resources review. Technical report, Rome, Italy.

Food and Agricultural Organisation (2020). The State of Food and Agriculture: Overcoming Water Challenges in Agriculture. Technical report, Rome, Italy.

Fowler, C. (2005). Seismology Measuring the Interior. In *The Solid Earth: An Introduction to Global Geophysics*, pages 100–186. Cambridge University Press.

Freeze, R. and Cherry, J. (1979). *Groundwater*. Prentice-hall.

Galea, P., Agius, M. R., Bozionelos, G., D'Amico, S., and Farrugia, D. (2021). A first national seismic network for the Maltese islands–The Malta seismic network. *Seismological Society of America*, 92(3):1817–1831.

Galloway, D. L. and Burbey, T. J. (2011). Regional land subsidence accompanying groundwater extraction. *Hydrogeology Journal*, 19(8):1459–1486.

Galloway, D. L. and Hoffmann, J. (2007). The application of satellite differential SAR interferometry-derived ground displacements in hydrogeology. *Hydrogeology Journal*, 15(1):133–154.

Garambois, S., Voisin, C., Romero Guzman, M., Brito, D., Guillier, B., and Réfloch, A. (2019). Analysis of ballistic waves in seismic noise monitoring of water table variations in a water field site: added value from numerical modelling to data understanding. *Geophysical Journal International*, 219(3):1636–1647.

Gemitzi, A. and Lakshmi, V. (2018). Estimating groundwater abstractions at the aquifer scale using GRACE observations. *Geosciences*, 8(11):419.

Gerstoft, P. and Tanimoto, T. (2007). A year of microseisms in southern California. *Geophysical Research Letters*, 34(20).

Giordano, M. et al. (2009). Global groundwater? Issues and solutions. *Annual review of Environment and Resources*, 34(1):153–178.

Grêt, A., Snieder, R., and Scales, J. (2006). Time-lapse monitoring of rock properties with coda wave interferometry. *Journal of Geophysical Research: Solid Earth*, 111(B3).

Grobbe, N., Mordret, A., Barde-Cabusson, S., Ellison, L., Lach, M., Seo, Y.-H., Viti, T., Ward, L., and Zhang, H. (2021). A Multi-Hydrogeophysical Study of a Watershed at Kaiwi Coast (O'ahu, Hawai'i), using Seismic Ambient Noise Surface Wave Tomography and Self-Potential Data. *Water Resources Research*, 57(4).

Groos, J. (2010). *Broadband seismic noise: classification and Green's function estimation*. PhD thesis, Karlsruher Inst. für Technologie.

Groos, J., Bussat, S., and Ritter, J. (2012). Performance of different processing schemes in seismic noise cross-correlations. *Geophysical Journal International*, 188(2):498–512.

Groos, J. and Ritter, J. (2009). Time domain classification and quantification of seismic noise in an urban environment. *Geophysical Journal International*, 179(2):1213–1231.

Gualtieri, L., Stutzmann, E., Capdeville, Y., Ardhuin, F., Schimmel, M., Mangeney, A., and Morelli, A. (2013). Modelling secondary microseismic noise by normal mode summation. *Geophysical Journal International*, 193(3):1732–1745.

Gubbins, D. (2004). *Time series analysis and inverse theory for geophysicists*. Cambridge University Press.

Gude, V. G. and Maganti, A. (2021). Desalination of deep groundwater for freshwater supplies. In *Global Groundwater*, pages 577–583. Elsevier.

Gutenberg, B. (1958). Microseisms. In *Advances in Geophysics*, volume 5, pages 53–92. Elsevier.

Hadziioannou, C., Larose, E., Coutant, O., Roux, P., and Campillo, M. (2009). Stability of monitoring weak changes in multiply scattering media with ambient noise correlation: Laboratory experiments. *The Journal of the Acoustical Society of America*, 125(6):3688–3695.

Hallett, S., Sakrabani, R., Thompson, A., Deeks, L., and Knox, J. (2017). Improving soil and water management for agriculture: insights and innovation from Malta. *Journal of Applied Research & Practice*, 1:40–59.

Hartfiel, L., Soupir, M., and Kanwar, R. S. (2020). Malta's Water Scarcity Challenges: Past, Present, and Future Mitigation Strategies for Sustainable Water Supplies. *Sustainability*, 12(23):9835.

Hasselmann, K. (1963). A statistical analysis of the generation of microseisms. *Reviews of Geophysics*, 1(2):177–210.

Healy, R. W. and Cook, P. G. (2002). Using groundwater levels to estimate recharge. *Hydrogeology journal*, 10(1):91–109.

Hedlin, M. A. and Orcutt, J. A. (1989). A comparative study of island, seafloor, and subseafloor ambient noise levels. *Bulletin of the Seismological Society of America*, 79(1):172–179.

Hillers, G., Ben-Zion, Y., Campillo, M., and Zigone, D. (2015). Seasonal variations of seismic velocities in the San Jacinto fault area observed with ambient seismic noise. *Geophysical Journal International*, 202(2):920–932.

Hillers, G., Campillo, M., and Ma, K.-F. (2014). Seismic velocity variations at TCDP are controlled by MJO driven precipitation pattern and high fluid discharge properties. *Earth and Planetary Science Letters*, 391:121–127.

Hiscock, K. M. and Bense, V. F. (2021). *Hydrogeology: principles and practice*. John Wiley & Sons.

Holden, P. and Fierer, N. (2005). Vadose Zone: Microbial Ecology. *Encyclopedia of Soils in the Environment*, pages 216–224.

House, M. (1961). Geology and Structure of the Maltese Islands. *Durham University, Department of Geography, Research Paper Series*, 5:23–31.

Illien, L., Andermann, C., Sens-Schönfelder, C., Cook, K., Baidya, K., Adhikari, L., and Hovius, N. (2021). Subsurface moisture regulates Himalayan groundwater storage and discharge. *AGU Advances*, 2(2).

Ji, K. H. and Herring, T. A. (2012). Correlation between changes in groundwater levels and surface deformation from GPS measurements in the San Gabriel Valley, California. *Geophysical Research Letters*, 39(1).

Kavusi, M., Khashei Siuki, A., and Dastourani, M. (2020). Optimal design of groundwater monitoring network using the combined Election-Kriging method. *Water Resources Management*, 34(8):2503–2516.

Khilyuk, L. F., Robertson Jr, J. O., Endres, B., and Chilingarian, G. (2000). *Magnitude and Intensity of Earthquakes*. Elsevier.

Kim, D. and Lekic, V. (2019). Groundwater variations from autocorrelation and receiver functions. *Geophysical Research Letters*, 46(23):13722–13729.

King, N., Argus, D., Langbein, J., Agnew, D., Bawden, G., Dollar, R., Liu, Z., Galloway, D., Reichard, E., Yong, A., et al. (2007). Space geodetic observation of expansion of the San Gabriel Valley, California, aquifer system, during heavy rainfall in winter 2004–2005. *Journal of Geophysical Research: Solid Earth*, 112(B3).

Kirsch, R. (2006). *Groundwater geophysics: a tool for hydrogeology*. Springer.

Konikow, L. F. (2011). Contribution of global groundwater depletion since 1900 to sea-level rise. *Geophysical Research Letters*, 38(17).

Larose, E., Carrière, S., Voisin, C., Bottelin, P., Baillet, L., Guéguen, P., Walter, F., Jongmans, D., Guillier, B., Garambois, S., et al. (2015). Environmental seismology: What can we learn on earth surface processes with ambient noise? *Journal of Applied Geophysics*, 116:62–74.

Larose, E., Derode, A., Campillo, M., and Fink, M. (2004). Imaging from one-bit correlations of wideband diffuse wave fields. *Journal of Applied Physics*, 95(12):8393–8399.

Larose, E., Roux, P., and Campillo, M. (2007). Reconstruction of Rayleigh–Lamb dispersion spectrum based on noise obtained from an air-jet forcing. *The Journal of the Acoustical Society of America*, 122(6):3437–3444.

Lecocq, T., Caudron, C., and Brenguier, F. (2014). Msnoise, a python package for monitoring seismic velocity changes using ambient seismic noise. *Seismological Research Letters*, 85(3):715–726.

Lecocq, T., Longuevergne, L., Pedersen, H. A., Brenguier, F., and Stammler, K. (2017). Monitoring ground water storage at mesoscale using seismic noise: 30 years of continuous observation and thermo-elastic and hydrological modeling. *Scientific reports*, 7(1):1–16.

Lewis, W., Xuereb, K., Escuder-Bueno, I., Andrés-Doménech, I., Torres, A. M., Gómez, Á. P.-N., López, E. P., Solar, D. A., Perales-Momparler, S., Wade, R., et al. (2015). Application of the E^2STORMED decision support tool in Haż-Żabbar.

Lin, F.-C., Moschetti, M. P., and Ritzwoller, M. H. (2008). Surface wave tomography of the western United States from ambient seismic noise: Rayleigh and Love wave phase velocity maps. *Geophysical Journal International*, 173(1):281–298.

Lin, F.-C., Ritzwoller, M. H., Townend, J., Bannister, S., and Savage, M. K. (2007). Ambient noise Rayleigh wave tomography of New Zealand. *Geophysical Journal International*, 170(2):649–666.

Liu, Z., Huang, J., and Li, J. (2010). Comparison of four techniques for estimating temporal change of seismic velocity with passive image interferometry. *Earthquake Science*, 23(5):511–518.

Lobkis, O. I. and Weaver, R. L. (2001). On the emergence of the Green's function in the correlations of a diffuse field. *The Journal of the Acoustical Society of America*, 110(6):3011–3017.

Longuet-Higgins, M. S. (1950). A theory of the origin of microseisms. *Philosophical Transactions of the Royal Society of London. Series A, Mathematical and Physical Sciences*, 243(857):1–35.

Lowrie, W. (2007). Seismology and the internal structure of the Earth. In *Fundamentals of Geophysics*, pages 121–203. Cambridge University Press.

Magri, O. (2006). A geological and geomorphological review of the Maltese Islands with special reference to the coastal zone. *Territoris*, 6:7–26.

Mainsant, G., Larose, E., Brönnimann, C., Jongmans, D., Michoud, C., and Jaboyedoff, M. (2012). Ambient seismic noise monitoring of a clay landslide: Toward failure prediction. *Journal of Geophysical Research: Earth Surface*, 117(F1).

Mao, S., Campillo, M., van der Hilst, R. D., Brenguier, F., Stehly, L., and Hillers, G. (2019). High temporal resolution monitoring of small variations in crustal strain by dense seismic arrays. *Geophysical Research Letters*, 46(1):128–137.

Mao, S., Lecointre, A., van der Hilst, R. D., and Campillo, M. (2022). Space-time monitoring of groundwater fluctuations with passive seismic interferometry. *Nature communications*, 13(1):1–9.

Margat, J. and Van der Gun, J. (2013). *Groundwater around the world: a geographic synopsis*. Crc Press.

McNamara, D. E. and Buland, R. P. (2004). Ambient noise levels in the continental United States. *Bulletin of the seismological society of America*, 94(4):1517–1527.

Meier, U., Shapiro, N. M., and Brenguier, F. (2010). Detecting seasonal variations in seismic velocities within Los Angeles basin from correlations of ambient seismic noise. *Geophysical Journal International*, 181(2):985–996.

Milsom, J. and Eriksen, A. (2011). Seismic Methods: General Considerations. In *Field Geophysics*, pages 211–226. John Wiley & Sons, Ltd.

MIT OpenCourseware (2021). Qualitative Aspects of Groundwater and Groundwater Flow. https://geo.libretexts.org/Bookshelves/Geography_(Physical)/The_Environment_of_the_Earth%27s_Surface_(Southard)/04:_Groundwater/4.04:_Qualitative_Aspects_of_Groundwater_and_Groundwater_Flow. Accessed: 15-12-2022.

Mordret, A., Jolly, A., Duputel, Z., and Fournier, N. (2010). Monitoring of phreatic eruptions using interferometry on retrieved cross-correlation function from ambient seismic noise: Results from Mt. Ruapehu, New Zealand. *Journal of Volcanology and Geothermal Research*, 191(1-2):46–59.

Mordret, A., Mikesell, T. D., Harig, C., Lipovsky, B. P., and Prieto, G. A. (2016). Monitoring southwest Greenland's ice sheet melt with ambient seismic noise. *Science advances*, 2(5):e1501538.

Moschetti, M., Ritzwoller, M., and Shapiro, N. (2007). Surface wave tomography of the western United States from ambient seismic noise: Rayleigh wave group velocity maps. *Geochemistry, Geophysics, Geosystems*, 8(8).

National Audit Office (2012). Performance Audit: Safeguarding Malta's Groundwater. Technical report, Malta.

National Statistics Office (2019a). Key Figures For Malta 2019 edition: Visuals and Words. https://nso.gov.mt/en/nso/Media/Salient-Points-of-Publications/Document/Key%20Figures%20for%20Malta%20-%202019%20Edition/Malta%20In%20Figures%20-%202019.pdf. Accessed: 15-12-2022.

National Statistics Office (2019b). Regional Tourism: 2016-2018. https://nso.gov.mt/en/News_Releases/View_by_Unit/Unit_C3/Tourism_Statistics/Documents/2019/News2019_106.pdf. Accessed: 15-12-2022.

Newbery, J. (1968). The perched water table in the upper limestone aquifer of Malta. *Journal of the Institution of Water Engineers*, 22:551–570.

Niemczynowicz, J. (1999). Urban hydrology and water management–present and future challenges. *Urban water*, 1(1):1–14.

Obermann, A., Froment, B., Campillo, M., Larose, E., Planès, T., Valette, B., Chen, J., and Liu, Q. (2014). Seismic noise correlations to image structural and mechanical changes associated with the *Mw* 7.9 2008 Wenchuan earthquake. *Journal of Geophysical Research: Solid Earth*, 119(4):3155–3168.

OTT (2011). OTT Thalimedes: Float operated shaft encoder with integrated data logger. https://www.ott.com/download/leaflet-shaft-encoder-for-depth-and-water-level-measurement-ott-thalimedes-1/. Accessed: 15-12-2022.

Owuor, S. O., Butterbach-Bahl, K., Guzha, A. C., Rufino, M. C., Pelster, D. E., Díaz-Pinés, E., and Breuer, L. (2016). Groundwater recharge rates and surface runoff response to land use and land cover changes in semi-arid environments. *Ecological Processes*, 5(1):1–21.

Pedley, H. (1987). Controls on Cenozoic carbonate deposition in the Maltese islands: review and reinterpretation. *Memorie della Societa Geologica Italiana*, 38:81–94.

Pedley, H. (1990). Syndepositional tectonics affecting Cenozoic and Mesozoic deposition in the Malta and SE Sicily areas (Central Mediterranean) and their bearing on Mesozoic reservoir development in the N Malta offshore region. *Marine and Petroleum Geology*, 7(2):171–180.

Pedley, H. M. et al. (1978a). A new lithostratigraphical and palaeoenvironmental interpretation for the coralline limestone formations (Miocene) of the Maltese Islands. *Overseas Geology and Mineral Resources*, 54.

Pedley, H. M., House, M. R., and Waugh, B. (1978b). The geology of the Pelagian block: the Maltese Islands. In *The ocean basins and margins*, pages 417–433. Springer.

Peterson, J. R. (1993). Observations and modeling of seismic background noise. Technical report, US Geological Survey.

Poupinet, G., Ellsworth, W., and Frechet, J. (1984). Monitoring velocity variations in the crust using earthquake doublets: An application to the Calaveras Fault, California. *Journal of Geophysical Research: Solid Earth*, 89(B7):5719–5731.

Prampolini, M., Gauci, C., Micallef, A. S., Selmi, L., Vandelli, V., and Soldati, M. (2018). Geomorphology of the north-eastern coast of Gozo (Malta, Mediterranean Sea). *Journal of Maps*, 14(2):402–410.

Ramillien, G., Famiglietti, J. S., and Wahr, J. (2008). Detection of continental hydrology and glaciology signals from GRACE: a review. *Surveys in geophysics*, 29(4):361–374.

Ratdomopurbo, A. and Poupinet, G. (1995). Monitoring a temporal change of seismic velocity in a volcano: Application to the 1992 eruption of Mt. Merapi (Indonesia). *Geophysical research letters*, 22(7):775–778.

Rehfeld, U. and Janssen, A. W. (1995). Development of phosphatized hardgrounds in the miocene Globigerina Limestone of the Maltese archipelago, including a description of *Gamopleura melitensis* sp. nov. (Gastropoda, Euthecosomata). *Facies*, 33(1):91–106.

Rivet, D., Brenguier, F., and Cappa, F. (2015). Improved detection of preeruptive seismic velocity drops at the Piton de La Fournaise volcano. *Geophysical Research Letters*, 42(15):6332–6339.

Rodell, M., Velicogna, I., and Famiglietti, J. S. (2009). Satellite-based estimates of groundwater depletion in India. *Nature*, 460(7258):999–1002.

Sabra, K. G., Gerstoft, P., Roux, P., Kuperman, W., and Fehler, M. C. (2005a). Extracting time-domain Green's function estimates from ambient seismic noise. *Geophysical research letters*, 32(3).

Sabra, K. G., Gerstoft, P., Roux, P., Kuperman, W., and Fehler, M. C. (2005b). Surface wave tomography from microseisms in Southern California. *Geophysical Research Letters*, 32(14).

Sánchez-Pastor, P., Obermann, A., Schimmel, M., Weemstra, C., Verdel, A., and Jousset, P. (2019). Short-and long-term variations in the Reykjanes geothermal reservoir from seismic noise interferometry. *Geophysical Research Letters*, 46(11):5788–5798.

Sapiano, M. (2020). Integrated Water Resources Management in the Maltese Islands. *Acque Sotterranee-Italian Journal of Groundwater*, 9(3).

Sapiano, M., Micallef, P., Attard, G., and Zammit, M.-L. (2008). The evolution of water culture in Malta: an analysis of the changing perceptions towards water throughout the ages. *Options Méditerranéennes : Série A. Séminaires Méditerranéens*, 83:97–109.

Sauter, R., ten Brink, P., Withana, S., Mazza, L., Pondichie, F., Clinton, J., Lopes, A., and Bego, K. (2013). Impacts of climate change on all European islands. Technical report, London, United Kingdom.

Schimmel, M., Stutzmann, E., and Gallart, J. (2011). Using instantaneous phase coherence for signal extraction from ambient noise data at a local to a global scale. *Geophysical Journal International*, 184(1):494–506.

Sens-Schönfelder, C. and Wegler, U. (2006). Passive image interferometry and seasonal variations of seismic velocities at Merapi Volcano, Indonesia. *Geophysical research letters*, 33(21).

Sens-Schönfelder, C. and Wegler, U. (2011). Passive image interferometry for monitoring crustal changes with ambient seismic noise. *Comptes Rendus Geoscience*, 343(8-9):639–651.

Shapiro, N. M. and Campillo, M. (2004). Emergence of broadband Rayleigh waves from correlations of the ambient seismic noise. *Geophysical Research Letters*, 31(7).

Shapiro, N. M., Campillo, M., Stehly, L., and Ritzwoller, M. H. (2005). High-resolution surface-wave tomography from ambient seismic noise. *Science*, 307(5715):1615–1618.

Shearer, P. M. (2009). Surface waves and normal modes. In *Introduction to Seismology*, pages 215–238. Cambridge University Press.

Stein, S. and Wysession, M. (2003). Basic Seismological Theory. In *An Introduction to Seismology, Earthquakes and Earth Structure*, pages 29–116. Wiley-Blackwell.

Stuart, M. E., Heaton, T. H. E., Maurice, L., Chilton, P. J., and Williams, P. J. (2008). A preliminary study on the identification of the sources of nitrate contamination in groundwater in Malta: Results and interpretation. Technical report, Nottingham, United Kingdom.

Sustainable Energy and Water Conservation Unit (2011). The 1st Water Catchment Management Plan for the Malta Water Catchment District. Technical report, Marsa, Malta.

Sustainable Energy and Water Conservation Unit (2015). The 2nd Water Catchment Management Plan for the Malta Water Catchment District 2015 - 2021. Technical report, Marsa, Malta.

Taira, T., Brenguier, F., and Kong, Q. (2015). Ambient noise-based monitoring of seismic velocity changes associated with the 2014 *Mw* 6.0 South Napa earthquake. *Geophysical Research Letters*, 42(17):6997–7004.

Telford, W., Geldart, L., and Sheriff, R. (1990). Seismic Methods. In *Applied Geophysics*, pages 136–280. Cambridge University Press.

Tsai, V. C. (2011). A model for seasonal changes in GPS positions and seismic wave speeds due to thermoelastic and hydrologic variations. *Journal of Geophysical Research: Solid Earth*, 116(B4).

Tukey, J. W. (1962). The future of data analysis. *The annals of mathematical statistics*, 33(1):1–67.

United Nations (2021). The United Nations World Water Development Report 2021: Valuing Water. Technical report, Paris, France.

United Nations (2022). The United Nations World Water Development Report 2022: Groundwater Making the invisible visible: Facts and Figures. Technical report, Perugia, Italy.

van der Gun, J. (2021). Groundwater resources sustainability. In *Global groundwater*, pages 331–345. Elsevier.

vanEssen (2022). Dataloggers. https://www.vanessen.com/product-category/data-loggers/. Accessed: 15-12-2022.

Velis, M., Conti, K. I., and Biermann, F. (2017). Groundwater and human development: synergies and trade-offs within the context of the Sustainable Development Goals. *Sustainability science*, 12(6):1007–1017.

Vella, A., Galea, P., and D'Amico, S. (2013). Site frequency response characterisation of the Maltese islands based on ambient noise H/V ratios. *Engineering geology*, 163:89–100.

Ventosa, S., Schimmel, M., and Stutzmann, E. (2019). Towards the processing of large data volumes with phase cross-correlation. *Seismological Research Letters*, 90(4):1663–1669.

Voisin, C., Guzmán, M. A. R., Refloch, A., Taruselli, M., and Garambois, S. (2017). Groundwater monitoring with passive seismic interferometry. *Journal of Water Resource and Protection*, 9(12):1414–1427.

Wada, Y., Van Beek, L. P., Van Kempen, C. M., Reckman, J. W., Vasak, S., and Bierkens, M. F. (2010). Global depletion of groundwater resources. *Geophysical research letters*, 37(20).

Wang, Q.-Y., Brenguier, F., Campillo, M., Lecointre, A., Takeda, T., and Aoki, Y. (2017). Seasonal crustal seismic velocity changes throughout Japan. *Journal of Geophysical Research: Solid Earth*, 122(10):7987–8002.

Wapenaar, K. and Fokkema, J. (2006). Green's function representations for seismic interferometry. *Geophysics*, 71(4):SI33–SI46.

Weaver, R. L. and Lobkis, O. I. (2004). Diffuse fields in open systems and the emergence of the Green's function (L). *The Journal of the Acoustical Society of America*, 116(5):2731–2734.

Wegler, U., Nakahara, H., Sens-Schönfelder, C., Korn, M., and Shiomi, K. (2009). Sudden drop of seismic velocity after the 2004 *Mw* 6.6 mid-Niigata earthquake, Japan, observed with Passive Image Interferometry. *Journal of Geophysical Research: Solid Earth*, 114(B6).

Wegler, U. and Sens-Schönfelder, C. (2007). Fault zone monitoring with passive image interferometry. *Geophysical Journal International*, 168(3):1029–1033.

WSC (2021). Water Services Corporation: Annual Report 2021. https://www.wsc.com.mt/elementor-6682/. Accessed: 13-12-2022.

Xanke, J. and Liesch, T. (2022). Quantification and possible causes of declining groundwater resources in the Euro-Mediterranean region from 2003 to 2020. *Hydrogeology Journal*, 30(2):379–400.

Xiao, M., Koppa, A., Mekonnen, Z., Pagán, B. R., Zhan, S., Cao, Q., Aierken, A., Lee, H., and Lettenmaier, D. P. (2017). How much groundwater did California's Central Valley lose during the 2012–2016 drought? *Geophysical Research Letters*, 44(10):4872–4879.

Yang, Y. and Ritzwoller, M. H. (2008). Characteristics of ambient seismic noise as a source for surface wave tomography. *Geochemistry, Geophysics, Geosystems*, 9(2).

Yang, Y., Ritzwoller, M. H., Levshin, A. L., and Shapiro, N. M. (2007). Ambient noise Rayleigh wave tomography across Europe. *Geophysical Journal International*, 168(1):259–274.

Yang, Z., Yuan, C., and Denolle, M. A. (2022). Detecting Elevated Pore Pressure due to Wastewater Injection Using Ambient Noise Monitoring. *The Seismic Record*, 2(1):38–49.

Yao, H. and Van Der Hilst, R. D. (2009). Analysis of ambient noise energy distribution and phase velocity bias in ambient noise tomography, with application to SE Tibet. *Geophysical Journal International*, 179(2):1113–1132.

Yao, H., van Der Hilst, R. D., and De Hoop, M. V. (2006). Surface-wave array tomography in SE Tibet from ambient seismic noise and two-station analysis—I. Phase velocity maps. *Geophysical Journal International*, 166(2):732–744.

Zhou, Y., Dong, D., Liu, J., and Li, W. (2013). Upgrading a regional groundwater level monitoring network for Beijing Plain, China. *Geoscience Frontiers*, 4(1):127–138.

A. MSNoise configuration settings

The MSNoise package includes a Configurator web graphical user interface (GUI), which allows the user to access and define the general MSNoise configuration (*config*), and the *station* and *filter* configurations, at different steps of the workflow. The home page of the web interface (Figure A.1) shows the project folder location and database, progress bars, and statistics related to data availability, cross-correlation, STACK, Moving Window Cross-Spectral (MWCS), DTT and PSD jobs. Results and PSD charts can be accessed from the *Results* and *Quality Control (QC)* sections respectively.

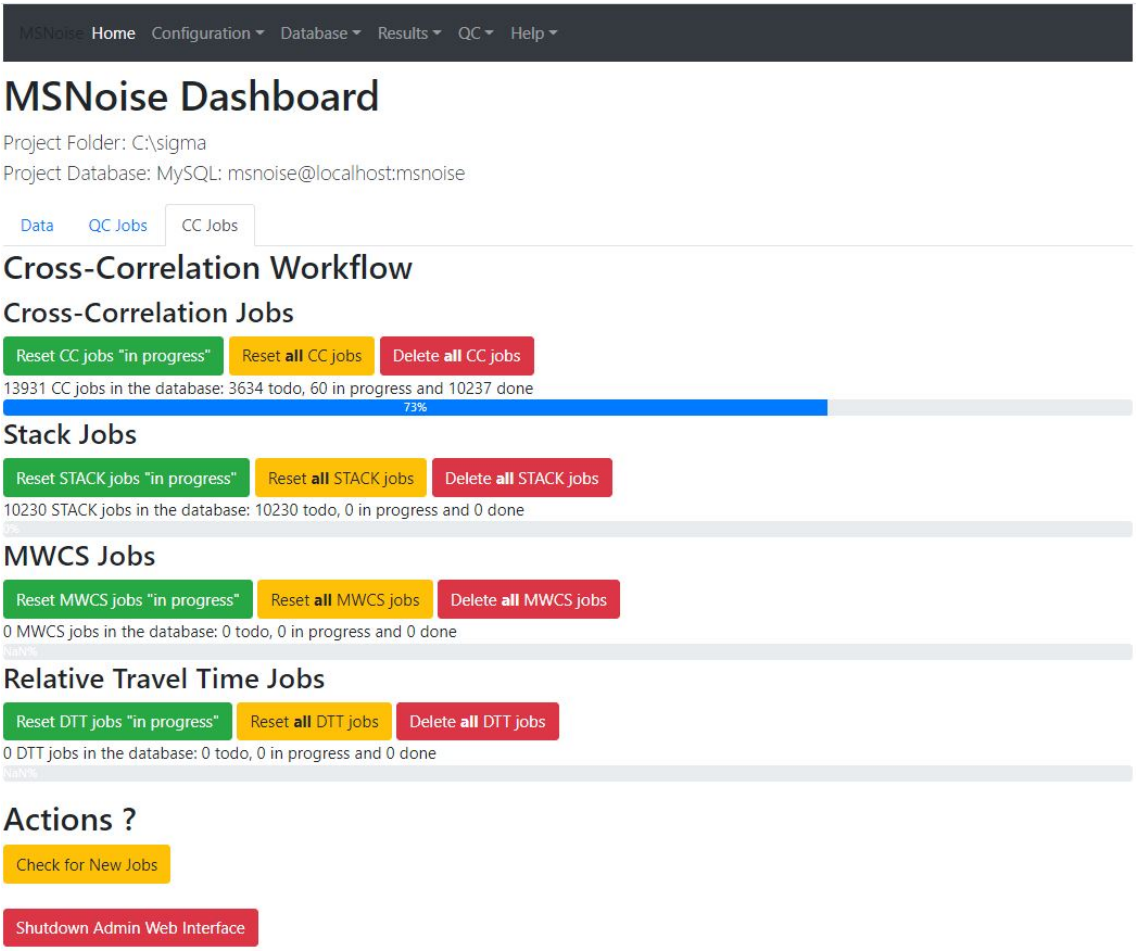

Figure A.1.: The graphical user interface (GUI) of MSNoise. The GUI main page, in the form of a website, shows the project folder location and database, progress bars, and statistics related to data availability, cross-correlation, STACK, MWCS, DTT and PSD jobs (Lecocq et al., 2014).

The *station* configuration section displays station information, such as the name, net-

work, location codes, channels, the geolocation (in longitude and latitude), the coordinate system and the altitude. The *filter* configuration section lists the created filters. For each filter, the table shows the filter id, the lower and higher frequency bounds of the Whiten function and of the linear regression done in MWCS (Hz), the specified window length and step to perform MWCS (s). The different filters can be activated or deactivated for processing purposes.

The general *config* section contains a number of configuration settings that are easily editable throughout the workflow. The folder where all archive data is being saved (*data_folder*), the data structure used (*data_structure*), the networks (*network*) and channels (*channels*) to analyse can all be accessed from this configuration section. The *startdate* and *enddate* parameters specify the first and last day of the data archive that need to be processed, while the duration of the analysis (s) is defined by *analysis_duration*. The sampling rate (in Hz) for cross-correlation (*cc_sampling_rate*), and the *resampling_method* (either Decimate or Lanczos [Downsampling]) are also configurable. The pre-processing low-pass and high-pass filter values (Hz) are specified by *preprocess_lowpass* and *preprocess_highpass* respectively. The parameter *preprocess_maxgap* sets the largest gap length (s) that will be filled with interpolation values in the pre-processing stage. If the gap length is found to be greater than this parameter, MSNoise sets the gap to zero. Another preprocessing step is defined by *preprocess_taper_length*, where tapering involves smoothening amplitudes at the beginning and end of traces, without changing the frequency content. Hence, this parameter deals with the length of the applied taper, in seconds. Since different seismic instruments may have different response functions, MSNoise also provides the option to remove instrument response (*remove_response*) to obtain the actual ground displacement. The *response_prefilt* parameter allows for the removal of instrument correction in the pre-filtering stage, and it is set to a range of values that are broader than the *preprocess_lowpass* and *preprocess_highpass* filters.

Windsorizing allows for reducing the influence of outliers on the statistics of the data (Blaine, 2018). With *windosorizing*, one can either not apply windsorizing by setting the parameter to 0, apply windosorizing at N times the RMS value or apply one-bit normalisation by setting the parameter to -1. One-bit normalisation is a common form of normalisation that reduces the effect of non-stationary signals (such as earthquakes) on time series of noise data, by setting each data point to its positive or negative sign (e.g., Cupillard et al., 2011). A number of studies have used one-bit normalisation in the pre-processing of noise data (Shapiro and Campillo, 2004; Shapiro et al., 2005; Larose et al., 2007; Yao and Van Der Hilst, 2009). One-bit normalisation can also be used for seismic coda processing (e.g., Campillo and Paul, 2003), which ensures an improved signal-to-noise ratio of the coda correlations, due to the enhanced multiple scattering (Larose et al., 2004).

Spectral whitening is a powerful normalisation tool in the frequency domain, which assumes that uncorrelated noise is obscuring the desired signal (Groos et al., 2012). In

the ambient seismic noise correlations, the emergence of broadband signals can be improved when using the *whitening* parameter in MSNoise. When representing estimates of the broadband Green's functions, this technique improves the stacked cross-correlation functions (e.g., Bensen et al., 2007). Spectral whitening has been used in varying ways in studies (e.g., Bensen et al., 2007; Brenguier et al., 2008b; Groos, 2010). The *whitening* command provides three options: whitening of all traces, no whitening or whitening if the components are different. The *whitening_type* details the type of spectral whitening function to be used, which include the brutal type (amplifying the signal to an amplitude of 1.0), and dividing the spectrum by its PSD. With the *clip_after_whiten* command, clipping (winsorizing) can be called before or after whitening. The *stack_method* parameter suggests the type of stack method to be used, which includes the linear mean or phase-weighted stack (PWS) method. The linear mean *stack_method* saves the daily CCF as a simple mean CCF of all windows, while the pws *stack_method* saves the daily CCF as the PWS. The number of days that are to be stacked in the moving-window stacks are configured with *mov_stack*.

If daily real-time monitoring is to be done, the number of days to be monitored when the archive is being scanned can be set by *crondays*. The type of cross-correlation, autocorrelation and cross-correlation for cross-components can be specified by *cc_type*, *cc_type_single_station_AC*, *cc_type_single_station_SC* respectively. The *components_to_compute* and *components_to_compute_single_station* configuration bits list the components to components to be computed for different stations, and for single stations, respectively. MSNoise also allows for cross-correlations and daily cross-correlations to be saved using the *keep_all* and *keep_days* commands, respectively.

The *response_format* and *response_path* commands specify the instrument response file format to be removed, and the location of the file respectively. The *qc_components* configuration bit sets the components to be processed for quality control. The beginning and end dates of the reference function to be used are set by the *ref_begin* and *ref_end* configuration bits. The *export_format* allows for the stacks to be exported in Seismic Analysis Code (SAC) format, MSEED or both formats, and *sac_format* specifies the SAC stack format (Doublets or Clarke). The maximum lag (s) is set to a value in *maxlag* that is enough to properly visualise the CCFs for the interstation distances observed in the present study, from the interstation distance plot (Figure 4.9). The *corr_duration* parameter relates to the length of the data window to be correlated and processed (s), while *overlap* is a factor representing the amount of overlap between each data window in calculating δt between the current and reference CCF. Ensuring an overlap between data windows is beneficial since it increases stacking, which allows for the cancelling of noise and making a signal more pronounced.

For the MWCS technique, the *dtt_lag* configuration bit defines how the lag window will be defined, mainly dynamic or static. The dynamic option determines the minimum

time lag based on the interstation distance and *dtt_v*, which specifies the velocity that will be used to avoid ballistic waves (Figure 4.9). Whenever *dtt_lag* is static, *dtt_minlag* specifies the minimum lag time to avoid ballistic waves. The *dtt_width* configuration bit details the length of the time lag window (s) used to perform MWCS, while *dtt_sides* specifies if causal or acausal time lags, or both will be used. The minimum coherence to be set on the δt measurements can be defined with *dtt_mincoh*, where MWCS points having values lower than *dtt_mincoh* will not be used in the weighted linear regression (WLS). The *dtt_maxerr* parameter sets a maximum limit on the error on the δt measurement, which does not use (in the WLS) MWCS points that have a δt measurement error that is greater than *dtt_maxerr*. The maximum δt values (s) can be specified with *dtt_maxdt*, where points with a higher δt value are not used in the WLS. Finally, the *stretching_max* and *stretching_nsteps* configuration bits describe the maximum stretching coefficient and the number of stretching steps between 1-*stretching_max* and 1+*stretching_max*, respectively. Further details about the MSNoise configuration bits can be reviewed in the MSNoise website (http://msnoise.org/doc/).

B. Rolling average

A moving average of 30, 60, and 90 days was also tested on the $\delta v/v$ and the water level data to smoothen out hard to explain anomalies. At a 60- and 90- rolling average, very small changes in the $\delta v/v$ are lost in the averaging. Hence, a 30-day rolling average was selected, so as to give the best detail on a monthly scale.

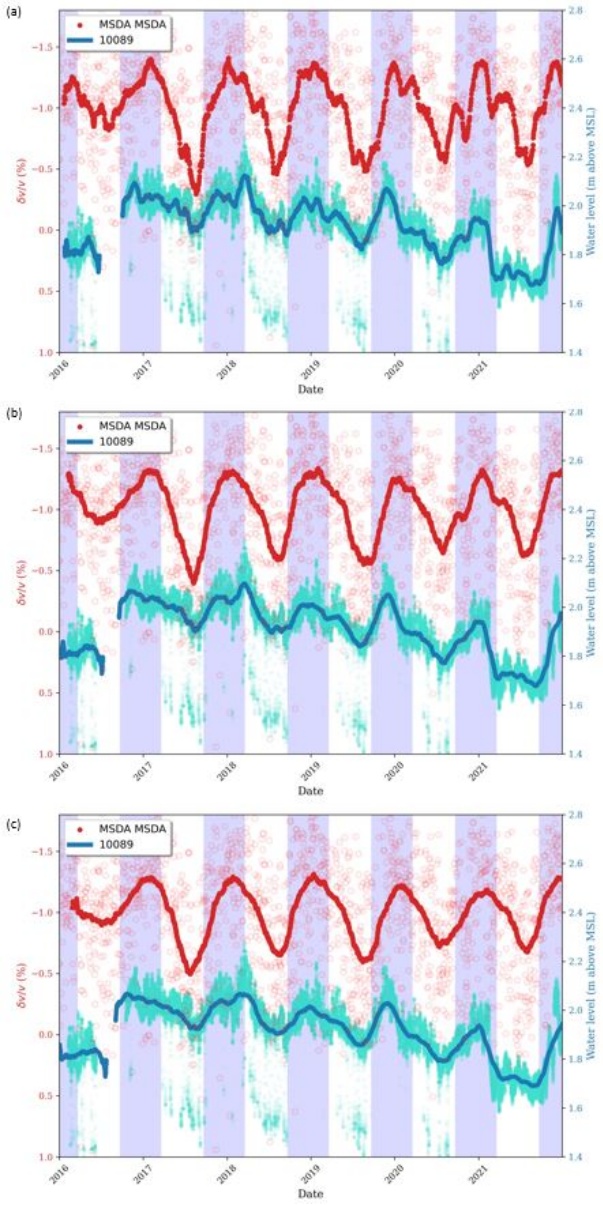

Figure B.1.: Example of different rolling averages of $\delta v/v$ and water level: (a) 30-day, (b) 60-day, and (c) 90-day.